

THEORETICAL AND EXPERIMENTAL DETERMINATION OF PROPERTIES OF
NiO AND Fe-doped NiO

by

Fidele J. Twagirayezu, B.S

A thesis submitted to the Graduate Council of
Texas State University in partial fulfillment
of the requirements for the degree of
Master of Science
with a Major in Physics
August, 2017

Committee Members:

Wilhelmus Geerts, Chair

Luisa Scolfaro

Ravi Droopad

COPYRIGHT

by

Fidele J. Twagirayezu

2017

FAIR USE AND AUTHOR'S PERMISSION STATEMENT

Fair Use

This work is protected by the Copyright Laws of the United States (Public Law 94-553, section 107). Consistent with fair use as defined in the Copyright Laws, brief quotations from this material are allowed with proper acknowledgement. Use of this material for financial gain without the author's express written permission is not allowed.

Duplication Permission

As the copyright holder of this work, I, Fidele J. Twagirayezu, authorize duplication of this work, in whole or in part, for educational or scholarly purposes only.

DEDICATION

In memory of “all innocent civilians” who lost their lives especially in the African Great Lakes Region, “you” will be remembered by every generation. Also this work is dedicated to all peoples who have been persecuted worldwide.

ACKNOWLEDGEMENTS

The research for my thesis was supported by a Thesis Research Support Fellowship awarded by the Graduate College at Texas State University, a grant from the Department of Defense (DOD), and a NASA Fellowship (Texas Space Grant Consortium). This is also a great moment to thank people whose support has been of pivotal importance during the time I have been a student at Texas State University.

I would like to particularly thank my thesis advisor Dr Wilhelmus Geerts for his dedication and advice. He has been a source of knowledge and encouragement, and yet there is no doubt to say that he is a great physics Professor; naturally graduate physics is not simple, but his way of teaching makes it a simple subject.

I would like to thank Dr Luisa Scolfaro for her vital explanation about density functional theory (DFT), and also for pointing out some errors in my primary calculations of band structure and density of states for Fe-doped NiO. In addition, she advised me to turn off the symmetry (ISYM) tag for the VASP relaxation of Fe-doped NiO.

Finally, I would like to thank Postdoc Pablo D Borges who taught me the usage of the VASP (Vienna ab initio simulation package) software, UNIX and LINUX commands, and how to execute VASP codes for DFT calculations. In addition, PhD candidate John Peterson was also a great source of knowledge, and I thank him for

teaching me to how use p4VASP, and for pointing out wrong k-points of the path in the Brillouin zone (BZ) for my previous simulations.

TABLE OF CONTENTS

ACKNOWLEDGMENTS.....	v
LIST OF FIGURES	x
LIST OF TABLES.....	xi
ABSTRACT.....	xiv
CHAPTER	
I.INTRODUCTION.....	1
1.1 Basic Physics	1
1.1.1 Optical Physics.....	1
1.1.2 Solid State Physics.....	7
1.1.3 Atomic Origin of Magnetism in Matter.....	11
1.1.4 Quantum Physics	13
1.2 Motivation.....	22
1.3 Literature overview of optical and magnetic properties of NiO and NiFeO samples.....	24
II.INTRODUCTION TO NICKEL AND ITS OXIDES	28
2.1 Nickel and Nickel Oxides.....	28
2.1.1 Nickel (Ni)	28
2.1.2 Nickel (II) Oxide (NiO) and Permalloy Oxide (Fe-doped NiO).....	29
2.1.3 NiO and Fe-doped NiO Crystalline Structures.....	29
III.COMPUTATIONAL THEORY	31
3.1 Early First-Principle Calculations.....	31
3.2 Density Functional Theory	34
3.2.1 Born-Oppenheimer Approximation.....	35
3.2.2 Hohenberg-Kohn Theorems.....	36

3.2.3 Khon-Sham (KS) Equations	37
3.2.4 Exchange-Correlation Functional(s)	42
IV.COMPUTATIONAL APPROACH.....	45
4.1 Brillouin Zone Sampling.....	45
4.2 Bandstructure and Density of States (DOS)	46
4.3 Generalized Gradient Approximation (GGA)	47
4.4 Beyond Generalized Gradient Approximation (GGA)	48
4.5 VASP Simulation Settings.....	49
4.6 Simulation Methods	50
V.COMPUTATIONAL RESULTS	59
5.1 Optical and Magnetic Properties of NiO	59
5.2 Optical and Magnetic Properties of Fe-doped NiO	69
5.3 Summary	75
VII.LAB INSTRUMENTS AND RESULTS	76
6.1 AJA Magnetron Sputtering System	76
6.1.1 Sample Manufacturing.....	77
6.2 X-Ray Diffraction System	82
6.2.1 System Preparation and Measurement Methods.....	83
6.2.2 X-Ray Measurement Methods	83
6.2.3 X-Ray Results for NiO and Ni _{0.8} Fe _{0.2} O samples	85
6.3 Ellipsometry	87
6.3.1 CompleteEase Software	90
6.3.2 Ellipsometric Measurement Methods and Settings.....	91
6.4 Physical Property Measurement System.....	93
6.4.1 Measurement Methods and Settings	93
6.4.2 Measurement of Magnetic Properties of Samples	94
VIII.EXPERIMENTAL RESULTS	97

7.1 Optical Characterization.....	97
7.1.1 Optical Properties of NiO (Low, and High O Sputtering Pressure).....	97
7.1.2 Optical Properties of Ni _{0.8} Fe _{0.2} O _{1-δ} (Low, and High O Sputtering Pressure).....	98
7.2 Magnetic Characterization.....	101
7.2.1 Magnetic Properties of NiO (Low, and High O Sputtering Pressure).....	101
7.2.2 Magnetic Properties of Ni _{0.8} Fe _{0.2} O _{1-δ} (Low, and High O Sputtering Pressure).....	107
7.3 Summary.....	114
 VIII.DISCUSSION.....	 116
(A) Overall Summary.....	116
(B) Future Works.....	117
 APPENDIX SECTION.....	 119
APPENDIX A.....	119
APPENDIX B.....	119
 REFERENCES.....	 121

LIST OF TABLES

Table	Page
5.1 Magnetic moment (in μ_B) obtained for 4-atom NiO using GGA	61
5.2 Calculated magnetic moment (in μ_B) for atomic orbitals and the net magnetic moment for 4-atom NiO using GGA+U(3eV).....	63
5.3 Calculated magnetic moment for 32-atom NiO using GGA+U	68
5.4 The calculated magnetic moment (in μ_B) for 32-atom 6.25 at. % Fe-doped NiO using GGA+U (4 eV).....	73
5.5 Calculated magnetic moment (in μ_B) for 32-atom 12.5 at. % Fe-doped NiO using GGA+U (4 eV).....	74
6.1 Deposition Parameters for NiO and NiFeO Samples	79
6.2 Composition and Dimensions of NiO and NiFeO samples	79
6.3 Samples thickness measured with different techniques: Ellipsometer, and Crystal Monitor	80

LIST OF FIGURES

Figure	Page
2.1 Crystal Structure of NiO with spin-polarization in the (111) planes	30
3.1 Self-Consistent Loop for Density Functional Theory.....	40
4.1 First Brillouin Zone (BZ) of (FCC) lattice with some points and lines of high Symmetry	46
4.2 Bandstructure for Si	47
4.3 FCC (SC lattice + eight basis atoms) Structure for NiO.....	51
4.4 Rhombohedral Structure of a 4-atom NiO.....	54
4.5 Rhombohedral Structure of a 32-atom NiO Supercell.....	54
4.6 Brillouin zone (BZ) along with high symmetry points for the rhombohedral structure for NiO, or Fe-doped NiO	56
4.7 Rhombohedral Structure of Fe-doped NiO Supercell (32 atoms)	57
5.1 Bandstructure (BS) and density of states (DOS) for both spin up and spin down states obtained for a 4-atom NiO using GGA	60
5.2 Density of states (DOS) for a 4-atom NiO with GGA+U.....	62
5.3 Bandstructure (BS) and Density of States (DOS) for a 32-atom NiO Supercell using GGA+U	64
5.4 Density of states (DOS) for a 32-atom Supercell NiO with the U-approach.....	65
5.5 Calculated optical properties of NiO using GGA+U method.....	66
5.6 Density of States (DOS) for spin-up and spin-down states obtained for a 32-atom Fe-doped NiO supercell using GGA+U.....	69
5.7 Calculated optical properties of Fe-doped NiO using the GGA+U(4eV)	

method.....	71
6.1 AJA Sputtering System in the Cleanroom at Texas State University.....	76
6.2 Crystal Monitor Thickness (nm) vs Ellipsometer Est. Thickness (nm) just after deposition.....	81
6.3 Rigaku X-Ray Diffractometer (XRD) at Texas State University	84
6.4 An example of the propagation of light for a theta (2 degrees)/ 2theta scan with XRD.....	85
6.5 XRD for NiO, and Ni _{0.8} Fe _{0.2} O _{1-δ} samples.....	86
6.6 (a) Elliptically polarized light wave as described by Eq. (6.2). (b) Illustrates the propagation and polarization of light.....	88
6.7 Reflection of light from a single thin film	90
6.8 Woollam M-2000 Ellipsometer (Credit J.A Woollam .Co. Inc.).....	92
6.9 Quantum Design PPMS-Model 6000 at Texas State University	95
6.10 The sample holder fully covered by the sample (in the middle) + substrate tiles.....	96
7.1 B-Spline Multi-layers Fitting for NiO	97
7.2 Measured optical properties for NiO (Low and high O sputtering pressure).....	98
7.3 B-Spline Fitting for Ni _{0.8} Fe _{0.2} O _{1-δ} . Ni _{0.8} Fe _{0.2} O _{1-δ} (Low O pressure) (a). Ni _{0.8} Fe _{0.2} O _{1-δ} (High O pressure) (b).....	99
7.4 Measured optical properties for Ni _{0.8} Fe _{0.2} O _{1-δ} (Low, and high O pressures), optical constants (n, k) (a), absorption coefficient (b),	100
7.5 Optical properties of NiO (Low O) vs. those of Ni _{0.8} Fe _{0.2} O _{1-δ} (Low O) (a), optical properties of NiO (High O) vs. those of Ni _{0.8} Fe _{0.2} O _{1-δ} (High O) (b)	101
7.6 Magnetic properties for NiO sputtered at low O pressure	103

7.7 Magnetic moment $m(H)$ measured from -9 to +9 Tesla at different Temperatures.....	104
7.8 Magnetic properties for NiO sputtered at high O pressure	105
7.9 Magnetic moment $m(H)$ for NiO samples measured from -9 to 9 Tesla at different temperatures	106
7.10 Magnetic moment $m(H)$ at 300K for NiO samples, one sputtered at low O pressure, and another sputtered at high O pressure.....	107
7.11 Magnetic Properties for $Ni_{0.8}Fe_{0.2}O_{1-\delta}$ sputtered at low O pressure.....	108
7.12 Magnetic moment $m(H)$ for $Ni_{0.8}Fe_{0.2}O_{1-\delta}$ samples	109
7.13 Magnetic Properties for $Ni_{0.8}Fe_{0.2}O_{1-\delta}$ sputtered at high O pressure.....	110
7.14 Measured magnetic moment $m(H)$ at different temperature for $Ni_{0.8}Fe_{0.2}O_{1-\delta}$ sample sputtered at High O pressure	111
7.15 Measured magnetic moment $m(H)$ at 300K for $Ni_{0.8}Fe_{0.2}O_{1-\delta}$ sputtered at low O pressure, and $Ni_{0.8}Fe_{0.2}O_{1-\delta}$ sputtered at high O pressure.....	112
7.16 Measured magnetic moment $m(T)$ at 9 Tesla of the sample holder+ substrate (a), and the sample holder (b).....	113

ABSTRACT

In this era of fast advances in nanotechnology and electronics Ni has become an interesting element because its oxidized form possessing semiconducting properties is enabling several applications such as gas sensors, dyed sensitized photocathodes and electrodes in alkaline batteries. In addition, recently NiO has been utilized as a resistive switching (RS) memory [1], [2], [3], and energy-saving application as an electrochromic (EC) [4], [5], [6] smart window. In particular, NiO has promise for RS memory to replace Flash memory beyond the 14 nm process node. RS memory guarantees rapid speeds in reading and writing, high storage density and non-volatility with lifetimes of ten years or more. [7]The EC property of the NiO is also a driving force behind futuristic technologies such as smart windows and non-volatile displays. However, the exact mechanisms behind certain phenomena such as RS and EC are still not fully understood.

In addition, in recent years there has been lots of research in Diluted Magnetic Semiconductor (DMS) materials because of their important utilization in spintronic devices. DMS materials have charge and spin degrees of freedom enabling the realization of devices with magnetic, electronic and optical functionalities. DMS electronic devices can have a higher speed and a lower switching energy than traditional electronic devices. NiO is an antiferromagnetic p-type semiconductor because of the presence of vacancy at Ni²⁺ sites [8], [9]. [10]The magnetic structure of NiO consists of ferromagnetic sheets of Ni²⁺ parallel to the (111) plane with opposite spin directions in neighboring planes. The

Fe doping of NiO leads to Fe-doped NiO (Permalloy Oxide) which exhibits advantageous DMS properties over NiO. However, the effect of transition metal (TM) ion doping on the magnetic properties of NiO at higher iron concentration has not been fully determined yet. The effect iron doping has on the Neel temperature of NiO is also still unknown.

The study of switching properties of NiO or Fe-doped NiO in resistive random-access memory (RRAM) devices can be easily possible by using optical or magnetic techniques that is why their physical properties such as optical or magnetic properties are also of interest in this thesis. In this thesis research, the physical properties of NiO, and Fe-Doped NiO were determined via theoretical and experimental methods.

a) Theoretical Methods:

For the theoretical part of the research, computer simulations were performed, and the physical properties were determined with the Density Functional Theory (DFT) using Vienna ab initio Simulation Package (VASP). Electronic, optical and magnetic properties of 4-atom NiO, 32-atom NiO, and 32-atom Fe-doped NiO supercells with spin polarization in the (111) planes were calculated using (GGA) and GGA+U methods. The theoretical outcome was compared with the experimental one or other findings from the literature. We began with simulations of 4-atom NiO, and 32-atom NiO. For the simulation of 32-atom Fe-doped NiO, we utilized the crystal structure of 32-atom NiO with Ni atoms substituted by Fe atoms (6.25%, and 12.5% Fe concentrations) without altering the initial spin ordering. Crystal structure and Brillouin zone were produced

using Vesta software and Bilbao Crystallographic Server respectively, and graphs were produced using p4VASP and Origin Pro software. The results show that NiO is an antiferromagnetic semiconductor with a band gap depending on the Hubbard potential (U). The nature of the magnetism of Fe-doped NiO depends on the amount of Fe atoms. The Fe doping reduces the band gap, and this reduction of the band gap has the effect on the optical properties. With the Hubbard potential U(4eV), the static refractive index is about 2.2 for NiO, and 2.25 for 6.25 at.% Fe-doped NiO respectively.

b) Experimental Methods:

For the experiment part of the research, different laboratory instruments including an AJA Sputtering System, an X-ray Diffractometer (XRD), an Ellipsometer, and a Physical Property Measurement System (PPMS) were utilized. Data analysis was carried out using specialized software. The samples were manufactured using the AJA Sputtering system. An XRD system was used to gather information about the crystal structure for each sample. The optical properties were determined using Ellipsometer and the CompleteEase software was used for ellipsometric data analysis. Magnetic properties were obtained using the PPMS interfaced with the Multivu program. All graphs were obtained using Microsoft Excel or Origin Pro software. The experiment involved NiO and $\text{Ni}_{0.8}\text{Fe}_{0.2}\text{O}_{1-\delta}$ samples, and one sample for each species was sputtered at low O pressure and another was sputtered at high O pressure. The XRD shows that all samples have NaCl-type structure. Samples sputtered at low O pressure have a higher magnetic

moment than those sputtered at high O pressure. Each sample has the static refractive index (n) close to 2.

I.INTRODUCTION

1.1 Basic Physics

1.1.1 Optical Physics

The theory of optics involves the properties of light, including the interaction of light with matter, and ways to investigate optical phenomena. Light is described as a propagating superposition of the electric field (E) and the magnetic field (B), producing electromagnetic waves through space-time, consequently these fields satisfy the wave equation. The unifying relation between the electric and magnetic fields is given by the following Dirac Symmetrized -Maxwell equations (in SI units) [11], [12]:

$$\nabla \cdot \vec{E} = \rho^e / \epsilon_0 \quad (1.1)$$

$$\nabla \cdot \vec{B} = \mu_0 \rho^m \quad (1.2)$$

$$\nabla \times \vec{E} = -\partial \vec{B} / \partial t - \mu_0 \vec{j}^m \quad (1.3)$$

$$\nabla \times \vec{B} = \mu_0 \epsilon_0 \partial \vec{E} / \partial t + \mu_0 \vec{j}^e \quad (1.4)$$

Here ρ^e is the electric charge density ρ^m is the magnetic charge density, \vec{j}^e is the electric current density, \vec{j}^m is the magnetic current density, ϵ_0 is the permittivity of free space, μ_0 is the permeability of free space. Normally, the charge density is related to the polarization \vec{P} arising from the interaction of light with the medium. Since no magnetic monopoles have been observed, Maxwell's equations can be obtained from the above equations by assuming that the magnetic charge and magnetic current densities are equal to zero.

The combination of the Maxwell's equations derived from (1), (3), and the combination of the Maxwell's equations from (2), (4) lead respectively to the following electric and magnetic field equations:

$$\frac{1}{c^2} \frac{\partial^2 \vec{E}}{\partial t^2} + \nabla \times (\nabla \times \vec{E}) = -\mu_0 \left(\frac{\partial \vec{j}}{\partial t} + \frac{\partial^2 \vec{P}}{\partial t^2} \right) \quad (1.5a)$$

$$\frac{1}{c^2} \frac{\partial^2 \vec{B}}{\partial t^2} + \nabla \times (\nabla \times \vec{B}) = \mu_0 \left(\nabla \times \vec{j} + \nabla \times \frac{\partial \vec{P}}{\partial t} \right) \quad (1.5b)$$

Here $c = 1/\sqrt{\mu_0 \epsilon_0}$ is the speed of light in the vacuum. Using the bac-cab formula for both \vec{E} and \vec{B} vector fields, the above field equations become:

$$\frac{1}{c^2} \frac{\partial^2 \vec{E}}{\partial t^2} - \nabla^2 \vec{E} = -\mu_0 \left(\frac{\partial \vec{j}}{\partial t} + \frac{\partial^2 \vec{P}}{\partial t^2} \right) \quad (1.6a)$$

$$\frac{1}{c^2} \frac{\partial^2 \vec{B}}{\partial t^2} - \nabla^2 \vec{B} = \mu_0 \left(\nabla \times \vec{j} + \nabla \times \frac{\partial \vec{P}}{\partial t} \right) \quad (1.6b)$$

In the free space, the solutions to the above equations are for sinusoidal waves, and can be written in the following form [13]:

$$\vec{E}(\vec{r}, t) = \vec{E}_0 \{ \exp[i(\vec{k} \cdot \vec{r} - \omega t)] \} \quad (1.7a)$$

$$\vec{B}(\vec{r}, t) = \vec{B}_0 \{ \exp[i(\vec{k} \cdot \vec{r} - \omega t)] \} \quad (1.7b)$$

Here \vec{r} is the position vector, and \vec{k} is the wave number vector, ω is the angular frequency, \vec{E}_0 and \vec{B}_0 are the respective complex electric and magnetic field amplitudes [13] associated with the initial electric and magnetic vector fields respectively.

As mentioned before, when light propagates through a material, its electric field interacts with it causing a polarization \vec{P} in the material. In the case of sinusoidal waves, the general equation for the electric field has the following solutions [13]:

$$\vec{E}(\vec{r}, t) = \vec{E}_0 \{ \exp[i(\vec{k} \cdot \vec{r} - \omega t)] \} \quad (1.8a)$$

$$\vec{P}(\vec{r}, t) = \vec{P}_0 \{ \exp[i(\vec{k} \cdot \vec{r} - \omega t)] \} \quad (1.8b)$$

For a linear material, the polarization \vec{P} as a function of ω can be written as a product of the susceptibility χ and the electric field \vec{E} , as follows:

$$\vec{P}(\omega) = \varepsilon_0 \chi(\omega) \vec{E}(\omega) \quad (1.9)$$

The substitution of the expressions of \vec{P} , and \vec{E} into the general electric fields equation leads to the following formula for the dispersion relation:

$$k^2 = \varepsilon_0 \mu_0 \{ 1 + \chi(\omega) \} \omega^2 \quad (1.10)$$

Since, $c = 1/\sqrt{\varepsilon_0 \mu_0}$ then the complex reflection index $\tilde{N} = n + i\kappa$ can be expressed in terms of the susceptibility:

$$n + i\kappa = \sqrt{1 + \chi(\omega)} \quad (1.11)$$

Under the influence of electric field \vec{E} of light, the motion of an electron bound to a nucleus is described by the following equation [14]:

$$m \frac{d^2 \vec{r}}{dt^2} + m\Gamma \frac{d\vec{r}}{dt} + m\omega_0^2 \vec{r} = -e\vec{E} \quad (1.12)$$

Here, m is the electronic mass, e is the elementary charge, \vec{r} is the position of the charge, \vec{E} is the electric vector field, Γ is the damping factor, and ω_0 is the resonant frequency. The solution to the above equation is given by [14]:

$$\vec{r} = \frac{e\vec{E} / m}{(\omega_0^2 - \omega^2) - i\Gamma \omega} \quad (1.13)$$

Since the position \vec{r} is linked to the dipole moment which is, in turn, related to the atomic polarizability $\tilde{\alpha}$, then the expression for this latter is given by [14]:

$$\hat{\alpha}(\omega) = \frac{e^2}{m} \frac{1}{(\omega_0^2 - \omega^2) - i\Gamma \omega} \quad (1.14)$$

On one hand, the displacement field \vec{D} can be related to the electric field \vec{E} by the formula:

$$\vec{D}(x, \omega) = \tilde{\epsilon}(\omega) \vec{E}(x, \omega) \quad (1.15)$$

On the other hand, the displacement field \vec{D} can be related to the polarizability by $\vec{D} = (1 + 4\pi N) \hat{\alpha} \vec{E}$, where N is number of oscillators, then equating the expressions for \vec{D}

and substituting the atomic polarizability by its expression, the dielectric function

$\tilde{\varepsilon} = \varepsilon_1 + i\varepsilon_2$ is given by [14]:

$$\tilde{\varepsilon} = 1 + \frac{4\pi N e^2}{m} \frac{1}{(\omega_0^2 - \omega^2) - i\Gamma\omega} \quad (1.19)$$

Here, ε_1 and ε_2 are respective real and imaginary parts of $\tilde{\varepsilon}$, and their expressions are respectively given by [14]:

$$\varepsilon_1 = 1 + \frac{4\pi N e^2}{m} \frac{(\omega_0^2 - \omega^2)}{(\omega_0^2 - \omega^2)^2 + \Gamma^2\omega^2} \quad (1.20a)$$

$$\varepsilon_2 = \frac{4\pi N e^2}{m} \frac{\Gamma\omega}{(\omega_0^2 - \omega^2)^2 + \Gamma^2\omega^2} \quad (1.20b)$$

Let N_i be the density of N oscillators with a resonance frequency ω_i . Eq.1.19

can be written in the following way:

$$\tilde{\varepsilon} = 1 + \frac{4\pi e^2}{m} \sum_i \frac{N_i}{(\omega_i^2 - \omega^2)^2 - j\Gamma_i\omega} \quad (1.21)$$

Since, $\tilde{\varepsilon} = \tilde{N}^2$, the optical properties n , and k can be expressed in terms of the values of

ε_1 and ε_2 in the following way:

$$n = \{1/2[(\varepsilon_1^2 + \varepsilon_2^2)^{1/2} + \varepsilon_1]\}^{1/2} \quad (1.22a)$$

$$k = [1/2[(\varepsilon_1^2 + \varepsilon_2^2)^{1/2} - \varepsilon_2]]^{1/2} \quad (1.22b)$$

As light propagates through space, it carries energy as described by the following Poynting's theorem:

$$\oiint_{\partial V} \vec{S}(r) \cdot \hat{n} da + \int_V \vec{J}(r) \cdot \vec{E}(r) dv + \frac{\partial}{\partial t} \int_V u dv = 0 \quad (1.23)$$

Here $\vec{S}(r)$ is the Poynting vector, $\vec{J}(r)$ is the electric current density vector, da is the surface element, dv is the volume element, \hat{n} is the unit normal vector perpendicular to the surface element, $\vec{E}(r)$ is the electric field, and u is the energy density.

Also the Kramers-Kronig relations, derived using the Cauchy's theorem due to the analyticity of $\varepsilon(\omega)/\varepsilon_0$, give n as function of energy E , relating k to the Cauchy's principal value P in the following way [15]:

$$n(E) - 1 = \frac{2}{\pi} P \int_0^{\infty} \frac{E' k(E')}{E'^2 - E^2} dE' \quad (1.24)$$

Here, E is the energy, and should not be confused with the magnitude E of the electric field \vec{E} used in previous equations.

Upon a material light can experience certain optical phenomena such as reflection or refraction and the angle of refraction depends on the index of refraction, according the following Snell's equations for reflection and refraction respectively:

$$\varphi_i = \varphi_r \quad (1.25a)$$

$$\hat{N}_1 \sin(\varphi_1) = \hat{N}_2 \sin(\varphi_2) \quad (1.25b)$$

Here φ_i , and φ_r are incidence and reflection angles for the reflection phenomenon upon the interface of a material. \hat{N}_1 , \hat{N}_2 are complex refractive indices, and φ_1 , φ_2 are incident and refraction angles for the medium 1 and medium 2 [16]. Note that since the refractive indices are complex, also the refraction angles can be complex.

Therefore, it is possible to construct an instrument that is able to determine the optical properties n , and k once angles of incidence and refraction are known; for example the ellipsometric technique takes the advantage of the above theory for the determination of a variety of physical properties such as optical constants, sample thickness, etc.

1.1.2 Solid State Physics

The formulation of the quantum theory was important to the birth of solid state theory, and the progress in solid state physics was ignited by the discovery of the x-ray diffraction which showed that most crystals have a periodic structure of atoms or groups of atoms. Infinitely repeating groups of identical atoms form an ideal crystal. With the lattice being the set of mathematical points, the lattice along with a basis represents the crystal structure. It is the choice of crystal axes that allows the identification of a basis for the crystal structure. A 3-D lattice is spanned by the three primitive translation vectors \vec{a}_1

, \vec{a}_2 and \vec{a}_3 such that the translation leaves the crystal invariant from \vec{r} to \vec{r}' . Such crystal translation is defined by [17], [18]:

$$\vec{r}' = \vec{r} + \vec{T} \quad \text{with} \quad \vec{T} = \gamma_1 \vec{a}_1 + \gamma_2 \vec{a}_2 + \gamma_3 \vec{a}_3 \quad (1.26)$$

Here γ_1 , γ_2 , and γ_3 are arbitrary integers, and \vec{T} is the crystal translation vector. The primitive lattice is the smallest lattice that can serve as a building block of matter, and it is spanned by the primitive translation vectors \vec{a}_1 , \vec{a}_2 , and \vec{a}_3 . Each primitive cell or primitive basis contains the exact same number of atoms. The choice of primitive cell can be achieved in different way, and a primitive cell with exactly one lattice point is known as Wigner-Seitz primitive cell. In momentum space, a primitive cell of reciprocal lattice is the Brillouin zone (BZ).

In two-dimensions there exist five types of lattices, and in three dimensions, due to the symmetry groups there exist seven types of cells and fourteen lattices, for example, in a cubic system, there are three different lattices: the simple cubic (SC) lattice, the body-centered cubic (BCC) lattice, and the face-centered (FCC) lattice. The orientation of the crystal plane is defined by the three non-collinear points whose coordinates may be in terms of lattice constants \vec{a}_1 , \vec{a}_2 and \vec{a}_3 , provided that each of them is situated on each Cartesian axis [17], [18]. However, in most of cases, the orientation of the crystal plane is preferred to be defined by indices of the plane. Normally, there exist v_1, v_2 , and v_3 integers such that the intercepts of each crystal plane are $v_1 \vec{a}_1, v_2 \vec{a}_2$, and $v_3 \vec{a}_3$.

The reciprocals of v_1 , v_2 , and v_3 are reduced to corresponding three integers (hkl) called the indices of the plane or Miller Indices. In other words, (hkl) are the coefficients of the linear combination in the 3-D reciprocal space spanned by reciprocal lattice vectors \vec{b}_1 , \vec{b}_2 , and \vec{b}_3 [17], [18]. When the light wave interacts with the crystal, the distance d between crystal planes is related to the angle of incidence θ and the n multiple of light wavelength λ as described by the following Bragg law [17], [19]:

$$2d \sin(\theta) = n\lambda \quad (1.27)$$

Since the crystal is invariant under the translation vector \vec{T} , then any local physical property such as the electron density $n(\vec{r})$ is also invariant, and then can be expanded into a Fourier series. Then, the Fourier series of electron density and its Fourier transform are [17], [19]:

$$\begin{aligned} n(\vec{r}) &= \sum_G n_G \exp(i\vec{G}\cdot\vec{r}) \\ n_G &= (1/v_c) \int_{cell} n(\vec{r}) \exp(-i\vec{G}\cdot\vec{r}) d^3\vec{r} \end{aligned} \quad (1.28)$$

Here, v_c is crystal cell-volume, n_G is the Fourier coefficient whose set determines the x-ray scattering amplitude, and the sum is over a set of reciprocal lattice vectors \vec{G} which determine the possible x-ray reflections. If the incoming and outgoing beams are respectively represented by $\exp(i\vec{k}\cdot\vec{r})$, and $\exp(-i\vec{k}'\cdot\vec{r})$, the phase difference is given by $\exp[i(\Delta\vec{k})\cdot\vec{r}]$, where $\Delta\vec{k} = \vec{k}' - \vec{k}$ is called the scattering vector. And when $\Delta\vec{k} = \vec{G}$ the diffraction condition for elastic scattering is given by: $2\vec{k}\cdot\vec{G} + \vec{G}^2 = 0$. And under the

same condition, the scattering amplitude F_G can be expressed in terms of the atomic form factor f_j [17], [19]:

$$F_G = N \int_{cell} n(\vec{r}) \exp(-i\vec{G}\cdot\vec{r}) d^3\vec{r} = N \sum_j \exp(-i\vec{G}\cdot\vec{r}_j) f_j \quad (1.29)$$

For spherically symmetric electron distribution with \vec{r} making an angle α with \vec{G} , the atomic form factor is given by the formula [17], [19]:

$$f_j = \int n_j(\vec{r}) \exp(-i\vec{G}\cdot\vec{r}) d^3\vec{r} = \sin c(Gr) \quad (1.30)$$

Any periodic crystal can be considered as a quantum system with periodic potential, and according to the quantum theory, a suitable solution to such periodic quantum system is given by the following Bloch theorem:

The solution to a quantum system with a periodic potential is the product of the plane wave function and a function of the same period as the crystal lattice [20].

$$\psi_k(\vec{r}) = u_k(\vec{r}) \exp(i\vec{k}\cdot\vec{r}) \quad (1.31)$$

where $u_k(\vec{r})$ has the same periodicity as the crystal lattice, $u_k(\vec{r}) = u_k(\vec{r} + \vec{T})$, here, \vec{T} is the lattice translation vector. Since $\psi_k(\vec{r})$ is identical to, $\psi_{k+G}(\vec{r})$, and both correspond to the energy $E(\vec{k})$, and $E(\vec{k} + \vec{G})$ respectively, then $E(\vec{k}) = E(\vec{k} + \vec{G})$ [20].

1.1.3 Atomic Origin of Magnetism in Matter

The total angular momentum and the nature of interaction of electrons in matter are responsible for the phenomenon of magnetism. There are five classes of magnetic materials: diamagnetic, paramagnetic, ferromagnetic, antiferromagnetic, and ferrimagnetic [21].

A diamagnetic material is a substance with a closed shell in atoms that usually have spin, and orbital moments oriented so that the atoms have a zero permanent net magnetic moment. But, in presence of the external magnetic induction, this material obtains a non-zero net magnetic moment. The magnetic moment as function of applied magnetic field, $m(H)$ for a diamagnetic material is a linear curve that slowly decreases from zero; this means that a diamagnetic material has a negative susceptibility χ . The diamagnetic moment is independent of the temperature.

A paramagnetic material is a substance whose atoms possess a non-zero net magnetic moment due to the non-cancellation of the spin of the electrons. Although at zero field the net magnetic moment of a paramagnet is zero as the spins of the various atoms are randomly oriented and cancel each other out, when an external magnetic field is applied to the paramagnet it carries a net magnetic moment. The $m(H)$ for a paramagnetic material at small magnetic fields is a linear graph which increases rapidly from zero with increasing magnetic field; this means that its susceptibility χ is positive. At higher magnetic field the magnetic moment saturates. The magnetic moment is typically inversely proportional to the temperature, so the higher the temperature the less of the magnetic moments are aligned.

A ferromagnetic material is a substance with a non-zero net magnetic moment because the electron spins are mostly aligned in the same direction. For ferromagnetic materials the spins of neighboring atoms are aligned because of the exchange interaction. The net magnetic moment of a ferromagnetic material can be non-zero in zero magnetic field and depends on the field that was applied to the material in the past, in other words, ferromagnetic materials seem to remember their history characterized by hysteresis. The $m(H)$ for a ferromagnetic material is a non-linear graph with hysteresis.

An antiferromagnetic material is a substance with a zero net magnetic moment because the nearest neighbor's moments are aligned antiparallel, which leads to the cancellation of the net magnetic moment. One of the characteristics for antiferromagnetism is the behavior of the susceptibility above the Neel temperature. Above this temperature, the susceptibility obeys the Curie-Weiss law with a negative intercept indicating negative exchange interaction. Small grains of anti-ferromagnetic material tend to have a magnetic moment because of uncompensated spins near the surface of the antiferromagnetic material.

Finally, a ferrimagnetic material is a substance with a non-zero net magnetic moment because the magnetic moments of neighboring atoms are not equal. The magnetic moments in this material are aligned antiparallel. This is a particular case because for other previous magnetic materials, all magnetic moments are of equal magnitude. Antiferromagnetic and ferrimagnetic materials are related to ferromagnetic materials as all the three types of materials show magnetic order. The order in these materials disappears at higher temperature. For instance, ferromagnetic materials are

paramagnetic, above the Curie temperature, and antiferromagnetic materials are paramagnetic above the Neel temperature.

The susceptibility for a sample can be easily calculated by using the following formula [21]:

$$\chi = \vec{M}/\vec{H} \text{ (emu/cm}^3 \text{ Oe)} \quad (1.32)$$

Here, \vec{M} is the magnetization which is equal to the magnetic moment \vec{m} per unit of volume v , and \vec{H} is the applied magnetic field strength.

1.1.4 *Quantum Physics*

Quantum physics is the most mysterious and successful theory for describing the microscopic level of any physical (made of matter) system. According to quantum theory, the properties of a system can be determined by solving the Schrodinger's equation which, in the time-independent, non- relativistic form, is:

$$\hat{H}\Psi(\vec{r}_1, \dots, \vec{r}_n) = E\Psi(\vec{r}_1, \dots, \vec{r}_n) \quad (1.33)$$

Here \hat{H} is the Hamiltonian operator describing all interactions of the system of n particles, E is the total energy of the system, and Ψ , which contains all the information about the system, is a set of solutions, or eigenstates of the Hamiltonian operator. Each of these eigenstates ψ_n is associated with an eigenvalue E_n , a real number that satisfies the eigenvalue equation.

In Hilbert space, quantum mechanics becomes the matrix mechanics where probability amplitudes are complex numbers and operators are represented by complex matrices. Thus the above time-independent Schrodinger's equation can be written as follows [22]:

$$\begin{pmatrix} H_{11} & H_{12} & H_{13} & \cdots & H_{1n} \\ H_{21} & H_{22} & H_{23} & \cdots & H_{2n} \\ H_{31} & H_{32} & H_{33} & \cdots & H_{3n} \\ \vdots & \vdots & \cdots & \ddots & \vdots \\ H_{n1} & H_{n2} & H_{n3} & \cdots & H_{nn} \end{pmatrix} \begin{pmatrix} \psi_1 \\ \psi_2 \\ \psi_3 \\ \vdots \\ \psi_n \end{pmatrix} = E \begin{pmatrix} \psi_1 \\ \psi_2 \\ \psi_3 \\ \vdots \\ \psi_n \end{pmatrix} \quad (1.34)$$

The exact expression for the Hamiltonian depends on nature of the physical system being described by the Schrodinger's equation. A much simpler form of the Hamiltonian is that of the particle in a box or a simple harmonic oscillator, and their corresponding Schrodinger's equation can be simply solved in closed form. The Hamiltonian for a many-body system is more complicated due to many degrees of freedom and a number of interactions between electrons and nuclei of the system. A full expression for the Hamiltonian for a multiple interactions system is as follows:

$$\hat{H} = \left(-\sum_i \frac{1}{2} \nabla_i^2 - \sum_I \frac{1}{2M_I} \nabla_I^2 + \frac{1}{2} \sum_{i \neq j} \frac{1}{|\vec{r}_i - \vec{r}_j|} + \frac{1}{2} \sum_{I \neq J} \frac{Z_I Z_J}{|\vec{r}_I - \vec{r}_J|} - \sum_{i,I} \frac{Z_I}{|\vec{r}_i - \vec{r}_I|} \right) \quad (1.35)$$

Here, M_I are nuclear masses, \vec{r}_i are electron positions, \vec{r}_I are nuclear positions, the first term is the kinetic energy of each electron, the second term the kinetic energy of the nuclei, the third term is the electron- electron interaction, and the fourth term is the nuclei-nuclei interaction and the last term is the electron-nuclei interaction. The evolution

of any quantum state between measurements is described by the time-dependent Schrodinger equation:

$$\hat{H}|\Psi\rangle = i\frac{\partial}{\partial t}|\Psi\rangle \quad (1.36)$$

By solving the above time-dependent Schrodinger's equation, the time-dependent solution takes a simple form, especially if the potential operator is time-independent, thus due to separation of variable, the solution for stationary states can be written as follows:

$$\Psi(\vec{r}_i, \vec{r}_l, t) = \tilde{\Psi}(\vec{r}_i, \vec{r}_l)\Theta(t) \quad (1.37)$$

The above separation, with a constant of separation E, leads to the respective time-independent and time evolution equations:

$$\hat{H}\tilde{\Psi}(\vec{r}_i, \vec{r}_l) = E\tilde{\Psi}(\vec{r}_i, \vec{r}_l) \quad (1.38a)$$

$$i\frac{d}{dt}\Theta(t) = E\Theta(t) \quad (1.38b)$$

The solution to the time-dependent Schrödinger's equation can now be written in the following form:

$$\Psi(\vec{r}_i, \vec{r}_l, t) = \tilde{\Psi}(\vec{r}_i, \vec{r}_l)\exp(-iEt) \quad (1.39)$$

This solution is stationary because the expectation value of a given time-independent operator \hat{O} for this solution is time-independent:

$$\begin{aligned}
\langle \Psi | \hat{O} | \Psi \rangle &= \int \prod_j dr_j \prod_J dr_J \Psi^*(\vec{r}_i, \vec{r}_I) \hat{O} \Psi(\vec{r}_i, \vec{r}_I) \\
&= \int \prod_j dr_j \prod_J dr_J \tilde{\Psi}^*(\vec{r}_i, \vec{r}_I) e^{iEt} \hat{O} \tilde{\Psi}(\vec{r}_i, \vec{r}_I) e^{-iEt} \\
&= \langle \tilde{\Psi} | \hat{O} | \tilde{\Psi} \rangle
\end{aligned} \tag{1.40}$$

This is also the reason why the time-independent Schrödinger's equation may be an appropriate choice for the study of the properties for arbitrary physical system.

The time-dependent many-electron wave function can also be written in terms of single-particle wave function $\psi_{k_i}(\vec{r}_i)$ as follows [23]:

$$\Psi(\vec{r}_1, \vec{r}_2, \dots, \vec{r}_N, t) = \sum_{\{k_1 \dots k_N\}} c(k_1, \dots, k_N, t) \psi_{k_1}(\vec{r}_1) \dots \psi_{k_N}(\vec{r}_N) \tag{1.41}$$

Here, k_i represents the quantum numbers, and $c(k_1, \dots, k_N, t)$ are the coefficients satisfying the permutations for particles (electrons). From the first to the second quantization; the wave function is written in terms of the Slater determinant and the occupation numbers in the Hilbert space as follows [23]:

$$\Psi(\vec{r}_1, \vec{r}_2, \dots, \vec{r}_N, t) = \sum_{\{n_1, \dots, n_\infty\}} \xi(n_1, \dots, n_\infty, t) \frac{1}{\sqrt{N!}} \begin{vmatrix} \psi_{k_1}(\vec{r}_1) & \dots & \psi_{k_1}(\vec{r}_N) \\ \vdots & \ddots & \vdots \\ \psi_{k_N}(\vec{r}_1) & \dots & \psi_{k_N}(\vec{r}_N) \end{vmatrix} \tag{1.42}$$

The above expression may be written in the following condensed form [23]:

$$\Psi(\vec{r}_1, \vec{r}_2, \dots, \vec{r}_N, t) = \sum_{\{n_1, \dots, n_\infty\}} \xi(n_1, \dots, n_\infty, t) \frac{1}{\sqrt{N!}} \sum_{P \in S_N} (-1)^p P[\psi_{k_1}(\vec{r}_1) \psi_{k_2}(\vec{r}_2) \dots \psi_{k_N}(\vec{r}_N)] \quad (1.43)$$

Here, P is the permutation operator for electrons, S_N is the permutation group, and p is the number of permutation. By defining a wave function:

$$\Psi(t) = \sum_{\{\tilde{n}_1, \dots, \tilde{n}_N\}} \xi(\tilde{n}_1, \dots, \tilde{n}_\infty, t) |\tilde{n}_1, \dots, \tilde{n}_\infty\rangle \quad (1.44)$$

Then the time-dependent Schrodinger's equation for a fermionic system can be written as follows [23]:

$$i \frac{\partial \Psi(t)}{\partial t} = \hat{H} \sum_{\{\tilde{n}_1, \dots, \tilde{n}_N\}} \xi(\tilde{n}_1, \dots, \tilde{n}_\infty, t) \frac{1}{\sqrt{N!}} \sum_P (-1)^p P[\psi_{k_1}(\vec{r}_1) \psi_{k_2}(\vec{r}_2) \dots \psi_{k_N}(\vec{r}_N)] \quad (1.45)$$

In a collection of N atoms, the change of momenta of both electrons and nuclei is the same because forces exerted on each other due to their charges is the same.

However the velocity of the nuclei is significantly less than that of the electrons because nuclei are heavier than electrons. This is seemingly credible on the time-scale of the nuclear motion, the electrons will instantaneously respond to any change in distance relative to the nuclei, or the ground-state configuration. This allows us to neglect the kinetic energy term for the nuclei in the full expression of the Hamiltonian, and solve first the time-independent Schrödinger's equation for the ground state in that configuration, and then solve for the nuclear motion. This approach of solving for electrons and nuclei separately is known as Born-Oppenheimer Approximation, and is based on the assumption that the wave-function for the Hamiltonian of the form:

$$\tilde{\Psi}(\vec{r}_i, \vec{r}_I) = \Psi(\vec{r}_i, \vec{r}_I) \Phi(\vec{r}_I) \quad (1.46)$$

and it requires that $\Psi(\vec{r}_i, \vec{r}_I)$ satisfies the time-independent Schrödinger's equation for the electrons in a motionless cloud of nuclei [24]:

$$\left(-\sum_i \frac{1}{2} \nabla_i^2 + \frac{1}{2} \sum_{i,j \neq i} \frac{1}{|\vec{r}_i - \vec{r}_j|} - \sum_{i,I} \frac{Z_I}{|\vec{r}_i - \vec{r}_I|} \right) \Psi(\vec{r}_i, \vec{r}_I) = E_e(\vec{r}_I) \Psi(\vec{r}_i, \vec{r}_I) \quad (1.47)$$

in which the eigenvalue E_e of the Hamiltonian also depends on the positions of the nuclei. If the full Hamiltonian (1.35) acts on the whole wave-function [24]:

$$\left(-\sum_J \frac{1}{2M_J} \nabla_J^2 + \frac{1}{2} \sum_J \sum_{K \neq J} \frac{Z_J Z_K}{|\vec{r}_J - \vec{r}_K|} + E_e(\vec{r}_I) \right) \tilde{\Psi}(\vec{r}_i, \vec{r}_I) = \hat{H} \tilde{\Psi}(\vec{r}_i, \vec{r}_I) \quad (1.48)$$

The adiabatic term E_e contributes to the energy of the system more than the remaining non-adiabatic terms according to the time-independent perturbation theory. By neglecting the non-adiabatic terms, the above Schrodinger's equation is satisfied if $\Phi(\vec{r}_I)$ is the solution of the following equation [24]:

$$\left(-\sum_J \frac{1}{2M_J} \nabla_J^2 + \frac{1}{2} \sum_J \sum_{K \neq J} \frac{Z_J Z_K}{|\vec{r}_J - \vec{r}_K|} + E_e(\vec{r}_I) \right) \Phi(\vec{r}_I) = E \Phi(\vec{r}_I) \quad (1.49)$$

The electron density for the system can be derived from the expression of the probability for finding arbitrary electron in a specific region of space.

The variational principle can also be utilized to find the lowest energy eigenstate of the system. By relaxing the restriction on the orthonormalization, the expectation value of the Hamiltonian operator \hat{H} can be expressed as follows:

$$\langle E \rangle = \frac{\langle \Psi | \hat{H} | \Psi \rangle}{\langle \Psi | \Psi \rangle} \quad (1.50)$$

Assume that the expectation value of the Hamiltonian $\langle E \rangle$ is the functional the wave function, $\langle E \rangle = E[\Psi]$, and make a small change $|\delta\Psi\rangle$, of the quantum state $|\Psi\rangle$, then the change in the expectation value of the energy is given by:

$$\delta E[\Psi] = \frac{\langle \Psi + \delta\Psi | \hat{H} | \Psi + \delta\Psi \rangle}{\langle \Psi + \delta\Psi | \Psi + \delta\Psi \rangle} - \frac{\langle \Psi | \hat{H} | \Psi \rangle}{\langle \Psi | \Psi \rangle} \quad (1.51)$$

After some algebra and without considering changes in second and higher-order terms in $\delta\Psi$, then the expression of the above change of the expectation value becomes:

$$\delta E[\Psi] = \frac{\langle \delta\Psi | (\hat{H} | \Psi \rangle - E[\Psi] | \Psi \rangle) + [\langle \delta\Psi | (\hat{H} | \Psi \rangle - E[\Psi] | \Psi \rangle)]^*}{\langle \Psi | \Psi \rangle} \quad (1.52)$$

If $|\Psi\rangle$ is the eigenstate of the Hamiltonian operator \hat{H} , with eigenvalue $E[\Psi]$, then there is no change of the functional, $E[\Psi]$. Thus, finding stationary values of $E[\Psi]$, can allow obtaining the eigenvalues of the Hamiltonian \hat{H} . Details for the derivation of above equations are found in Appendix B.

Let S be a system in the quantum state $|\Psi\rangle$ close to the ground state $|\psi_0\rangle$, assuming that the quantum state is complete, so it can be expressed as follows:

$$|\Psi\rangle = |\psi_0\rangle + \sum_n a_n |\psi_n\rangle \quad (1.53)$$

Using the variational principle, the value of $E[\Psi]$ is given by:

$$E[\Psi] = E_0 + \sum_n |a_n|^2 (E_n - E_0) + O(|a_n|^4) \quad (1.53)$$

Since for, $n \geq 1$, $E_n > E_0$, then one realizes that $E[\Psi] \geq E_0$, in other words this shows that functional gives the upper bound value of E_0 . The details about the above equations are found in Appendix B.

Since solving Schrodinger equations for many-body quantum systems is full of difficulties, other successful way for obtaining approximate solutions is the usage of the perturbation theory. For the time independent perturbation theory, the time- independent Schrodinger's equation for unperturbed system can be written as follows:

$$\hat{H}_0 |\psi_n^{(0)}\rangle = E_n^{(0)} |\psi_n^{(0)}\rangle \quad (1.54)$$

By adding a small perturbation to the Hamiltonian such that the perturbed Hamiltonian is $\hat{H} = \hat{H}_0 + \varsigma \hat{W}$ where \hat{W} is the perturbation operator and ς is a small positive dimensionless parameter to ensure that the perturbation is as small as possible, then the time-independent Schrodinger's equation becomes [25]:

$$(\hat{H}_0 + \varsigma \hat{W}) |\psi_n^{(0)}\rangle = E_n^{(0)} |\psi_n^{(0)}\rangle \quad (1.55)$$

Since the perturbation was chosen to be significantly small, eigenstates and eigenvalues of the above Schrodinger's equation can be expressed in series:

$$E_n = \sum_{k=0}^{\infty} \zeta^k E_n^{(k)}, \quad \text{where } E_n^{(k)} = \frac{1}{k!} \frac{d^k E_n}{d\zeta^k} \quad (1.56a)$$

$$|\psi\rangle = \sum_{k=0}^{\infty} \zeta^k |\psi^{(k)}\rangle, \quad \text{where } |\psi^{(k)}\rangle = \frac{1}{k!} \frac{d^k |\psi\rangle}{d\zeta^k} \quad (1.56b)$$

When ζ equals to zero, the above eigenstates and eigenvalues are for the unperturbed system. The time-independent Schrodinger's equation written in terms of the above series has the following form [25]:

$$(\hat{H}_0 + \zeta \hat{W}) \left(\sum_{k=0}^{\infty} \zeta^k |\psi_n^{(k)}\rangle \right) = \left(\sum_{k=0}^{\infty} \zeta^k E_n^{(k)} \right) \left(\sum_{k=0}^{\infty} \zeta^k |\psi_n^{(k)}\rangle \right) \quad (1.57)$$

After expansion, and comparison of coefficients of each power of ζ , one obtains infinite series of equations corresponding to the powers of ζ , and in general, the j th equation has the following form:

$$(\hat{H}_0 - E_n^{(0)}) |\psi_n^{(j)}\rangle = -\hat{W} |\psi_n^{(j-1)}\rangle + \sum_{k=1}^j E_n^{(k)} |\psi_n^{(j-k)}\rangle \quad (1.58)$$

The zero- order equation is just the Schrodinger equation with unperturbed Hamiltonian. If ζ is written in terms of small parameters $x^\mu = (x^1, x^2, \dots)$, there exists a map from a parameter manifold M on which the parametrized Hamiltonian is defined to be a Hermitian operator $H(x^\mu)$ acting on the Hilbert space. If the latter operator has respective eigenstates and energy eigenvalues $|\psi_n(x^\mu)\rangle$, and $E_n(x^\mu)$, then the eigenstates form a vector bundle on the manifold M . Since ζ is parametrized, if the unperturbed

reference point x_0^μ is equal to zero then the parametrized Hamiltonian operator can be written as follows:

$$\hat{H}(x^\mu) = \hat{H}(0) + x^\mu \hat{F}_\mu \quad (1.59)$$

Here, \hat{F}_μ is the operator which may represent the forces related to x^μ . According to the adiabatic assumption, energy eigenvalues and eigenstates are smooth functions of parameters, thus they can be expanded in series. In the power series expansion, energy eigenvalues and eigenstates have the following forms:

$$E_n(x^\mu) = E_n + x^\mu \partial_\mu E_n + \frac{1}{2!} x^\mu x^\nu \partial_\mu \partial_\nu E_n + \dots \quad (1.60a)$$

$$|\psi_n(x^\mu)\rangle = |\psi_n\rangle + x^\mu |\partial_\mu \psi_n\rangle + \frac{1}{2!} x^\mu x^\nu |\partial_\mu \partial_\nu \psi_n\rangle + \dots \quad (1.60b)$$

Since a quantum system with a time-independent perturbation is described by time-independent perturbation theory, thus a system that is subject to a time-dependent perturbation is described by time-dependent theory, however the mathematics for both theories are purely the same [26].

1.2 Motivation

NiO is playing a major role in science and technology because of its important physical properties. NiO with Ni vacancies is a p-type semiconductor which can serve as p-type transparent and conducting films and the bulk NiO is widely chosen for use as

antiferromagnetic or functional sensor layers [27]. Due to its unipolar and bipolar switching properties, NiO is the basis for RRAM technology which takes advantage of the soft breakdown of a switching material, usually transition metal oxides, for non-volatile data storage [28]. Normally, the migration of oxygen in the metal oxide can lead to switch from high resistance metallic state to low semiconducting or insulating state, and the control of different resistance levels is achieved by applying a certain voltage across the electrodes. Thus this resistance change property is utilized for the storage of bits of information. However, only little is known about the fundamental origin of these switching properties.

The Fe alloying of NiO leads to NiFeO which is also thought as the oxide of Permalloy (NiFe). Permalloy has become more and more important for modern nanotechnology and nano-electronics due to its particular magnetic properties. The first application of Permalloy was in telegraphic communication to maintain signal degradation caused by distortion of communication cables. Due to its high permeability, Permalloy is also applied in sensing devices and actuators [29]. Because of the important application of Permalloy [30], interest in study of Permalloy Oxide (NiFeO) has been growing among scientists. Another way for obtaining Permalloy oxide is the Fe doping of NiO. Normally, it has been observed that the Fe doping of NiO yields advantageous semiconducting properties, but as previously mentioned, only little is known about all physical properties of Fe-doped NiO.

The study of optical properties of NiO and Fe-doped NiO are of great importance especially for the RRAM technology. The RRAM switching properties are based on a filament that appears during the low resistance state and disappears during the

high resistance state. Locating this filament when studying the switching properties of RRAM devices currently requires the devices to be disassembled, but location techniques based on optical or magnetic properties would allow to remotely locating this filament without any disassembly.

1.3 Literature overview of optical and magnetic properties of NiO and NiFeO samples

While little has been done for thick or RF sputtered NiO samples, NiO powders and thin films have been studied extensively; for instance Issei Sugiyama et al. found ferromagnetic dislocations in antiferromagnetic NiO, and the origin of this ferromagnetism is the local non-stoichiometry at dislocations with Ni deficiency [31]. N. Mironova-Ulmane et al. found that NiO nanopowders (13-23 nm particles size) are antiferromagnetically ordered at room temperature with a rhombohedral structure (R-3m) as evidenced from the (422) Bragg reflect splitting located at high scattering angle of about 130 degrees[32].

The introduction of Ni²⁺ vacancies or doping with other cations leads to p-type semiconducting behavior [33].

Yuan-Hua Lin et al. found that the Fe-doped NiO samples exhibit FM properties at room temperature, and the magnetization loop exhibits the remnant magnetization, and this magnetism is likely to be caused by the introduction of magnetic Fe ions and related defects [34]. P. Douvalis et al. found that 2% ⁵⁷Fe-doped NiO samples, prepared by

heating in air at temperatures between 673 and 873 K, are ferromagnetic, and the origin of this magnetism is attributed to the presence of NiFe₂O₄ impurity phase, but this phase may not be detected by the XRD due to its small particle size effect or the high dilution [35].

S. Manna et al. found that pure NiO nanorods at room temperature exhibit a weak ferromagnetic phase due to the presence of a small hysteresis at the lower magnetic field, and a presence of antiferromagnetic phase [36]. The Fe doping increases the hysteresis compared to undoped NiO. Fe ions have two stable valence states Fe³⁺, and Fe²⁺, and the ferromagnetism may arise from Fe³⁺, or a mixture of Fe²⁺, and Fe³⁺ states [36]. The XRD results show six (111), (200), (220), (311), (222), and (400) characteristic peaks of cubic crystalline NiO, these same peaks appear for Fe-doped NiO, this suggests that there is no presence of an impurity phase when substituting Ni with Fe at some of the Ni sites. [36] The temperature dependence of the magnetic moment from room temperature to low temperature of Fe-doped NiO shows that FC and ZFC curves decrease when the temperature decrease and FC and ZFC curves split above the room temperature.

S. Philp Raja et al. found that impurity phase NiFe₂O₄ have effects on magnetic and dielectric properties of Fe-doped NiO [37].

According to Shaohui Liu et al.[38] the XRD of Ni_{1-x}Fe_xO (x = 0, 0.01, 0.02) shows five (111), (200), (220), (311), and (222) diffraction peaks characteristic of the NaCl-crystal structure. No lattice constants change, due to the increase of the Fe doping, was observed since ionic radii of Ni²⁺, Fe²⁺, and Fe³⁺ were quite close [38]. Both NiO and Fe-doped NiO samples show hysteresis, but the magnetic moment m(H) for NiO is

almost linear, characteristic of the antiferromagnetic phase, for both samples the FC curve decreases, and the ZFC curve increases as the temperature increases, and for each sample the FC and ZFC curves converge at around 300K [38].

J. Khemprasit et al. found that $\text{Fe}_{0.01}\text{Ni}_{0.09}\text{O}$ nanoparticles samples have the rock salt structure, and calcining them at different temperatures ranging from 400 to 1000 degrees Celsius does not affect their crystal structure [39]. J. Khemprasit et al. claim that the origin of the ferromagnetism is: (a) the double exchange interaction through Fe ions and defects (e.g Fe^*_{Ni}), and (b) the presence of ferromagnetic and / or ferrimagnetic impurities co-existed with the main phase [39]. Also they found that the crystallite size and the particle size increased when the calcining temperature increased because of grain growth during heat treatment [39]. They also claim that NiO is antiferromagnetic below the Neel temperature, but it becomes ferromagnetic if its crystallite size is less than 8 nm due to finite-size effect, since the reduction of the crystallite size results in the increase of the surface to volume ratio, and this causes the high value of uncompensated magnetic moments [39].

D.Y. Jiang et al. found that the optical band gap of NiO thin films deposited onto quartz substrates by the electron beam deposition technique ranges from 3.08 to 3.32 eV [40]. M. Tyagi et al. found that the static refractive index (n) of NiO thin films deposited by RF sputtering is about 2.48 [41]. M. Guziewicz et al. found that NiO thin films made using unbalanced magnetron sputtering from a 3" NiO target in an O_2 -Ar gas mixture at controlled temperatures from 300 up to 700 °C have the bandgap ranging from 3.4 to 3.58 eV [42]. A. Venter et al. found that the bandgap and the refractive index (n) of the oxidized Ni thin films depend on the oxidation temperature; the range for the bandgap

is from 3.37 eV at 350 degree Celsius to 3.76 eV at 600 degrees Celsius, and the refractive index (n) at 400 degrees Celsius is about 2.3 [43].

P.M. Ponnusamy et al. found that the bandgap for NiO and Fe-doped NiO nanoparticles prepared by wet-chemical process is 3.958 eV and 4.026 eV respectively [44].

II. NICKEL OXIDE AND PERMALLOY OXIDE

2.1 Nickel and Nickel Oxides

2.1.1 Nickel

Nickel is a chemical element which is symbolized by (Ni) and having an atomic number 28. Nickel is a silvery-white, hard and ductile material which belongs to transition metals in the periodic table of elements. It exhibits a mixture of ferrous and nonferrous metal materials. It was found that Nickel is present in most of meteorites, and is often used as one of the criteria for distinguishing a meteorite from other minerals. The bulk of nickel mined are either from laterites where the dominant ore minerals are nickeliferous limonite [(Fe,Ni)O(OH)] and garnierite (a hydrous nickel silicate), or magmatic sulfide deposits where the principal ore mineral is pentlandite [(Ni,Fe)₉S₈] [45], [46], [47]. And pure Nickel is easily reactive at room temperature forming principally NiO, N₂O₃, α -Ni(OH)₂, β -Ni(OH)₂, or NiOOH.

Ni atom has a total of ten valence electrons, eight electrons in the 3d orbital, and two electrons in the 4s orbital. Ni has a cubic-closed packed (CCP) crystal structure which is stable at pressures of at least 70 GPA. Ni belongs to a space group Fm3m with a space group number 225. Ni has the following unit cell parameters: a: 352.4 pm, b: 352.4 pm, c: 352.4 pm, α : 90.000°, β : 90.000°, and γ : 90.000°, where a, b, and c are lattice vectors, and α , β , and γ are lattice angles [48], [49]. As already mentioned, the oxidation of Ni can lead to a variety of chemical substances including NiO will also be the main subject of discussion in this thesis.

2.1.2 Nickel (II) Oxides and Permalloy Oxide

Pure Nickel is highly reactive with the air forming different Nickel Oxides depending on the nature of existing conditions. For instance, in the Physics Research Lab at Texas State University, optical properties of Ni thin films which were left at ambient air and room temperature underwent a logarithmic change over a period of several weeks, and optical characterization showed the formation of Nickel oxide (NiO), and possibly Ni(OH)₂. For artificial oxidation, non-stoichiometric NiO and NiFeO samples were obtained by the sputtering process, and samples were sputtered at both low and high oxygen concentrations to study the effect of oxygen vacancies on physical properties. Bulk NiO is an antiferromagnetic semiconductor material with a Neel temperature of about 523K.

2.1.3 NiO and Permalloy Oxide Crystal Structures

NiO adopts a face-centered cubic (FCC) structure with octahedral Ni (II) and O²⁻ sites, two Ni atoms in the unit cell, with a lattice constant (a) of 4.1705 Angstroms at 0K. Bulk NiO has a rhombohedral and cubic structure below and above the Neel temperature respectively [32], [50]. NiO also belongs to space group Fm3m, with a space group number 225. Below the Neel temperature, Ni²⁺ spin polarize in ferromagnetic configuration in the (111) planes along <112> axes, and the alternation of in-plane magnetization leads to the antiferromagnetic state. In the (FCC) structure, the in-plane magnetizations lead to magnetic domains. Figure 2.1 shows the crystal structure of NiO [51]. Any doping may cause structural stress in the crystal lattice which can be eliminated by structure relaxation, but the degree of stress depends on the amount and the atomic

size of the dopant. Both NiO and Permalloy Oxide were simulated using the same crystal structure since the XRD shows that they both have the rock salt structure.

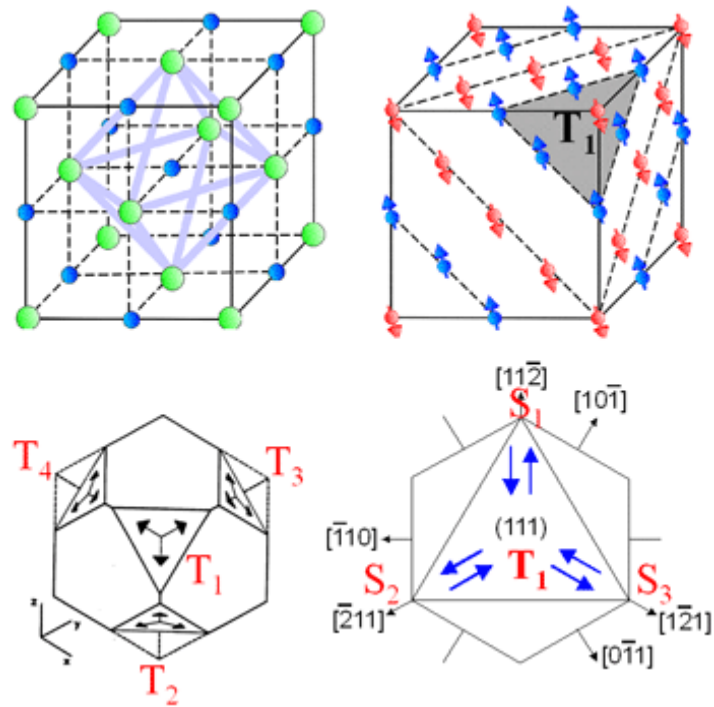


Figure 2.1 Crystal Structure of NiO with spin-polarization in the (111) planes. T and S are magnetic domains in [111], and [112] directions respectively.

III.COMPUTATIONAL THEORY

3.1 Early First Principle Calculations

The early known first principle calculations are the Hartree method, and the Hartree Fock method. The Hartree (H) method considers a one-electron model, instead of the n-electron system, by assuming that the n-electron system is just a set of non-interacting one-electrons where each electron interacts with others at an average. In the H method, the wave equation for the system is given by [52]:

$$\left(-\frac{1}{2}\nabla^2 + U_{ext}(\vec{r}) + U_H(\vec{r}) \right) \Psi(\vec{r}) = E\Psi(\vec{r}) \quad (3.1)$$

where $U_{ext}(\vec{r})$ is the interaction between the electrons and the nuclei, $U_H(\vec{r})$ is the Hartree potential resulting from the Coulomb repulsive interaction between each electron and the average field of others. The total energy of the system is the sum of energies of all electrons, since electrons are non-interacting. Consequently, the wave function for the system is the product of the one-electron wave function for each electron $\psi_i(\vec{r})$, this product is known as the Hartree product:

$$\Psi(\vec{r}_1, \dots, \vec{r}_n) = \prod_i \psi_i(\vec{r}_i) \quad (3.2)$$

The main issue with the (H) method is that it does not obey the principle of antisymmetry and the Pauli's principle, and yet the method does include the exchange and correlation potentials.

The Hartree-Fock (HF) method [53], [54] is the improved (H) method using variational process, and gives a proper description to the missing information in the (H) method. In the HF method, the wavefunction for an n-electron system is given by the Slater determinant [55] for the approximation of linear combination of non-interacting one-electron wave functions. For example, the wave function for a two-electron system is:

$$\Psi(\vec{r}_1, \vec{r}_2) = \frac{1}{\sqrt{2}} \begin{vmatrix} \psi_1(\vec{r}_1) & \psi_2(\vec{r}_1) \\ \psi_1(\vec{r}_2) & \psi_2(\vec{r}_2) \end{vmatrix} = \frac{1}{\sqrt{2}} [\psi_1(\vec{r}_1)\psi_2(\vec{r}_2) - \psi_2(\vec{r}_1)\psi_1(\vec{r}_2)] \quad (3.3)$$

The above determinant takes such form because of the antisymmetry principle, since electrons are fermions:

$$\Psi(\vec{r}_1, \vec{r}_2) = -\Psi(\vec{r}_2, \vec{r}_1) \quad (3.4)$$

By taking in account of the spin state for each electron, the exact Slater determinant as a combination of $\psi_1(\vec{r}_1, \uparrow)$, $\psi_1(\vec{r}_1, \downarrow)$, $\psi_2(\vec{r}_2, \uparrow)$, and $\psi_2(\vec{r}_2, \downarrow)$, takes the following form:

$$\Psi(\vec{r}_1, \vec{r}_2, \uparrow, \downarrow) = \frac{1}{\sqrt{2}} \begin{vmatrix} \psi_1(\vec{r}_1, \uparrow) & \psi_2(\vec{r}_1, \downarrow) \\ \psi_1(\vec{r}_2, \uparrow) & \psi_2(\vec{r}_2, \downarrow) \end{vmatrix} \quad (3.5)$$

The above Slater determinant satisfies the Pauli's principle for the wave function vanishes once two electrons occupy the same spin state.

The Slater determinant for an n-electron system, without taking in account the spin state for each electron, has the following form [53], [56], [57], [58]:

$$\Psi(\vec{r}_1, \vec{r}_2, \dots, \vec{r}_n) = \frac{1}{\sqrt{n!}} \begin{vmatrix} \psi_1(\vec{r}_1) & \psi_2(\vec{r}_1) & \cdots & \psi_n(\vec{r}_1) \\ \psi_1(\vec{r}_2) & \psi_2(\vec{r}_2) & \cdots & \psi_n(\vec{r}_2) \\ \vdots & \vdots & \vdots & \vdots \\ \psi_1(\vec{r}_n) & \psi_2(\vec{r}_n) & \cdots & \psi_n(\vec{r}_n) \end{vmatrix} \quad (3.6)$$

And the wave equation for the HF case is obtained by rewriting the wave equation for the H case in terms of the Slater determinant as a wavefunction is:

$$\left(-\frac{1}{2} \nabla^2 + U_{ext}(\vec{r}) + U_{ij}(\vec{r}) \right) \Psi(\vec{r}) = E \Psi(\vec{r}) \quad (3.7)$$

where $U_{ij}(\vec{r})$ is the electron–electron interaction which stands for classical and quantum contribution of electrons to the system. The energy of the system can be obtained from the inner product of the Hamiltonian:

$$E = \sum_{i,j} \int \Psi_i^* \left(-\frac{1}{2} \nabla^2 + U_{ext}(\vec{r}) + U_{ij}(\vec{r}) \right) \Psi_i(\vec{r}) dr \quad (3.8)$$

Since the electrons are in interaction, the wavefunction as a Slater determinant is not accurate, so the improvement comes from the variational principle. The ground state (GS) energy is determined by the variational principle [53]. In quantum physics, without degeneracy, the lowest energy corresponds to the ground state, and minimizing the energy of the system with respect to the wave function leads to the ground state energy.

$$0 = \delta \left(\int \Psi \hat{H} \Psi dr \right)_{GS} \quad (3.9)$$

3.2 Density Functional Theory

The Schrodinger's equation is one of the brilliant achievements in the modern science; unfortunately the equation is easily applicable for very simple quantum systems due to difficulties resulting from many-particle quantum effect. However, many-body systems can be approximately solved using the density functional theory (DFT).

This is a powerful computational quantum mechanical modeling approach used in physics, chemistry and materials science to calculate the (ground state) [59] properties of many body systems. For the last three decades, DFT has been the most successful method for the quantum mechanical simulation of periodic systems and nowadays it is widely used in modeling of energy surfaces in molecules and even inner compositions of planets. The central idea of the theory consists of expressing the electron density $n(\vec{r})$ in terms of the one-electron wave-function [59], [60] $\psi_i(\vec{r})$:

$$n(\vec{r}) = \sum_i |\psi_i(\vec{r})|^2 \quad (3.10)$$

By including the spin, the wave-function takes the spinor form, where the first and the second elements of the spinor stands for spin up and spin down respectively:

$$\psi_i(\vec{r}) = \begin{pmatrix} \phi_{i\alpha}(\vec{r}) \\ \phi_{i\beta}(\vec{r}) \end{pmatrix} \quad (3.11)$$

And the complex conjugation of the spinor which has two elements leads to a form of the electron density matrix with four elements:

$$\tilde{n}(\vec{r}) = \sum_i \begin{pmatrix} |\phi_{i\alpha}(\vec{r})|^2 & \phi_{i\alpha}(\vec{r})\phi_{i\beta}(\vec{r})^* \\ \phi_{i\alpha}(\vec{r})^*\phi_{i\beta}(\vec{r}) & |\phi_{i\beta}(\vec{r})|^2 \end{pmatrix} \quad (3.12)$$

Also, the electron density matrix can be expanded into the electron density and the magnetization density.

However, even with electron density, difficulties for solving the problem for many-electron system remain since the Hamiltonian of the system is extremely complex (complicated), thus a sets of particular methods need to be utilized to satisfy the Schrodinger equation for the system, and one of these special methods is Born-Oppenheimer Approximation which was previously discussed briefly in the introduction.

3.2.1 Born-Oppenheimer Approximation

If we decide to describe the properties of a collection of N atoms of 3N degrees of freedom; for instance, one of the necessary things that would need to be known about the energy is the change in energy if some atoms are moved with respect to others. To indicate the position of each atom we need to know the location of both the nuclei and electrons, since the electrons are not much heavier than nuclei, they tend to respond rapidly to any change. Thus the kinetic energy of nuclei is negligible, and then the Born-Oppenheimer approximation guarantees that electronic and nuclear motions can be studied independently. The separation of these two types of motions is given by the equation (1.46). In the first step of the above approximation, one solves Schrodinger's equation for fixed atomic nuclei, and the wave function depends on the electrons only. And in the second step, one solves the Schrodinger's equation for nuclei only, with the

electronic wave function serving as a potential [16]. The adiabatic potential energy surface of the atoms having M nuclei situated at positions $\vec{r}_1, \dots, \vec{r}_M$ is the ground state energy function of the form; $E(\vec{r}_1, \dots, \vec{r}_M)$.

3.2.2 Hohenberg-Kohn Theorems

These theorems are the basis for density functional theory, because they allow the determination of the ground-state properties of a system without dealing with many-electron states $|\psi_i\rangle$. Since our system has N electrons moving in a static potential, the normalization condition can be written as; $\langle \psi_i | \psi_i \rangle = N$.

These theorems are based on an important assumption that any physical system can be regarded as a collection of electrons moving in the field of an external potential $U_{ext}(\vec{r})$. The first theorem states that the ground-state energy from the Schrodinger's equation is a unique functional of the electron density $n(\vec{r})$, where \vec{r} is the position vector. The energy functional $E[n(\vec{r})]$ can be written in terms of the external potential as follows [59], [60]:

$$E[n(\vec{r})] = \int n(\vec{r})U_{ext}(\vec{r})d\vec{r} + F[n(\vec{r})] \quad (3.13a)$$

or,

$$E[n(\vec{r})] = \langle \psi_i | \hat{H} | \psi_i \rangle \quad (3.13b)$$

Here, F is an unknown quantity, but universal functional of the electron density $n(\vec{r})$.

This means that there exists an injective mapping between the ground-state wave function and the ground state electron density function.

Even though the first theorem claims that the functional of the electron density satisfies the Schrodinger's equation, it does not give the details about the nature of the functional. It is the second theorem that defines the functional in the following way: the electron density that minimizes the energy of the overall functional satisfies the Schrodinger's equation. Then, if the functional is known, a true electron density can be obtained by simply varying an arbitrary to minimize the functional. The functional described by the Hohenberg-Kohn theorem can be written in terms of a one-electron wave function $\psi_i(\vec{r})$, and the energy functional is given by the equation [62]:

$$\begin{aligned}
E[\{\psi_i\}] = & -\sum_i \int \psi_i^* \nabla^2 \psi_i d^3r + \int U(\vec{r})n(\vec{r})d^3\vec{r} \\
& + \frac{1}{2} \iint \frac{n(\vec{r})n(\vec{r}')}{|\vec{r} - \vec{r}'|} d^3\vec{r}d^3\vec{r}' + E_{xc}[\{\psi_i\}] + \{E_{ion}\}
\end{aligned} \tag{3.14}$$

Here, the functional includes five terms: the first term is the electron kinetic energy, the second term is the Coulomb interaction between the electrons and the nuclei, the third term is the Coulomb interaction between pairs of electrons, the fourth term is the exchange-correlation functional that includes all additional quantum mechanical effects, and the last term is the Coulomb interaction between pairs of nuclei.

3.2.3 Kohn-Sham Equations

A Kohn-Sham Subsystem is a quantum system of non-interacting fermions moving in the external potential field. Kohn and Sham found that the right electron $n(\vec{r})$ density can be achieved by solving a set of Schrodinger equations called Khon-Sham equations [63] of non-interacting particles in which each equation only involves one

particle, in other words, with the Kohn-Sham approach, the n-electron system is replaced by a one-electron system. The solution obtained by using the Kohn-Sham approach is a single Slater determinant of the set of orbitals corresponding to the lowest energy eigenvalues to the following Kohn-Sham equations [60], [62]:

$$\left[-\frac{1}{2}\nabla^2 + U(\vec{r}) + \underbrace{\int \frac{n(\vec{r}')}{|\vec{r}-\vec{r}'|} d^3\vec{r}'}_{U_{eff}} + U_{xc}(\vec{r}) \right] \psi_i(\vec{r}) = \varepsilon_i \psi_i(\vec{r}) \quad (3.15)$$

Here, the orbitals ψ_i are the solutions to the KS equations, ε_i are the energy eigenvalues, the first term in the Hamiltonian for KS equations is the kinetic energy, the second term stands for the interaction between an electron and a collection of nuclei, and the third term stands for the Coulomb interaction between the electron and the total electron density, and is called Hartree potential and is defined by [63]:

$$U_H(\vec{r}) = \int \frac{n(\vec{r}')}{|\vec{r}-\vec{r}'|} d^3\vec{r}' \quad (3.16)$$

The self- interaction is represented by the fourth term, and stands for the exchange and correlation potential, and is related to the exchange correlation energy through the following functional derivation:

$$U_{xc}(\vec{r}) = \frac{\delta E_{xc}(\vec{r})}{\delta n(\vec{r})} \quad (3.17)$$

As mentioned before, to find the electron density, it is required to solve the Kohn-Sham equations, but the Hartree potential has to be defined, however defining the

Hartree potential requires the knowledge of the electron density [64], and to know the electron density, the single-electron density should be known, but knowing them requires solving the Kohn-Sham equations. In other words, the problem requires executing the following algorithm [65]:

1-Defining an initial guess electron density $n(\vec{r})$

2-Solving the Kohn-Sham equations using the trial (guess) electron density to find the single-electron wave functions, $\psi_i(\vec{r})$

3-Using the Kohn-Sham single-particle wave functions from step 2, to determine the electron density: $n_{KS}(\vec{r}) = 2 \sum_i \psi_i(\vec{r}) * \psi_i(\vec{r})$ (fermionic systems)

4-Comparing the electron density $n_{KS}(\vec{r})$ with the trial electron density, $n(\vec{r})$, and if both are the same, that is the ground state electron density, then the total energy of the system can be calculated by utilizing that calculated electron density. If they are different, the process should be repeated with new trial values of electron density until both electron densities become approximately identical [67]. The iterative variation approach (self-consistent loop) is shown in the Figure 3.1.

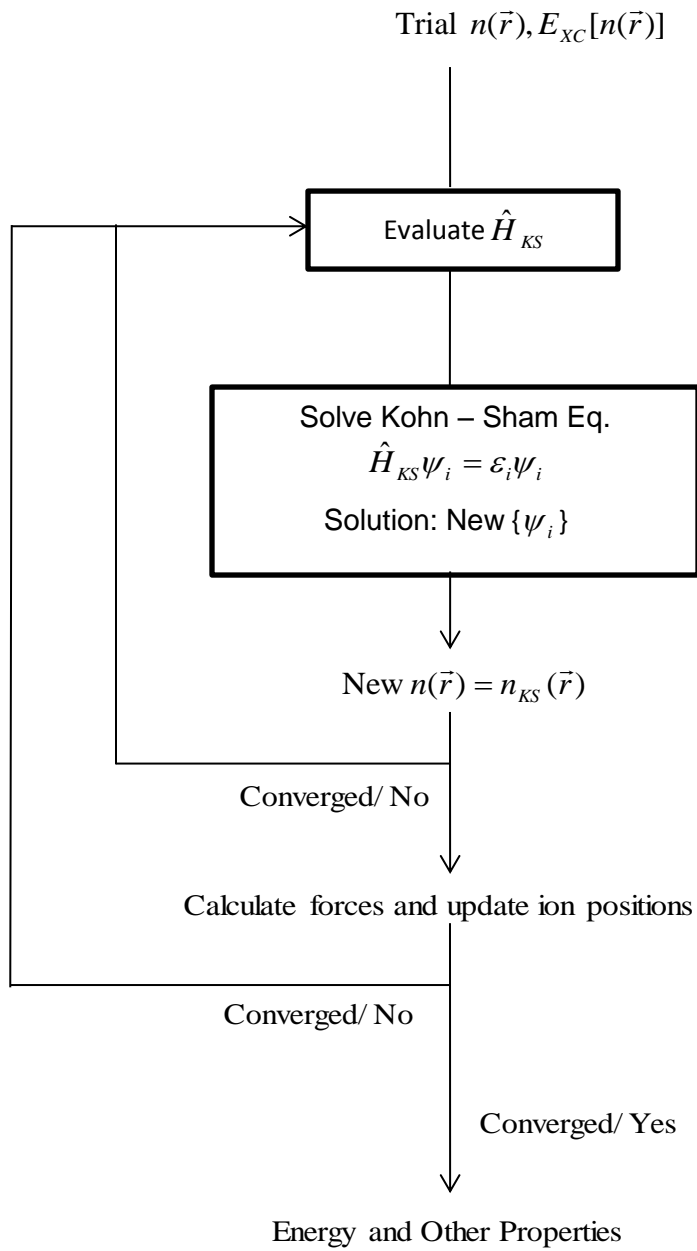


Figure 3.1 Self-Consistent Loop for Density Functional Theory.

With the Bloch theorem, the function $u_k(\vec{r})$ is a periodic function [68], and according to the Fourier theorem, it can be written as a Fourier series, thus the wave function has the form:

$$u_k(\vec{r}) = \sum_{\vec{G}} c_k(\vec{G}) \exp[i(\vec{k} + \vec{G}) \cdot \vec{r}] \quad (3.18)$$

As mentioned before, \vec{G} is the reciprocal lattice vector. And Kohn-Sham (KS) equations can be written in terms of the Fourier transforms:

$$\left(-\frac{1}{2} \nabla^2 + U_{eff} \right) \sum_{\vec{G}} c_n(\vec{k} + \vec{G}) \exp[i(\vec{k} + \vec{G}) \cdot \vec{r}] = \varepsilon_{nk} \sum_{\vec{G}} c_n(\vec{k} + \vec{G}) \exp[i(\vec{k} + \vec{G}) \cdot \vec{r}] \quad (3.19)$$

Since the effective potential can be written in terms of the plane wave (PW) basis set, by expressing the kinetic energy in terms of \vec{k} and \vec{G} , then Kohn-Sham equations can be written in the condensed matrix form, for example, the 3x3 matrix KS Hamiltonian at arbitrary band index n can be written as follows:

$$\begin{bmatrix} \frac{1}{2}(\vec{k} - \vec{G})^2 & U_{eff} & 0 \\ U_{eff} & \frac{1}{2}(\vec{k})^2 & U_{eff} \\ 0 & U_{eff} & \frac{1}{2}(\vec{k} + \vec{G})^2 \end{bmatrix} \begin{bmatrix} c_{k-G} \\ c_k \\ c_{k+G} \end{bmatrix} = \varepsilon_k \begin{bmatrix} c_{k-G} \\ c_k \\ c_{k+G} \end{bmatrix} \quad (3.20)$$

In any material, there is the formation of bands, bands which are occupied by electrons are called the valence band, and the unoccupied bands are called the conduction band, and the band-structure is obtained by plotting the energy as a function of the Fourier space known as k-points space. Another representation of the electronic structure

is the density of states (DOS), which is the number of electronic states per unit energy range.

3.2.4 Exchange-Correlation Functional(s)

The KS equations do not succeed to accurately describe real systems for the KS method does not fully include the exchange-correlation (XC) energy since, as already mentioned, the KS method is for one-electron systems instead of n-electron systems. Even though, in the formulation of the theory of density functional(s), this energy counts for less than ten percent of the total energy, it plays a major role in determining important physical system properties such as spin-polarization, or band gap formation. Thus, the accuracy of the DFT calculations depends on the best approximation of the XC energy [69]. This energy is related to effective reduction of electron density or XC hole which is due to the repulsion between electrons. The XC hole comprises exchange and correlation components, and at high electron densities, due to Pauli Exclusion Principle the XC hole is mainly dependent of the exchange component, and at lower densities the correlation component becomes important. The electrostatic energy of an electron at position \vec{r} with XC hole at position \vec{r}' is the local XC energy per electron, and can be expressed as follows:

$$\varepsilon_{XC}[n(\vec{r})] = \frac{1}{2} \int \frac{n_{XC}^{hole}(\vec{r}, \vec{r}')}{|\vec{r} - \vec{r}'|} d\vec{r}' \quad (3.21)$$

And the integral of the product of the electron density and the local XC energy per electron is the XC energy functional [69]:

$$E_{XC}[n(\vec{r})] = \frac{1}{2} \iint \frac{n(\vec{r})n_{XC}^{hole}(\vec{r}, \vec{r}')}{|\vec{r} - \vec{r}'|} d\vec{r}d\vec{r}' \quad (3.22)$$

The approximate value of the XC energy can be achieved by assuming that the overall electron density is equivalent to the local electron density. With this idea of localized XC hole, the physical system is regarded as a collection of many pieces of uniform density with distinct values, and the total XC energy is the sum of all energies for individual pieces. This is called the local density approximation (LDA) [70]. This method is accurate for systems with almost zero gradient electron densities or homogeneous electron gases. For instance, for a homogenous gas of exchange-correlation energy per electron $\varepsilon_{XC}^{hom}[n(\vec{r})]$ the functional is given by:

$$E_{XC}^{LDA}[n(\vec{r})] = \int n(\vec{r})\varepsilon_{XC}^{hom}[n(\vec{r})]d\vec{r} \quad (3.23)$$

By considering the spin variable for spin-polarized systems, the LDA is extended to the spin-polarized density approximation (LSDA), and the XC energy functional for the system is written as:

$$E_{XC}^{LDA}[n_{\uparrow}(\vec{r}), n_{\downarrow}(\vec{r})] = \int n(\vec{r})\varepsilon_{XC}^{hom}[n_{\uparrow}(\vec{r}), n_{\downarrow}(\vec{r})]d\vec{r} \quad (3.24)$$

However, real physical systems are not homogeneous; they do really not have uniform electron density. Then the application of the LDA for real systems do not guarantee a precise result. More accurate XC functional(s) are obtained by the generalized gradient approximation (GGA) method [71], [72] which includes electron

density and its local gradient. The general XC energy functional, depending on the spin variable with the density gradient, is given by:

$$E_{XC}^{GGA}[n_{\uparrow}(\vec{r}), n_{\downarrow}(\vec{r})] = \int n(\vec{r}) \mathcal{E}_{XC}^{GGA}[n_{\uparrow}(\vec{r}), n_{\downarrow}(\vec{r}), \nabla n_{\uparrow}(\vec{r}), \nabla n_{\downarrow}(\vec{r})] d\vec{r} \quad (3.25)$$

While the XC energy functional for GGA has no both simple and correct form, its general form can be expressed in terms of the exchange-correlation energy LDA. Beyond GGA, there are other XC functionals which include additional variables to produce better accuracies.

IV.COMPUTATIONAL APPROACH

4.1 Brillouin Zone Sampling

In the reciprocal space, the primitive cell is the first Brillouin zone (BZ) [73], and symmetry operations such as rotation and inversion can reduce the first BZ to the irreducible BZ, and fold certain k-points a number of times, these special k-points are called points of high symmetry.

While constructing the first BZ follows the same procedure in either two or three dimensions, the construction in latter dimensions is more difficult. In two dimensions, it can be constructed by drawing a reciprocal lattice, and lines from a reference lattice point to its nearest neighbors and bisect the lines perpendicularly. In three dimensions, the first BZ is the volume formed by surfaces taking at same bisecting lines from the Gamma point to its neighbors. An example of the first BZ is shown in Figure 4.1. Also there exist BZs of high order centered at the Gamma point; however all of them play the same role due to the periodicity of the reciprocal lattice, all k-points outside the first BZ are the same since they differ by the reciprocal lattice vector \vec{G} .

Sampling the first BZ is important for the DFT calculations because few k-points reduce the computational time, and enough k-points represent accurately the system. Normally any point in the first BZ is a k-point, thus there exists an infinite number of k-vectors for the wave function. However, because of the smoothness of the wave function over the first BZ, a finite number of k-points is sufficient. The choice of necessary number of k-points depends on the convergence of the energy, in other words, good convergence of the total energy corresponds to sufficient k-points.

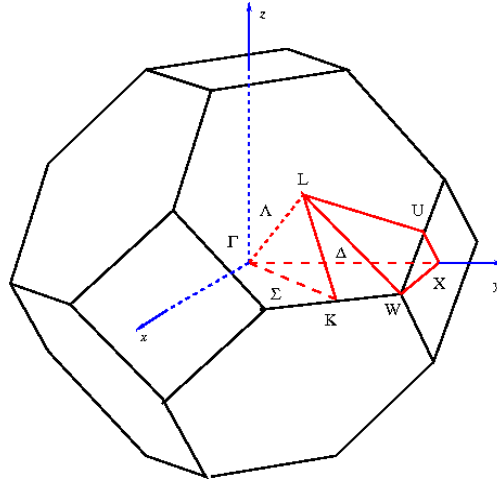


Figure 4.1 First Brillouin Zone (BZ) of (FCC) lattice with some points and lines of high symmetry.

4.2 Bandstructure and Density of States (DOS)

In isolated atoms, electrons occupy specific and discrete energy levels, but when they come together, there is a formation of bands. Almost all core electrons remain in initial locations because of strong interaction with the nuclei, however valence electrons try to occupy the same energy level. The electronic structure is represented with the spectrum of energy curves in the k-space which is called the bandstructure. Figure.4.2 shows an example of the bandstructure for Si [74]. Also a representation of the density of states (DOS), which is the number of electronic states per unit of energy range, is another way to characterize the electronic structure.

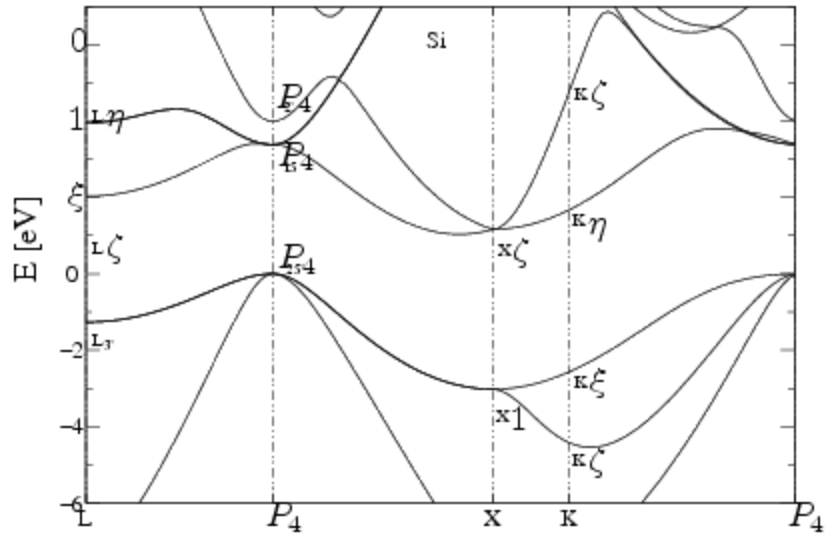


Figure 4.2 Bandstructure for Si. The valence band and the conduction band are below and above the Fermi energy level ($E_F=0$) respectively.

The reaction of valence electrons to the nuclei can lead to the formation of band gap. The band gap width and its location with respect to the Fermi level also play role for the physical description of materials.

4.3 Generalized Gradient Approximation (GGA)

In comparison with other calculation methods such as LDA, the GGA method describes very well almost all systems [75], [76] with error less than to 4% for some properties. The method solves most of overbinding issues of LDA. However the GGA method has some limitations. One of the widely known limitations is that the GGA approach fails to describe strongly correlated systems such as transition metal oxides for orbitals of such systems are strongly localized, thus there is an additional repulsive interaction between each pair of electrons. In addition, like the LDA method, the GGA

method fails to accurately describe the band gap [77], [78]. On one hand, the failure is caused by GGA's inaccessibility to excited states; the GGA method is based on the noninteracting one-electron Kohn-Sham (KS) model in which the definition of the band gap is different from the true definition of the band gap. On the other hand, the failure results from an incomplete cancelation of the self-interaction due to the nature of XC energy.

4.4 Beyond Generalized Gradient Approximation (GGA)

For strongly correlated systems, the GGA can be extended to GGA+U method, also called the U-approach which consists of adding the energy U to the GGA Kohn-Sham (KS) Hamiltonian [79], [80] to improve the DFT calculations. This approach has been reported to improve many physical system properties such as band gap, or magnetic moment. Otherwise, the correction for the band gap underestimation may be achieved by using advanced techniques such as hybrid functionals [81], Green function techniques, GW approximation or other self-interaction correction methods, however, unlike the GGA method or the U-approach, most of the above methods are computationally expensive. Thus, all DFT calculations in this thesis research were performed with the GGA/U-approach.

4.5 VASP Simulations

VASP (Vienna Ab initio Simulation Package) [65], [82] is software for electronic structure and quantum mechanical modeling of physical systems. VASP solves the many-body Schrodinger's equation approximatively either within the DFT or within the HF method, or within a mixture of both as Hybrid functionals. VASP calculations require at least four input files: INCAR, POSCAR, POTCAR, and KPOINTS.

The INCAR file is the central brain for the calculations because it contains the lines of codes (flags) about the run. The POSCAR file contains the information about the structure of the system to simulate. The POTCAR file contains pseudopotential or PAWs and XC functional information for atoms of the system. And the KPOINTS file contains coordinates and symmetry specification for k-points in the BZ. In general, the computational time depends on the number of electrons in the system, the content of the INCAR file, or the computational method. Advanced calculations for many-electron systems are extremely costly due to either the colossal amount of required computing power or computation time. Once the calculation is complete, several files containing the result of the run are returned, and frequently used output files are: OUTCAR, CONTCAR, DOSCAR and CHGCAR.

The OUTCAR file contains most of the output information from the run along with the input file, for example the information about the bandstructure, the density of states or dielectric constants can be easily extracted from the OUTCAR file. The CONTCAR file contains the information about atomic positions after the calculation is complete. The DOSCAR file contains the total DOS and partial DOS information.

Normally the DOSCAR file obtained directly from the relaxation process are useless for DOS, accurate DOS information requires running a static calculation using the result the converged calculation, with the CONTCAR as POSCAR file. And finally, the CHGCAR file contains the lattice vectors, atomic coordinates and the charge density after the run.

4.6 Simulation Methods

Various VASP simulations for NiO and Fe-doped NiO were performed. The results were compared with previous findings in the literature. Simulations for Fe-doped NiO were utilized to learn about of the effect of Fe doping on the electronic, optical and magnetic properties of NiO.

The first simulations were for NiO crystals, and the main reason was to directly facilitate next simulations, given that the Permalloy (NiFe) oxide can be obtained from NiO by replacing Ni atoms with Fe atoms, and also to ease the study because any change in physical properties had to be attributed to the Fe doping.

The first simulations of NiO were done with a simple cubic lattice structure. Above the Neel temperature NiO has an FCC (NaCl-type) structure but we chose to simulate it in the simple cubic (SC) structure to reduce the amount of time for VASP calculation and learn more about NiO system. We recall that the NaCl-type structure can be described in two ways: a) an FCC lattice plus two basis atoms or b) a SC lattice + eight basis atoms.

Preliminary calculations were done with SC lattice + eight basis atoms: four Nickel and four oxygen (O) atoms (see Figure 4.3). The first calculations were for the self-consistency calculations and the investigation of the crystal structure stability. Since the crystal structure stability corresponds to k-points with the lowest total energy, several simulations were performed with different k-points in the (BZ) in search for the k-points with the lowest total energy. Used k-points were: (2x2x2), (4x4x4), (6x6x6), (8x8x8), (10x10x10), and (12x12x12), and the calculations showed that the stable NiO corresponded to (4x4x4) k-points. This is probably one of the reasons why these k-points were previously used for NiO first principles calculations, as published in [83], and other works.

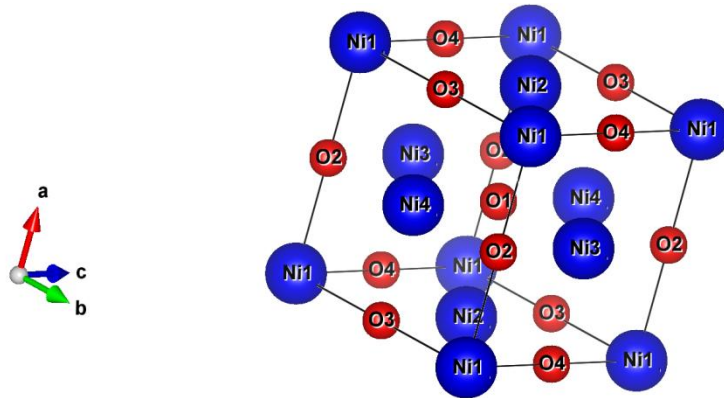


Figure 4.3 FCC (SC lattice + eight basis atoms) Structure for NiO. The lattice parameters of the above supercell are twice those of the unit cell. The lattice constant for the unit cell of NiO is about 4.17 Angstroms.

Spin calculations were also performed. More specifically one no-spin polarized (ISPIN=1) calculation, and another spin polarized (ISPIN=2) calculation. The comparison between the total energies from both calculations showed that the total energy for the spin-polarized calculation was lower than that of the no-spin polarized calculation, which means that the electron charge density is not distinguished by spins. Next, calculations with or without (ISPIN =2), MAGMOM tags were performed, and calculations with these tags yielded the lower total energy than those without them, since Ni atoms were given a unique non-zero magnetic moment for every different calculation, this indicates that each atom in NiO has a magnetic moment.

To study the type of magnetism of NiO, the energies for both ferromagnetic (FM) and anti-ferromagnetic (AFM) configurations were calculated by choosing sequences in which all spins of Ni atoms are up or down, or sequences of up and down spins of Ni atoms in the MAGMOM tag. Each Ni atom was assigned a magnetic moment value, +2 for the spin-up state and -2 for the spin-down state, and all O atoms were given a zero magnetic moment value each. And by total energy comparison technique, the simulations showed that the ferromagnetic NiO was more likely to be stable, which is a contradiction since, as already mentioned, the bulk NiO is antiferromagnetic. However, the difference in total energies for both configurations was extremely small, but non-negligible.

Since the DFT calculations are normally done at zero Kelvin (K), so it was necessary to consider the crystal structure of NiO at such temperature, which is a distorted structure along the [111] direction, also known as, the rhombohedral structure.

In addition, since all previous calculations were done with GGA method which does not fully describe the system, thus the application of the U-approach was also necessary, and the correction for exchange-correlation interactions was U-J, with $J = 0$. The Hubbard correction U for both NiO, and Fe-doped NiO, only involved d-orbitals for both Ni, and Fe atoms. Different U values were utilized for studying the Hubbard (U) effect on the bandgap, but the study of Fe effect required the use of the same U for both NiO and Fe-doped NiO.

In this case, the NiO crystal structure was increased from a unit cell to a supercell with both the cubic (FCC) structure and rhombohedral structure with antiferromagnetic (Ni) ordering in the (111) planes, and since NiO is supposed to be rhombohedral at zero Kelvin (K), calculations with cubic structure were carried out only for a test, thus only rhombohedral structures are displayed. Each structure had either 4 atoms: 2 Ni and 2 O atoms, or 32 atoms: 16 Ni atoms and 16 O atoms. At least four different types of calculations were done, and at least two calculations for each type of structure.

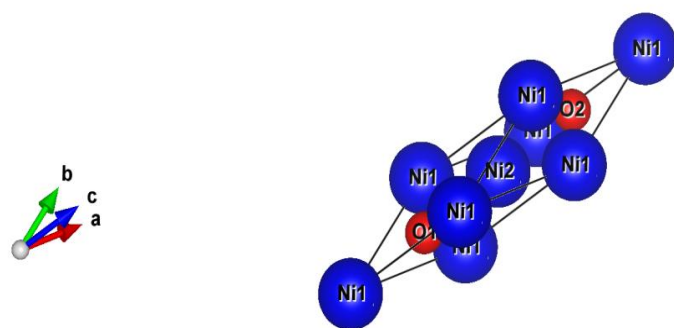


Figure 4.4 Rhombohedral Structure of a 4-atom NiO. Antiferromagnetic (Ni) ordering in (111) planes.

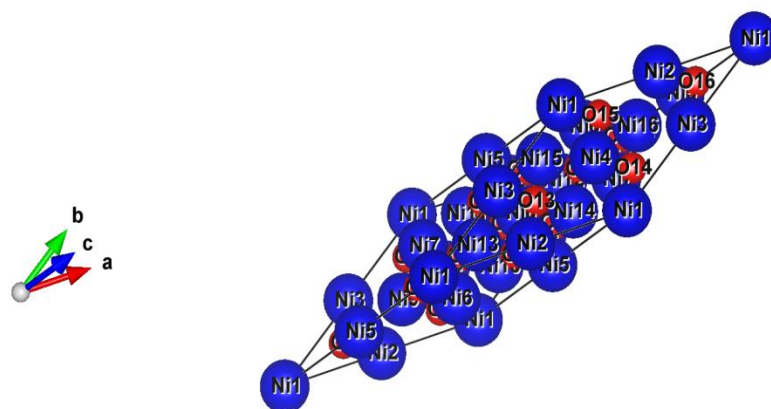


Figure 4.5 Rhombohedral Structure of a 32-atom NiO Supercell. Antiferromagnetic (Ni) ordering in (111) planes.

Calculations with NiO supercells with both cubic (FCC), and rhombohedral structures, showed that the total energy obtained with spin polarization was greater than that with non-spin polarization for each structure, which is in agreement with the previous calculation with NiO unit cells that up and down spins in NiO are free to have different spatial orbitals. In addition, calculations with MAGMOM showed less total energy than calculations without MAGMOM for each structure, and calculations with the AFM configuration yielded less total energy than the FM configuration, however, the total energy with either AFM or FM configuration for the cubic structure was greater than the total energy for the AFM configuration for the rhomboidal structure. This indicates that the bulk NiO is indeed AFM with the rhombohedral structure at zero Kelvin (K).

Some similarities were observed for both FCC and rhombohedral structures, for example, for each of structures, the total force was zero, however most of ions were extremely stressed, relaxation calculations were carried out to reach the self-consistency condition (with a fully relaxed system). Five calculations for structural and ionic relaxations (ISIF=2) were performed for thirty ionic steps to reach an acceptable force on each ion less or equal than 0.001 eV/Angst. In addition, the static calculation was done, and the result from the static calculation was used to obtain the (DOS). Normally the space group is not identical for FCC and rhombohedral structures, while the space group of the FCC structure belongs to the space group Fm3m (225), the rhombohedral structure belongs to the space group R3m (166). For the (BS) bandstructure, additional calculations with different paths of high symmetry points in the (BZ) shown by Figure 4.5, to obtain the Fourier space energy.

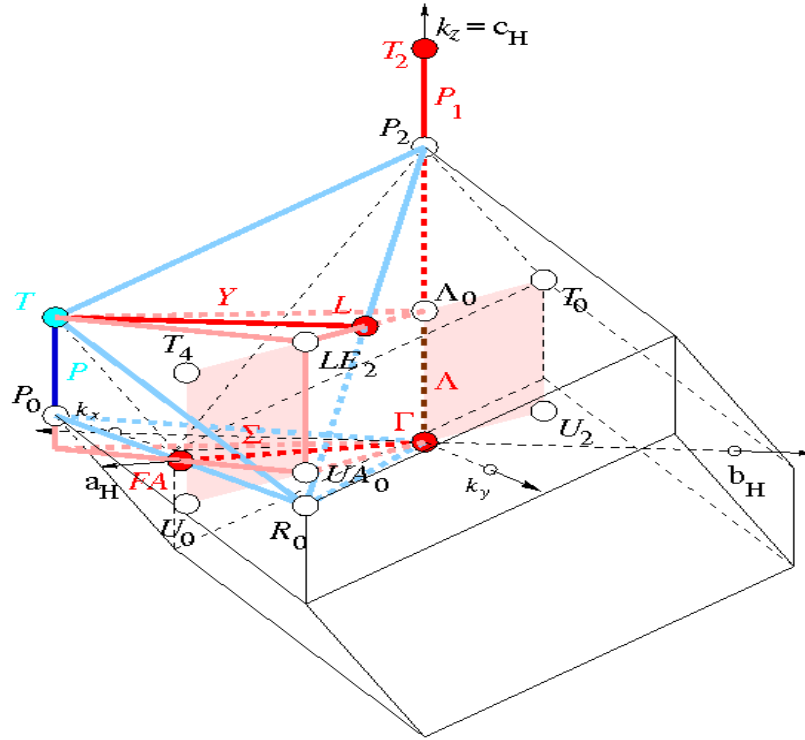


Figure 4.6 Brillouin zone (BZ) along with high symmetry points for the rhombohedral structure for NiO, or Fe-doped NiO.

After the simulation of Nickel Oxide, four types of simulations for Nickel oxide doped with Iron were done. All simulations were performed using a supercell, in a rhombohedral structure in the (111) planes, of 32 atoms: one Fe atom, 15 Ni atoms, and 16 O atoms in the AFM configuration. Thus, in comparison with NiO simulations, a concentration of 6.25% Fe was considered in these simulations. The magnetic moment for Fe atom was randomly chosen to be $5 \mu_B$, but VASP adjusted that value during the calculation.

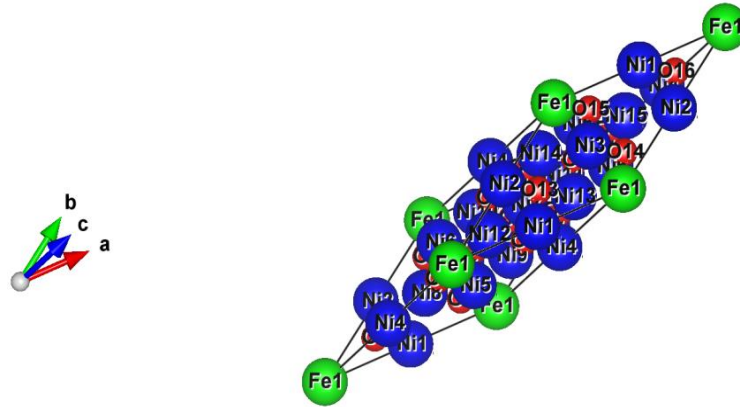


Figure 4.7 Rhombohedral Structure of Fe-doped NiO Supercell (32 atoms). Anti-ferromagnetic ordering for both (Ni) and (Fe) in the [111] direction.

First, two calculations were performed to learn whether or not Fe-doped NiO was magnetic, one calculation was done without MAGMOM tag, and another with MAGMOM tag, and with total energies comparison from both calculations showed that Fe-doped NiO was magnetic. The last two calculations with MAGMOM were done, with one in the AFM configuration, and another in the FM configuration. The energy from the calculation with no MAGMOM was extremely higher than energies from other calculations, and the energy from the calculation with spins of atoms being up and down alternatively was lower than the energies from simulations with all spins of atoms being either up or down, but the non-zero magnetic moment indicated that Fe-doped NiO was not antiferromagnetic, and this makes sense because only one Ni was substituted by Fe atom by keeping the same spin ordering.

Also Fe-doped NiO ions were stressed, thus the relaxation was needed to significantly reduce forces on ions. After several relaxations, the self-consistent result was obtained, and then used, along with different paths of the K-points in the Brillouin zone, to generate the bandstructure and densities of states.

V.COMPUTATIONAL RESULTS

5.1 Optical and Magnetic Properties of NiO

The GGA calculations for 4-atom NiO yielded a band gap, however with the same type of the calculation for 32-atom NiO the band gap was not present; this is due to the exchange-correlation interactions that increase with the number of interacting particles, especially for strong correlated systems.

According to the crystal field theory, Ni atoms in NiO have an octahedral coordination, 3d orbitals are split such that the conduction band minimum is made of e_g states, and the valence band maximum is made of a mixture of e_g and t_{2g} states.

Figure 5.1 shows the band structure and density of states for a 4-atom NiO from the GGA calculations. According to the results, NiO has an energy gap E_g of about 0.6 eV with respect to the Fermi energy level ($E_F = 0$ eV) at the valence band maximum. Since this electronic gap has a small but non-zero energy, then intrinsic NiO is a semiconductor.

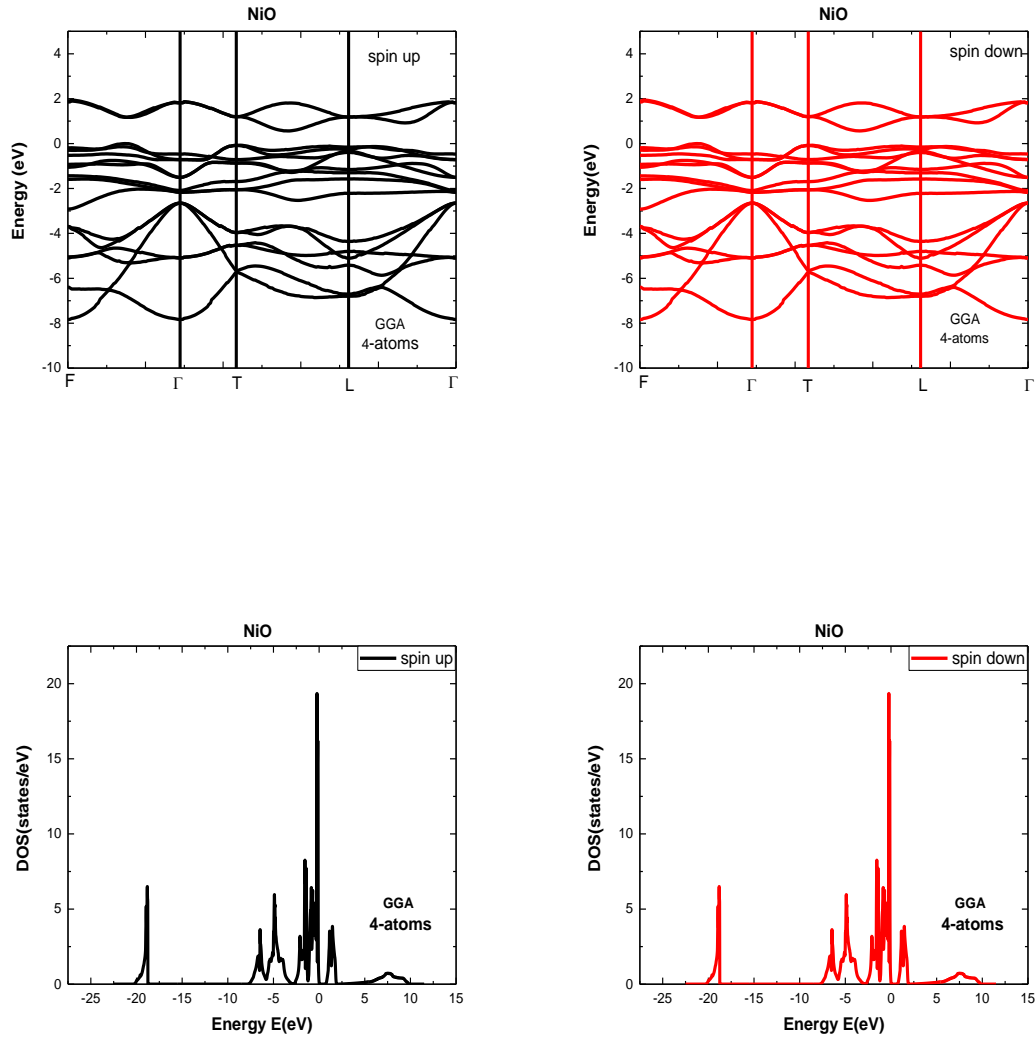


Figure 5.1 Bandstructure (BS) and density of states (DOS) for both spin up and spin down states obtained for a 4-atom NiO using GGA. The Fermi energy level is set at the origin ($E_F = 0$ eV) at the valence band maximum. Measured from the Fermi energy level, the band gap is $E_g = 0.6$ eV.

According to the above result, the spin-up bandstructure is identical to the spin-down bandstructure; consequently, the total magnetic moment is zero. Table 5.1 shows the magnetization for each orbital and the total magnetization for 4-atom NiO. The first two ions correspond to Ni atoms, and others correspond to O atoms. The total magnetization is zero, as expected since the bulk NiO is antiferromagnetic.

Table 5.1 Magnetic moment (in μ_B) obtained for 4-atom NiO using GGA. The first two ions (in green color) are for Ni atoms, and the last ions (in red color) are for O atoms.

# of ion	s	p	d	tot
1	-0.008	-0.014	1.23	1.208
2	0.008	0.014	-1.23	-1.208
3	0.000	0.000	0.000	0.000
4	0.000	0.000	0.000	0.000
tot	0.000	0.000	0.001	0.000

Normally, the trial magnetic moment value was $2 \mu_B$ for Ni atom and $0 \mu_B$ for O, the calculated value is $1.208 \mu_B$ for Ni, and $0.00 \mu_B$ for O atom (see Table 6.2), but the magnetic moment is correctly described by GGA+U method. The result also shows that the total magnetization is zero, this is in agreement of the fact that both DOS and BS are symmetric with respect to the Fermi energy ($E_F = 0$ eV). For each Ni atom, most of the magnetization comes from the d-orbital electrons, and a small contribution comes from s-orbitals, and the possible reason is s-orbitals are fully occupied, and d-orbitals are not, and yet their electrons have non-zero orbital angular momenta.

Since GGA also underestimates the band gap, the U-approach was used to obtain better accuracy. The chosen U value was 4 eV for d-orbitals of Ni atoms and 0 eV for O atoms, and the exchange interaction value was zero. Like the GGA, the U-approach yielded a zero magnetization and symmetric bandstructure for spin-up and spin-down states, and the energy gap became 2.6 eV. Figure.5.2 shows the symmetric density of

states for spin-up and spin-down states. The Fermi energy level is, at the origin of the energy spectrum, at the valence band maximum.

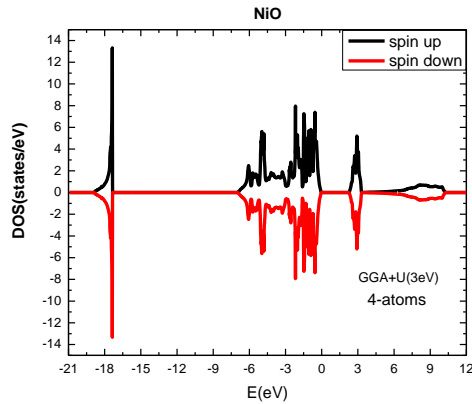


Figure 5.2 Density of states (DOS) for a 4-atom NiO with GGA+U. With $U-J = 3\text{eV}$, the band gap is about 2.6 eV.

As expected, the magnetic moment for Ni atoms was improved by the U-method. The magnetization value with GGA+U(3eV) is about $1.6 \mu_B$. Table 5.2 shows the magnetization for NiO from GGA+U(3eV) calculations. The total magnetization for same orbitals is zero, which means that the total magnetization for the whole system is also zero; thus confirming that the bulk NiO is an antiferromagnetic. As in the previous case with GGA method, the majority of the magnetization comes from the d-orbital electrons and s-orbitals contribute less to the magnetization.

Table 5.2 Calculated magnetic moment (in μ_B) for atomic orbitals and the net magnetic moment for 4-atom NiO using GGA+U(3eV). The first two ions (in green color) are for Ni atoms, and the last two ions (in red color) are for O atoms.

# of ion	s	p	d	tot
1	-0.007	-0.011	1.584	1.565
2	0.007	0.011	-1.584	-1.565
3	0.000	0.000	0.000	0.000
4	0.000	0.000	0.000	0.000
tot	0.000	0.000	0.000	0.000

With the Hubbard correction U for Ni d-orbitals, both bandstructure and density of states for spin up are identical to those for spin down; this indicates that the total magnetic moment, thus the system is antiferromagnetic. With the Hubbard energy $U = 4.0$ eV, there is a band gap of 2.5 eV (See Figure 5.3). With the Hubbard energy $U = 4.5$ eV, the band gap is 3 eV (See Figure 5.4), this is in a much better agreement with the experimental value ranging from 3.5 to 4.0 eV. This also indicates that the value of the band gap depends of the value of U . Normally, other calculations, which are not included here, showed that there is a range for U that leads to the bandgap, in other words, by increasing the value of U , the bandgap increases to reach a maximum and decreases to ultimately vanish.

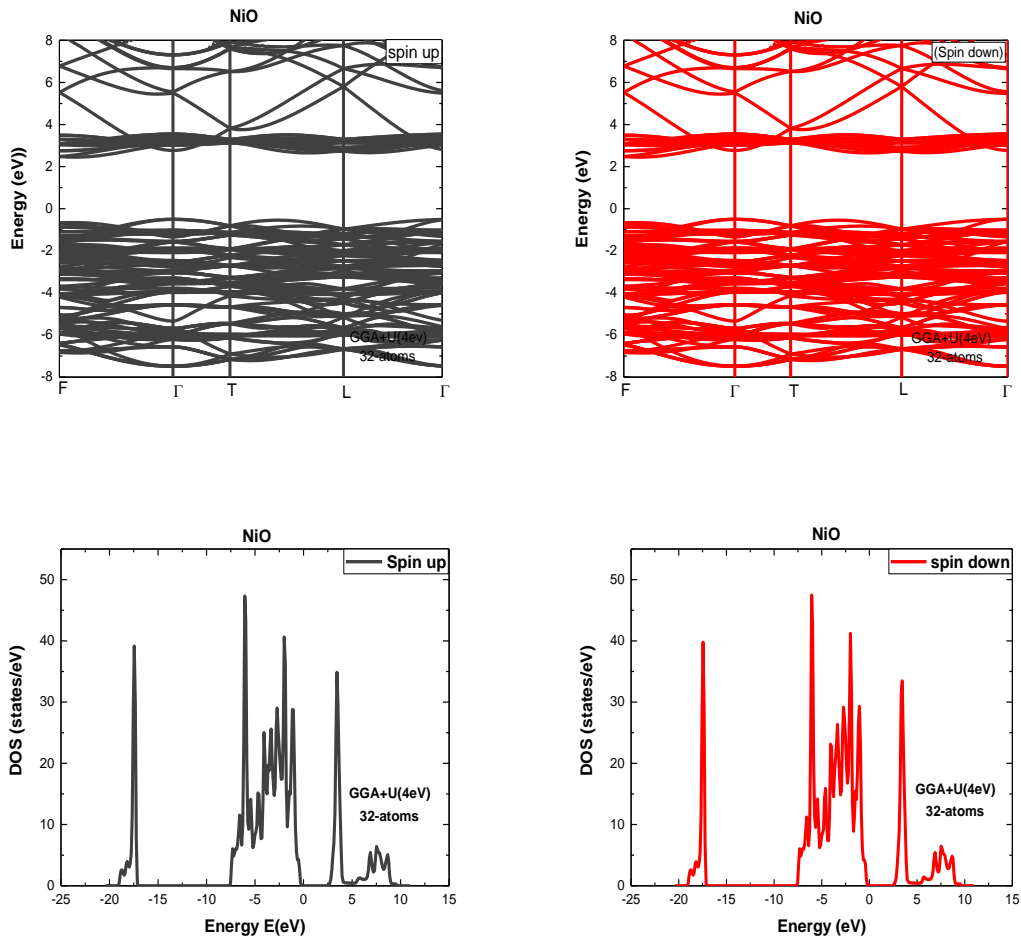


Figure 5.3 Bandstructure (BS) and Density of States (DOS) for a 32-atom NiO Supercell with GGA+U. Spin-up and spin-down states for both BS and DOS are symmetric. With $U-J = 4.0\text{eV}$, the band gap is 2.5 eV.

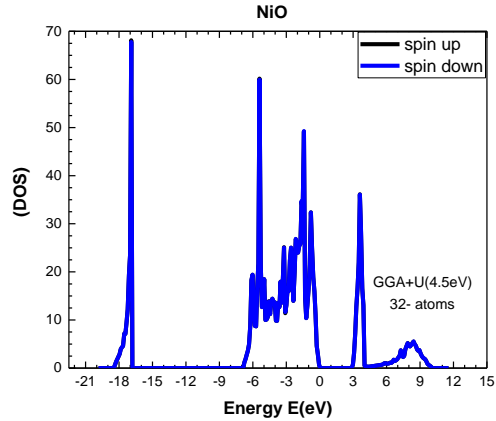


Figure 5.4 Density of states (DOS) for a 32-atom Supercell NiO with the U-approach. Spin-up and spin-down states for DOS are symmetric. With $U-J = 4.5$ eV, the band gap is 3 eV.

The result about the optical properties of NiO from 0 to 10 eV (see Figure 5.5) shows that, at the lowest energy (0.0 eV), the refractive index (n) is about 2.2, and the reflectivity is about 0.14, but the extinction coefficient (k), the real optical conductivity, the absorption, and the energy loss are all null, whereas the reflectivity function is not. The optical conductivity, the absorption and the loss functions begins to increase at around 2 eV. The result also shows that the imaginary dielectric function, the extinction coefficient (k), the reflectivity, the real optical conductivity, and the absorption function have a peak at same energy of the order of 4 eV. For low energies ranging from 0 to approximately 2eV intrinsic NiO is less absorbing, less optically conducting and less lossy.

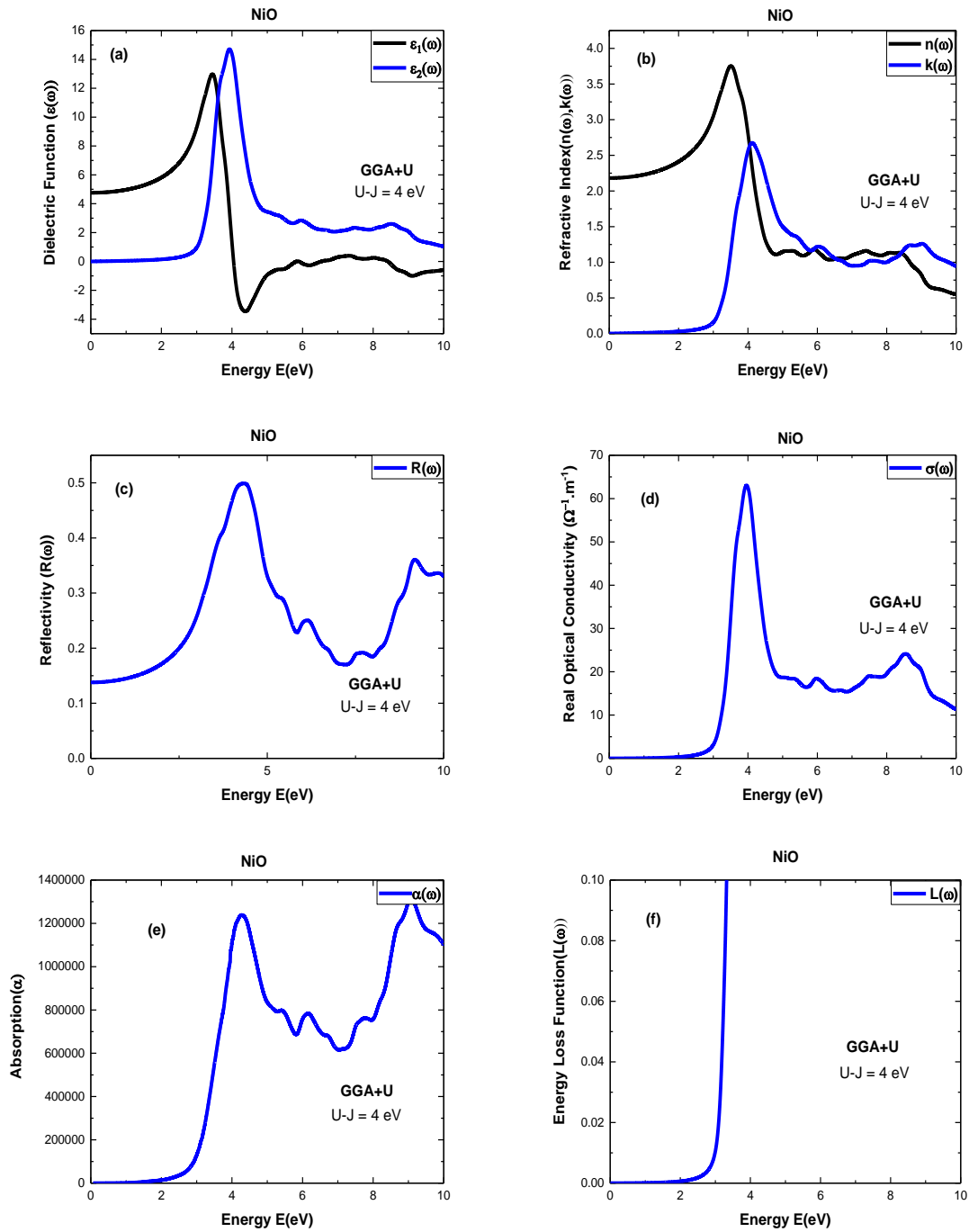


Figure 5.5 Calculated optical properties of NiO using GGA+U method. Dielectric Function (a), Refractive Index (b), Reflectivity (c), Real Optical Conductivity (d), Absorption (e), and Energy Loss (f).

The total magnetic moment is zero as expected ,and the magnetic moment for Ni is $1.643 \mu_B$, this is lightly different from the Ni magnetic moment value in the 4-atom NiO system. Normally, the crystal relaxation was not performed for the 4-atom NiO system because it appeared fully relaxed. But, the magnetic moment of O is zero as expected. Each orbital of O has a zero magnetic moment, thus the most of the magnetic moment originates from the d- orbital electrons for Ni.

Table 5.3 Calculated magnetic moment for 32-atom NiO using GGA+U. The first sixteen ions (in green color) are for Ni atoms, and the last sixteen ions (in red color) are for O atoms.

# of ion	s	p	d	tot
1	-0.005	-0.009	1.657	1.643
2	-0.005	-0.009	1.657	1.643
3	-0.005	-0.009	1.657	1.643
4	-0.005	-0.009	1.657	1.643
5	-0.005	-0.009	1.657	1.643
6	-0.005	-0.009	1.657	1.643
7	-0.005	-0.009	1.657	1.643
8	-0.005	-0.009	1.657	1.643
9	0.005	0.009	-1.657	-1.643
10	0.005	0.009	-1.657	-1.643
11	0.005	0.009	-1.657	-1.643
12	0.005	0.009	-1.657	-1.643
13	0.005	0.009	-1.657	-1.643
14	0.005	0.009	-1.657	-1.643
15	0.005	0.009	-1.657	-1.643
16	0.005	0.009	-1.657	-1.643
17	0.000	0.000	0.000	0.000
18	0.000	0.000	0.000	0.000
19	0.000	0.000	0.000	0.000
20	0.000	0.000	0.000	0.000
21	0.000	0.000	0.000	0.000
22	0.000	0.000	0.000	0.000
23	0.000	0.000	0.000	0.000
24	0.000	0.000	0.000	0.000
25	0.000	0.000	0.000	0.000
26	0.000	0.000	0.000	0.000
27	0.000	0.000	0.000	0.000
28	0.000	0.000	0.000	0.000
29	0.000	0.000	0.000	0.000
30	0.000	0.000	0.000	0.000
31	0.000	0.000	0.000	0.000
32	0.000	0.000	0.000	0.000
tot	0.000	0.000	0.000	0.000

5.2 Optical and Magnetic Properties of Fe-doped NiO

Unlike for NiO, due to the Fe doping the (BS) as well as the (DOS) for spin-up and spin-down states for Fe-doped NiO are noticeably different, consequently, the net magnetic moment should not be zero. In comparison with the DOS for NiO, one realizes the Fe-doping introduces a state that reduces the initial band gap. This state originates from the Fe energy splitting which sends the state t_{2g} of Fe above the highest occupied NiO level, and this t_{2g} sub-band becomes highest fully occupied state (see Figure 5.6), that is why the band gap of Fe-doped NiO is lower than that of NiO. The U-method for Fe-doped NiO yielded the energy gap which is approximately equal to 2.0 eV which is about 0.5 eV lower than the one obtained for NiO (see Figure 5.3 and Figure 5.6).

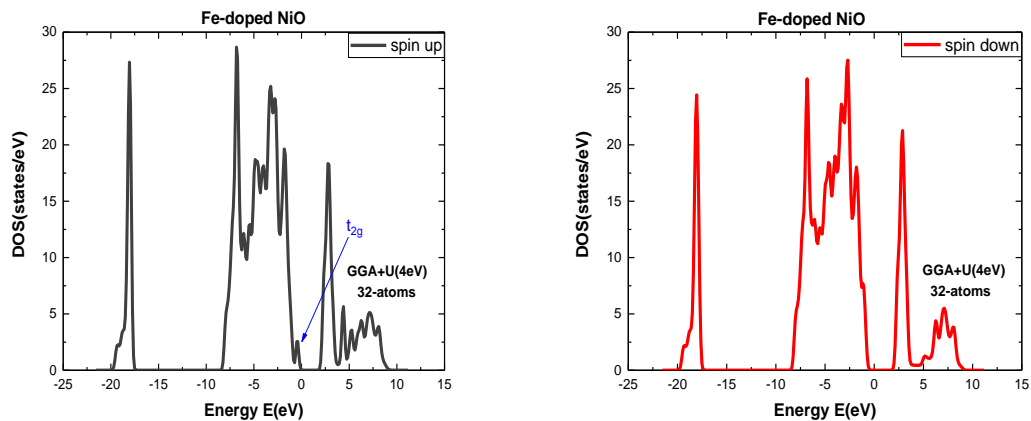


Figure 5.6 Density of States (DOS) for spin-up and spin-down states obtained for a 32-atom Fe-doped NiO supercell using GGA+U. With respect to the Fermi level ($E_F = 0$), the bandgap is about 2 eV.

We also study the optical properties of Fe-doped NiO from 0 to 10 eV. Like the 32-atom NiO system, Fe-doped NiO is less optically conductive, less absorbing, and has less energy loss at lower energies (see Figure 5.7). However, the decrease of the bandgap due to the Fe doping affects the optical properties of intrinsic NiO. For example, the bandgap reduction causes the decrease of the maxima of the dielectric function, the refractive index, the reflectivity, the real optical conductivity, and the absorption function (see Figure 5.5 and Figure 5.7). In addition, the decrease of the bandgap increases the static refractive index (n) from 2.2 to 2.25, also there is an increase of static reflectivity $R(0)$ from about 0.14 to 0.15 (see Figure 5.5 and Figure 5.7). For lower energies, the real optical conductivity, and the absorption function begin to increase at approximately 2eV as in intrinsic NiO, but the loss function of Fe-doped NiO increases faster than that of intrinsic NiO, this is also due to the reduced band gap in Fe-doped NiO compared to intrinsic NiO (see Figure 5.5 and Figure 5.7).

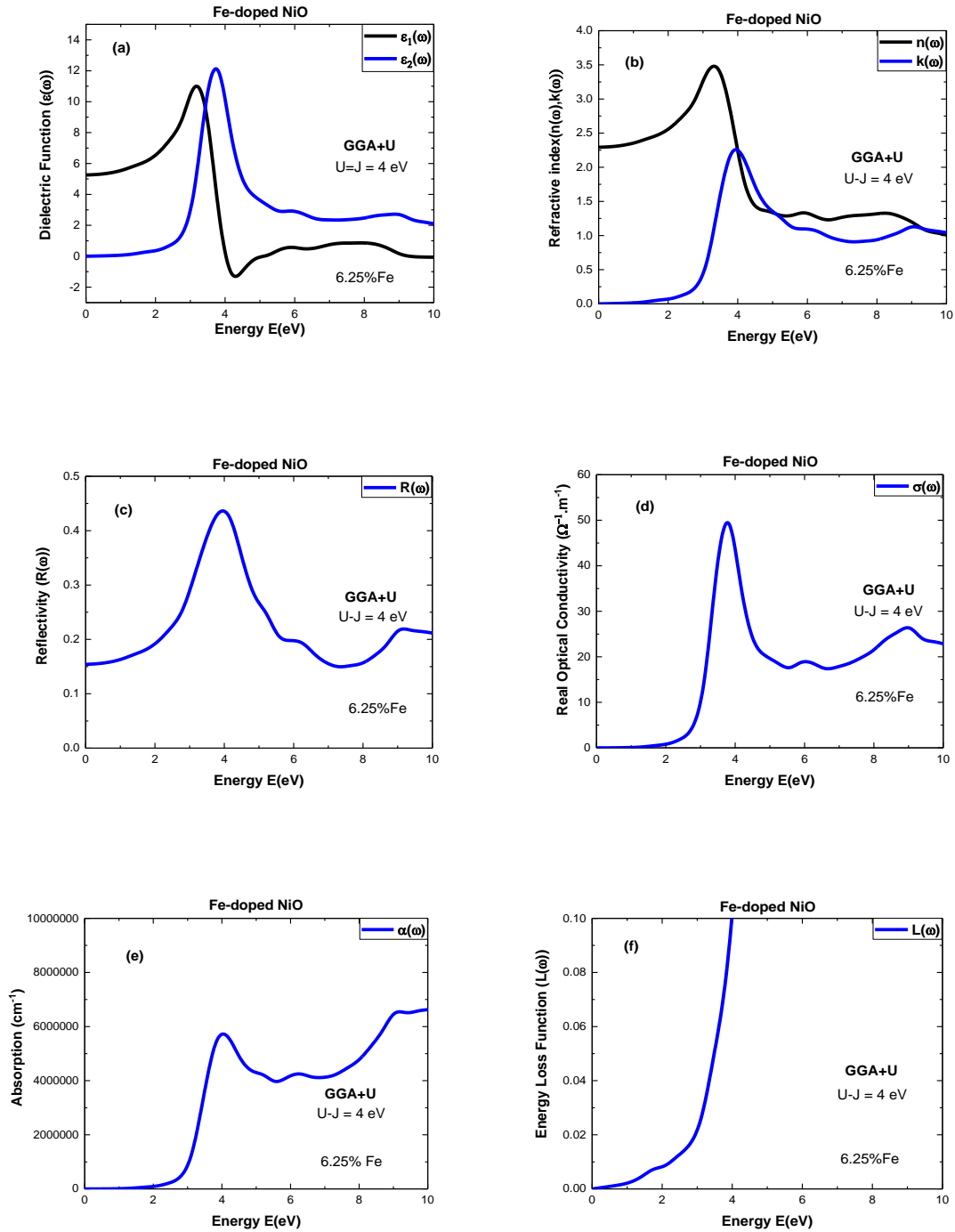


Figure 5.7 Calculated optical properties of Fe-doped NiO using GGA+U (4eV) method. Dielectric Function (a), Refractive Index (b), Reflectivity (c), Real Optical Conductivity (d), Absorption (e), and Energy Loss (f).

Unlike for NiO, the result (see Table 5.4) from the calculations shows that 6.25 at.% Fe-doped NiO has a non-zero magnetic moment of the order of $1.968 \mu_B$, this is obvious since Fe atom has a higher magnetic moment than Ni atom, for example, according to Hund's rule. The calculated magnetic moment of Fe is $3.652 \mu_B$, and the magnetic moments for Ni and O are approximately identical to those obtained for NiO. Like for NiO, for each Ni atom in the Fe-doped NiO, the major contribution to the magnetic moment comes from d-orbitals, and even though the overall magnetization for each O atom is zero, p-orbitals of each O contributes more to the magnetic moment.

Table 5.4 The calculated magnetic moment (in μ_B) for 32-atom 6.25 at. % Fe-doped NiO using GGA+U (4 eV). The first ion (in aqua color) is for Fe atom, the following fifteen ions (in green color) are for Ni atoms, and the last sixteen ions (in red color) are for O atoms.

# of ion	s	p	d	tot
1	0.012	0.008	3.632	3.652
2	0.003	0.002	1.671	1.677
3	-0.007	-0.011	1.635	1.618
4	-0.005	-0.01	1.643	1.628
5	-0.007	-0.011	1.635	1.618
6	-0.005	-0.01	1.64	1.625
7	-0.003	-0.003	-1.67	-1.675
8	-0.006	-0.011	1.633	1.616
9	0.006	0.008	-1.638	-1.623
10	-0.003	-0.003	-1.67	-1.675
11	0.007	0.01	-1.633	-1.616
12	0.006	0.009	-1.635	-1.62
13	0.007	0.01	-1.632	-1.615
14	0.006	0.009	-1.636	-1.621
15	0.004	0.002	1.672	1.678
16	0.007	0.009	-1.635	-1.619
17	0.000	-0.001	0.000	-0.001
18	0.000	-0.009	0.000	-0.009
19	0.000	-0.013	0.000	-0.013
20	0.000	0.002	0.000	0.002
21	0.000	-0.02	0.000	-0.019
22	0.000	0.000	0.000	0.000
23	0.000	0.000	0.000	0.000
24	0.000	0.001	0.000	0.001
25	-0.007	-0.061	0.000	-0.068
26	0.000	0.000	0.000	-0.001
27	0.007	0.063	0.000	0.07
28	-0.007	-0.082	0.000	-0.089
29	0.007	0.064	0.000	0.072
30	-0.007	-0.076	0.000	-0.083
31	0.001	-0.009	0.000	-0.008
32	0.007	0.062	0.000	0.069
tot	0.023	-0.066	2.012	1.968

Table 5.5 Calculated magnetic moment (in μ_B) for 32-atom 12.5 at. % Fe-doped NiO using GGA+U (4 eV). The first ion (in aqua color) is for Fe atom, the following fifteen ions (in green color) are for Ni atoms, the nineteenth ion (in aqua color) is for Fe atom, and the last fifteen ions (in red color) are for O atoms.

# of ion	s	p	d	tot
1	0.014	0.011	3.797	3.822
2	-0.002	-0.007	1.723	1.714
3	-0.002	-0.007	1.723	1.714
4	-0.001	-0.007	1.718	1.709
5	-0.002	-0.007	1.723	1.714
6	-0.001	-0.007	1.718	1.709
7	-0.002	-0.007	1.72	1.711
8	-0.001	-0.006	1.722	1.715
9	-0.014	-0.011	-3.764	-3.789
10	0.002	0.007	-1.723	-1.714
11	0.002	0.007	-1.723	-1.714
12	0.001	0.007	-1.718	-1.709
13	0.002	0.007	-1.723	-1.714
14	0.001	0.007	-1.717	-1.709
15	0.002	0.007	-1.719	-1.711
16	0.001	0.006	-1.722	-1.715
17	0	0	0	0
18	0	0	0	0
19	0	0	0	0
20	0	0	0	0
21	0	0	0	0
22	0	0	0	0
23	0	0	0	0
24	0	0	0	0
25	0	0.002	0	0.002
26	0	0.007	0	0.007
27	0	0.006	0	0.006
28	0	-0.006	0	-0.006
29	0	0.006	0	0.006
30	0	-0.006	0	-0.006
31	0	-0.007	0	-0.007
32	0	-0.002	0	-0.002
tot	0	0.002	0.034	0.036

5.3 Summary

GGA/GGA+U calculations show that NiO is an antiferromagnetic semiconductor. With the GGA method, a 4-atom NiO has a band gap of 0.6 eV, and with the GGA+U method, a 32-atom NiO has a band gap of 2.5 eV by using U(4eV), and a band gap of 3 eV by using U(4.5eV). The calculated magnetic moments of Ni and O atoms are $\sim 1.7 \mu_B$, and $0 \mu_B$ respectively, this is in agreement with [84]. GGA+U calculations show that 6.25 at.% Fe-doped NiO has a non-zero net magnetic moment. The calculated magnetic moments for Ni and O are, on average, similar to those obtained for NiO. The calculated magnetic moment for Fe is $\sim 3.7 \mu_B$, and this value is in agreement with [84]. This explains why 6.25 at. % Fe-doped NiO has a non-zero net magnetic moment since only one Ni atom was substituted by one Fe atom keeping the same antiferromagnetic ordering. The result also shows that 12.5 at.% Fe-doped NiO have a very small net magnetic moment to be considered zero (note that there is also a magnetic contribution from O atoms), thus 12.5 at.% Fe-doped NiO. This indicates that the magnetic nature of Fe-doped NiO depends on the Fe concentration. The Fe doping decreases the bandgap, and this decrease affects the optical properties of NiO. The decrease of bandgap increases the static refractive index (n) just as P. Mallick et al.[104] claim that the reduction of the bandgap due to the Fe doping increases the refractive index.

V.LAB INSTRUMENTS AND RESULTS

6.1 AJA Magnetron Sputtering System

The AJA Magnetron Sputtering System is a confocal thin-film deposition instrument which is usually utilized to deposit thin-films of metals and insulators on silicon wafers or other substrates. The system contains 2 DC and 2 RF magnetron sputtering guns which allow in-situ tilting of their heads; this allows uniformity, or sputtering rate optimization at any distance within a short period of time and a minimal effort. The system uses a LabVIEW based Phase II-J computer control system allowing both manual and automated modes [85].



Figure 6.1 AJA Sputtering System in the Cleanroom at Texas State University.

The system can attain a pressure as low as $4E-8$ Torr, and the substrate holder allows simultaneous rotation, and heating up to 850 degrees Celsius. During the

sputtering process, Argon ions are accelerated into the target consisting of the material to be deposited, and due to the energy and momentum transfer, some of the target atoms are ejected. These ejected atoms form an atom beam and are deposited on the substrate. The ignition of the plasma requires a pressure above 20 mTorr, and the initial presence of positively charged ions necessary to start a plasma may depend on cosmic radiation. In the Direct Current (DC) sputtering mode, positively charged ions are accelerated to the target by a negative potential of hundreds of volts. Electrons created by impacting ions can also cause further ionization of the gas. However this technique is limited to conducting materials such as metals and doped semiconductors. The main reason is that impacting positively charged ions would create a charge on an insulating target, and annihilate the ion current. To prevent the charge build up, a Radio-Frequency (RF) alternating current (AC) voltage is applied to insulating targets, thus this technique is called RF-sputtering. The samples reported on in this thesis were made by reactive RF magnetron sputtering using a mixture of oxygen and argon.

6.1.1 Sample Manufacturing

Samples were sputtered in the AJA Sputtering system. As the deposition rate was not constant but varied across the sample-holder, and to reduce the thickness variations across the substrate the sample holder was rotated at 40 rpm during deposition. The thickness varies slightly across a 3'' microscopic slide. Si/SiO₂ was used as substrates for all samples. All substrates were cleaned [86] via sonication in water for five minutes, acetone for five minutes, methanol for five minutes, and isopropyl alcohol (IPA) for five minutes.

After the substrates were loaded into the AJA sputtering system the substrates were cleaned in-situ using the Copra gun: 240 Watts, 0.15 sccm argon (Ar) flow, and a cleaning time of 300 seconds. The films were sputtered at room temperatures using a metallic target of Ni or Ni_{0.8}Fe_{0.2}. For all cases the substrate shutter was used during the time the guns were ramped up to full power and the gas flow rates were adjusted. The deposition power was 240 Watts for all samples. The other deposition parameters are summarized in Table 6.1 below. The deposition rate was measured with a crystal thickness monitor. To avoid the sputter guns from getting overheated, after sputtering for 600-700 seconds the gun was switched off and allowed to cool down for 10 minutes. After the cool down period, the guns were started up again and the deposition was continued. The number of sputter sessions are listed in the table and labeled as #runs. The total gas flow was kept constant during deposition at 50-51 sccm. Films were sputtered at two different oxygen (O) sputter gas concentrations. Table 6.1 shows two different sputter pressures. PM was measured with a capacitance manometer and PT was measured with a convectron gauge. The readings of the latter vacuum gauge depend on the type of gas. The AJA convectron gauge is calibrated for N₂. The real pressure for Ar is a factor 1.4 larger than the indicated value. The values listed in the table are the values read from the instrument.

Table 6.1 Deposition Parameters for NiO and NiFeO Samples.

sample	target	Ar flow sccm	O flow sccm	volt	#runs	Dep. Rate [A/sec]	Depos. Time [sec]	PM [mTor]	PT [mTor]
081016A/B	Ni81Fe19	45.02	5	119	7	0.5	4560	7.7	3.9
081016-1/2	Ni81Fe19	49.74	0.54	107	5	0.7	3300	7.9	N/A
081416-A/B	Ni	45.03	6.02	137	7	0.6	4260	7.9	4
081516-1/2	Ni	50.23	0.47	127	6	0.9	3600	8.9	3.8

As already mentioned, samples were made by reactive RF magnetron sputtering; the background pressure in the chamber before starting the deposition was in the 10^{-8} Torr range. Prior to deposition the Ni or NiFe target was pre-sputtered for one minute, sputtering was done using a mixture of Ar and O gases. Note that two Si/SiO₂ substrates were mounted for the same sputtering run resulting in two samples for each deposition run.

Dependent on the chemical composition, and the oxygen flow during deposition, four types of samples were made:

Table 6.2 Composition and Dimensions of NiO and NiFeO samples. (High O) and (Low O) stand for high and low oxygen flow respectively.

Sample	Composition	Width	Length	Thickness	Volume (m ³)
081416A	NiO (High O)	4.6 mm	4.375 mm	335.4 nm	6.752e-12
081516-1	NiO (Low O)	4.2 mm	5.650 mm	437.0 nm	10.99e-12
081016A	Ni _{0.8} Fe _{0.2} O _{1.δ} (High O)	4.2 mm	4.400 mm	269.5 nm	4.985e-12
081016-2	Ni _{0.8} Fe _{0.2} O _{1.δ} (Low O)	4.0 mm	5.500 mm	293.5 nm	6.457e-12

Two different techniques were used to determine the thickness of the samples: prior to deposition the deposition rate was measured with a crystal thickness monitor and

the film thickness was calculated from the measured deposition rate and deposition time. Also ellipsometry was used to determine the film thickness. Both techniques did not yield the same results. Table 6.3 shows the estimated thickness from the thickness monitor deposition rate and deposition time as well as the measured thickness determined from ellipsometry measurements. The ellipsometry thickness is consistently higher. A plot of the crystal monitor thickness vs. the ellipsometer thickness shows a straight line with a slope of 0.75 and a non-zero y-axis intersect.

Table 6.3 Samples thickness measured with different techniques: Ellipsometer, and Crystal Monitor.

Sample	Composition	Est. thickness (Ellipsometry just after deposition)	Est. thickness (crystal monitor)	Est. thickness (Ellipsometry with roughness, 6 months after deposition)
081016A/B	Ni _{0.8} Fe _{0.2} O(High O)	269.5 (nm)	228 (nm)	261.6+6.8 (nm)
081016-1/2	Ni _{0.8} Fe _{0.2} O(Low O)	293.5 (nm)	231 (nm)	283.3+30.7(nm)
081416-A/B	NiO(High O)	335.4 (nm)	256 (nm)	316+17 (nm)
081516-1/2	NiO(Low O)	463.5 (nm)	324 (nm)	436.5+30.6(nm)

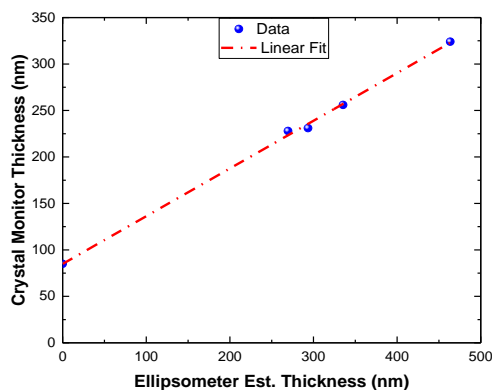


Figure 6.2 Crystal Monitor Thickness (nm) vs Ellipsometer Est. Thickness (nm) just after deposition.

The crystal monitor thickness is based on mass (using density). The optical thickness is based on actual thickness (using the wavelength of the light). The difference could indicate that the RF sputtered NiO and NiFeO thin films have a different density than bulk material, possibly due to voids caused by the high sputter pressures (50 mTorr). The ellipsometric values in this table are based on the ellipsometric measurements that we did immediately after we made the samples. Another explanation could be a systematic error in the ellipsometer thickness caused by an initial seed layer with different optical properties as revealed by [87]. The optical properties that vary through the film thickness are not uncommon for oxide materials. For example, the dry or wet oxide on Si is normally modeled by a bi-layer with two different refraction indices.

6.2 X-ray Diffractometer (XRD)

The reason why the X-ray diffraction is commonly utilized for the study of crystal structure and atomic spacing is crystals act as diffraction gratings for X-ray wavelengths. The X-ray diffraction is based on constructive interference which is produced when the interaction of the X-rays and the crystal satisfy the Bragg's Law which relates the wavelength of the X-rays to the lattice spacing. A scan of the sample through a range of 2θ angles allows reaching all possible diffraction directions of the crystal lattice. And since a material has a unique d-spacing, a relation between the diffraction peaks and the d-spacing allows for the identification of the crystal structure and orientation.

The X-Ray Diffraction (XRD) system consists of three basic parts: an X-ray tube, a sample holder, and an X-ray detector. In the X-ray tube, electrons from the heated cathode are accelerated by the anode. Upon their arrival at the anode, their interaction with the atoms of the anode leads to the release of energy and the emission of the X-ray spectra when incoming electrons have sufficient energy to displace the inner shell electrons of the target material. The X-ray spectra have a variety of components, and the strongest are K_α and K_β lines due to respective electronic transitions from L shells to K shells, and M shells to K shells. The K_α component of the X-ray spectra consists of two parts of almost the same intensity and energy: $K_{\alpha 1}$, and $K_{\alpha 2}$ [88]. The X-rays are collected from the source by a collimator, and directed towards the sample. The reflected X-rays are detected by a detector that is mounted on a goniometer and the intensity of the beam is recorded. As mentioned before, peak intensity occurs once the Bragg's Law is

satisfied. Then the detector processes the X-ray signal and sends the output signal to a computer system.

6.2.1 System Preparation and Measurement Methods

Measurements were made using a SmartLab Rigaku Diffractometer. The instrument is easy to use since it is a fully computer controlled system with guidance software. Before any of the measurements, the water chiller is turned on. A wait time might be required for the chiller's temperature to reach 70F. Normally, this is the recommended temperature at which the XRD system is ready for operation. Next, the connected computers to the XRD system are powered up and the HyPix detector is connected. The smartlab guidance software is started and the X-ray generator is activated. For measurement, the voltage and the current are set to 40kV and 44mA respectively [89], [90]. The type of the measurement is chosen and both optical and sample alignments are performed. For optical alignment, the system starts with the alignment of the source components, and moves down the light path. For the sample alignment, the system aligns the sample parallel with the light path. Center slit and Height Reference Sample Plate are usually required for optical alignment, and changing between samples may require optical alignment for best measurement results.

6.2.2 XRD Measurements

Prior to measurement, the samples were cleaned with ionized water, acetone, methanol, and isopropyl, and then dried with IPA using the spinner. Figure 6.3 shows the Rigaku X-ray Diffractometer (XRD) which was used for the measurements. After the system preparation, for each measurement, the glass was placed between the sample and

the sample stage to reduce the background noise. The sample stage was installed in the system in parallel beam (PB) configuration for a theta/2theta scan [90] starting from 30 to 100 degrees. The typical duration for each measurement was set to 8 min.



Figure 6.3 Rigaku X-Ray Diffractometer (XRD) at Texas State University.

The θ angle was set at 2 degrees and only the sample scan was done through the 2θ angle. So this X-ray scan does not show the planes parallel to the substrates as the traditional 2θ - scan. In fact, the peaks at low angle originate from planes that are kind of parallel to the substrate while the peaks at higher two theta angle are caused by planes that make an angle with the substrate. By choosing a small θ angle, the incident X-rays are more or less parallel to the substrate and do not see the silicon substrate. So the Si

peaks are strongly suppressed. The peak combination around 54 degrees in the spectra is caused by the Si substrate. If necessary, it can also be removed by rotating the sample slightly around its normal. The X-ray measurements were done with a slit width of 5 mm. The plastic clips to hold the samples were not used. The smaller slit width (i.e. 5 mm instead of 10 mm) guaranteed that none of the x-rays is missing the sample and hit the substrate holder or the clips.

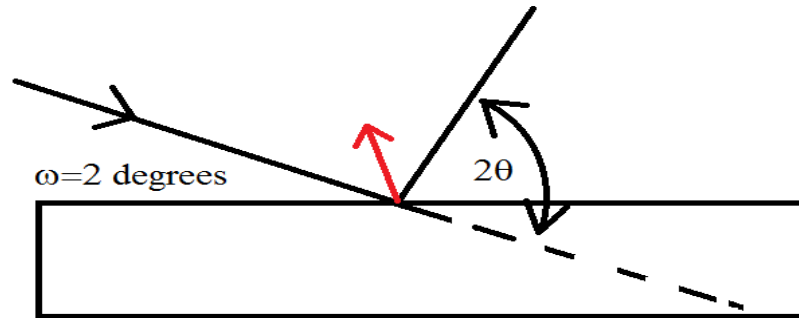


Figure 6.4 An example of the propagation of light for a theta (2 degrees)/ 2theta scan with XRD.

6.2.3 X-Ray Results for NiO and Ni_{0.8}Fe_{0.2}O_{1-δ} Samples

XRD shows that some of the NiFeO peaks are much weaker and slightly broader than those of NiO; this indicates that both samples have the same crystal structure, but NiFeO samples have smaller crystallites and possibly a different texture. Due to the

omega measurement configuration, the (111) peak and the (222) peak originate from the same crystal direction but different crystallites. Similarly, the (200) peak and the (400) peak originate from the same crystal orientation but different crystallites. These diffraction peaks are characteristic of the NaCl-type structure, thus our XRD are in agreement with [36], [38].

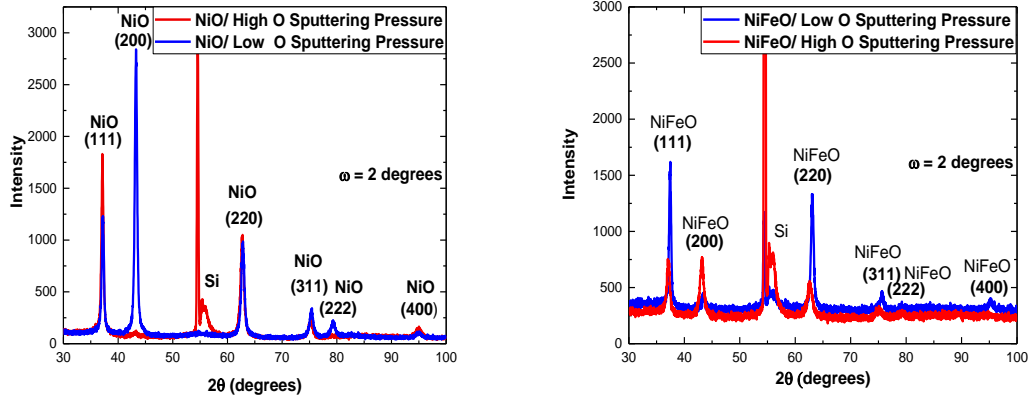


Figure 6.5 XRD for NiO, and Ni_{0.8}Fe_{0.2}O_{1-δ} samples. Both results show that samples have NaCl-type structure.

It should be noted here that although XRD results are often used to show the absence of other phases, 2θ scans are very not sensitive to nanoparticles of other phases. As the diffraction peak width increases with smaller size grains, the peaks of nanoparticles often disappear in the noise of the 2θ scan. Nanoparticles of these phases can still be present as shown by A P. Douvalis et al. [35]. FTIR ellipsometry measurements on RF sputtered FeNiO by Taludker et al. confirm the rocksalt crystal structure [105].

6.3 Ellipsometry

Ellipsometry is a powerful technique for research on new materials and processes. This technique was utilized to determine the optical properties of all samples. The theory of Ellipsometry is based on Fresnel reflection and transmission equations of polarized light on the planar interfaces of a multilayer material. The term Ellipsometry comes from the fact that the reflected light of incident linearly polarized light arriving on a surface at an oblique angle is often elliptically polarized. The change of the state of polarization of the light upon reflection depends on the optical properties and structure of the multilayer. Since the light wave is transverse, the end point of the electric field describes an elliptical trajectory in a plane perpendicular to the wave number vector \vec{k} [91]. Perpendicular to \vec{k} are mutual electric field \vec{E} and magnetic field \vec{B} vectors. Figure 6.6 shows the propagation of light from the source to the sample to the detector. The simplest relation between the electric field \vec{E} , and the magnetic field \vec{B} is given by the following formula:

$$\vec{B} = (\vec{k} \times \vec{E}) / \omega \quad (6.1)$$

Here \vec{k} is the wave number, and ω is the angular frequency.

The electric field \vec{E} can be described by the superposition of two linearly polarized electric plane waves of complex amplitudes E_p , and E_s which are respectively parallel and perpendicular to the plane of incidence containing the wave number vector \vec{k} , and the normal to the sample. These two wave components are usually called p-waves

and s-waves respectively. Their corresponding planes are shown in Figure 6.6. The time dependence of the electric field \vec{E} can be expressed as follows [91]:

$$\vec{E}(t) = \begin{bmatrix} E_s(t) \\ E_p(t) \end{bmatrix} = \text{Re} \left\{ \begin{bmatrix} E_{os} e^{i\Delta} \\ E_{op} \end{bmatrix} \exp[i\omega(t - t_0)] \right\} \quad (6.2)$$

Here t_0 is the initial time, and Δ is the ellipsometric relative phase which measures the difference in phase shift of the p- and s- light waves upon reflection. E_{os} / E_{op} , the relative amplitude of the electric field amplitudes E_{os} and E_{op} is often written as $\tan(\Psi) = E_{os} / E_{op}$. Both Ψ and Δ are determined by single ellipsometric measurement. The ratio of the intensity of the outgoing wave to that of the incident wave is called the reflectance (\mathfrak{R}). Note that intensities are proportional to the square of the electric field amplitudes.

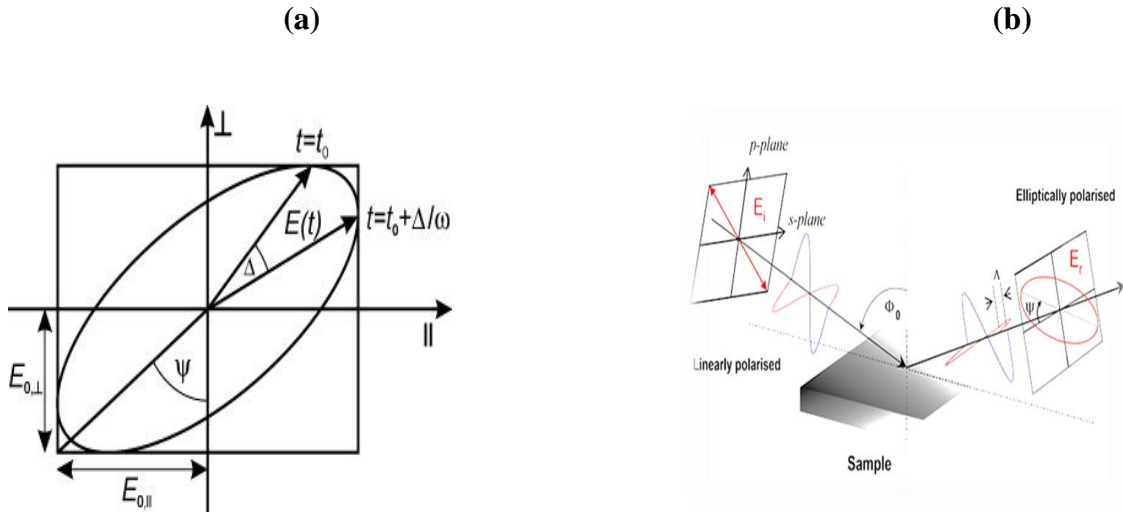


Figure 6.6 (a) Elliptically polarized light wave as described by Eq. (6.2). (b) Illustrates the propagation and polarization of light. Linearly polarized light is elliptically polarized upon reflection with the sample.

The reflection or transmission of an EM-wave with a planar interface is described by the Fresnel equations. For a planar interface between medium 1 and medium 2 with refraction indices \hat{N}_1 and \hat{N}_2 respectively, the Fresnel coefficients for reflection (a) and transmission (b) are given by [93]:

$$r_{12}^p = \frac{\hat{N}_2 \cos(\phi_1) - \hat{N}_1 \cos(\phi_2)}{\hat{N}_2 \cos(\phi_1) + \hat{N}_1 \cos(\phi_2)} \quad r_{12}^s = \frac{\hat{N}_1 \cos(\phi_1) - \hat{N}_2 \cos(\phi_2)}{\hat{N}_1 \cos(\phi_1) + \hat{N}_2 \cos(\phi_2)} \quad (6.3a)$$

$$t_{12}^p = \frac{2\hat{N}_1 \cos(\phi_1)}{\hat{N}_2 \cos(\phi_1) + \hat{N}_1 \cos(\phi_2)} \quad t_{12}^s = \frac{2\hat{N}_1 \cos(\phi_1)}{\hat{N}_1 \cos(\phi_1) + \hat{N}_2 \cos(\phi_2)} \quad (6.3b)$$

Here, ϕ_1 refers to the angle of incidence, ϕ_2 to the angle of refraction, the superscripts stand for p-waves and s-waves, and the subscripts stand for the medium 1 and medium 2. For a material with, more than one interfaces, the transmitted light across any interface can end up being reflected, thus the total Fresnel reflection coefficient (R) is defined as the ratio of the outgoing resultant electric field amplitude to the incoming electric field amplitude of light. For instance, for a thin film with two interfaces, the light wave reaching interface 2 can either be transmitted in the medium 3, or reflected back (see Figure 6.7), thus the total reflection coefficient is [93]:

$$R^p = \frac{r_{12}^p + r_{23}^p \exp[-j4\pi(d/\lambda)\tilde{N}_2 \cos(\phi_2)]}{1 + r_{12}^p r_{23}^p \exp[-j4\pi(d/\lambda)\tilde{N}_2 \cos(\phi_2)]} \quad (6.4a)$$

$$R^s = \frac{r_{12}^s + r_{23}^s \exp[-j4\pi(d/\lambda)\tilde{N}_2 \cos(\phi_2)]}{1 + r_{12}^s r_{23}^s \exp[-j4\pi(d/\lambda)\tilde{N}_2 \cos(\phi_2)]} \quad (6.4b)$$

Here d is the thickness of the medium 2, and λ is the wavelength of the light. Thus the relation between R and Ψ is given by the formula, [92], [93] $\tan(\Psi) = |R^p|/|R^s|$, and the reflectance \mathfrak{R} is related to the total reflection coefficient R by the formula $\mathfrak{R} = |R|^2$.

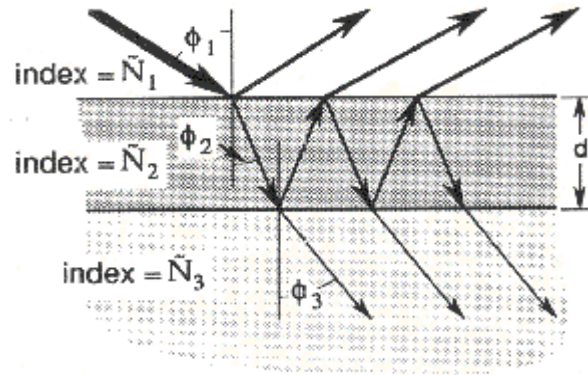


Figure 6.7 Reflection of light from a single thin film. The total reflected light is the sum of waves going back in the medium 1, and the total transmitted light is the sum of light waves reaching the medium 3.

The samples studied in this thesis are more complicated than the one illustrated by the above Figure 6.7 because they contain two thin films, a 2.25 nm thick SiO₂ layer in between the Si wafer and the transition metal oxide film. This oxide layer is thick enough to avoid a reaction between Ni and Si atoms at room temperature.

6.3.1 CompleteEase Software

Results from experimental ellipsometric measurements are analyzed using the CompleteEase program. This computational tool is utilized to determine samples

properties such as energy gap, optical properties, thickness, and surface roughness. The program can interface with the ellipsometer to perform measurements, thus data collection and analysis can be done within the CompleteEase program. The program utilizes different models such as Lorentz model for characterizing optical properties in the infrared part of the electromagnetic spectrum, or Cody-Lorentz model for describing the energy-gap and its effect on the optical properties [94]. Other incorporated models such as Cauchy, Sellmeier, Forouhi, and Urbach tail also play important roles, for instance, the optical properties of transparent materials can be described below the bandgap by Cauchy or Sellmeier models. The latter model describes absorption below the energy gap.

6.3.2 Ellipsometric Measurement Methods and Settings

Measurements for determining the optical properties of samples were made using a Woollam M-2000 ellipsometer which is a rotating compensator ellipsometer. Figure 6.8 shows a Woollam M-2000 ellipsometric model for optical characterization.

The wavelength range was from 350 to 2000 nm, and most measurements were made using: a six angles recipe, a three angles recipe, or a one angle recipe. The integration time was set between 10 and 30 seconds. The typical accuracy for straight-through measurements of this type of ellipsometer is $\Psi = \pm 0.075^\circ$ and $\Delta = \pm 0.05^\circ$ (for a 10-second integration time). And the amount of noise on the ellipsometric quantities was negligible and errors are mostly caused by imperfections in the assumed model.



Figure 6.8 Woollam M-2000 Ellipsometer (Credit J.A Woollam.Co., Inc.).

In addition to ellipsometric measurements, the M-2000 ellipsometer can also be used to measure the transmission spectra of the samples sputtered on glass. The transmission measurements are typically done at perpendicular incidence. The data from the measurements were modeled and analyzed using the CompleteEase Software. Models were made using both optical properties of materials from the Woollam database, and some materials manufactured in the cleanroom at Texas State University. For all films, it was assumed that the optical properties were isotropic and constant through the film thickness. Strictly speaking those assumptions are not correct as grain size increases with

film thickness, resulting in a change of the optical properties through the film thickness as shown by [87]. It is expected that the error caused by deficiencies in the model of the samples has a tremendous effect on the calculated film thickness than the noise in the Ψ and Δ spectra.

6.4 Physical Property Measurement System

The physical property measurement system (PPMS) [95] is an instrument that contains several measurement techniques of physical properties such as resistivity, and magnetic properties [96] under constant or variable temperature, pressure, magnetic and electric fields. Magnetic properties are determined with the vibrating sample magnetometer (VSM) technique [95]. The PPMS has a 9-Tesla superconducting magnet capable of producing a magnetic field ranging from -9 to +9 Tesla [95]. Measurements can be done along a temperature interval ranging from 1.9K to 300K [95]. The maximum sample size depends on the type of measurement technique. For the VSM the maximum sample size is 4x4 mm².

6.4.1 Measurement Procedure and Settings

The measurement of magnetic properties requires following a certain procedure to ensure the safety for both the user and the instrument. The system must be prepared for the VSM installation. To avoid the superconducting magnet from quenching, the Helium level in the system must stay above 70%. For each VSM measurement, using the MultiVu program interfaced with the system, the temperature and the magnetic field was

set to 300 K, and 0 Oe respectively, and then the system was vented. Before loading the sample, any existing sample in the sample chamber was removed. The coil set was inserted in the sample chamber using the puck-insertion tool. The sample tube was carefully lowered in the sample chamber until the centering ring touched the top flange. The linear motor was installed on the top flange, and linear motor and VSM cables are connected to the system. The VSM was activated, and when it was ready, the chamber was opened, and the sample mounted on the sample holder was carefully lowered through the top of the linear motor. After sample loading, the chamber was closed, and purged using the standard purge method. The sample position was set manually. Normally, the sample position can be set either manually or automatically, however, since our samples have very a weak magnetic moment, only the manual setting for sample position was possible. After the measurement, we followed the same procedure in reverse for sample unloading and instrument shutdown.

6.4.2 Measurement of Magnetic Properties for Samples

The magnetic properties for both NiO and Permalloy (NiFe) Oxide with high and low oxygen concentration were determined with the (Model 6000) Quantum Design Physical Property Measurement System (PPMS) [95]. Figure 6.8 shows the PPMS which was utilized for the VSM measurements. Before each measurement, samples were cleaned with ionized water, acetone, methanol, and isopropyl, and then were dried using a spinner. For each measurement, a sample of roughly $4 \times 4 \text{ mm}^2$ was mounted on a Quantum Design quartz sample holder using glue (rubber cement) and substrate tiles were mounted around the sample to make the substrate longer than the distance between the VSM pick-up coils (see Figure 6.10), this techniques suppresses the diamagnetic

signal of SiO₂/Si substrate since the VSM measurement for any sample longer the distance between the pick-up coils is zero.



Figure 6.9 The Quantum Design PPMS-Model 6000 at Texas State University.

The measurement involved the determination of magnetic moment (m) as function of the temperature (T) or function of the applied magnetic field (H). Measurements were taken in the magnetic field (H) after sample cooling to the desired temperature (3K) either without the applied magnetic field to obtain zero-field cooled (ZFC) curves or with the applied magnetic field to obtain field cooled (FC) curves. The temperature was varied from 3K to 300K, and the applied magnetic field varied from -0.3 to 0.3 Tesla and from -9 to 9 Tesla. Two type of sequence of commands were written in the Multivu program: one sequence for the measurement of $m(H)$ from -9 to 9 Tesla at different temperature (T), another sequence for ZFC and FC curves of $m(T)$ at 9 Tesla,

followed by $m(H)$ from -0.3 to 0.3 Tesla after a wait time of 900s, and ZFC and FC curves of $m(T)$ at 0.3 Tesla after a wait time of 300s.

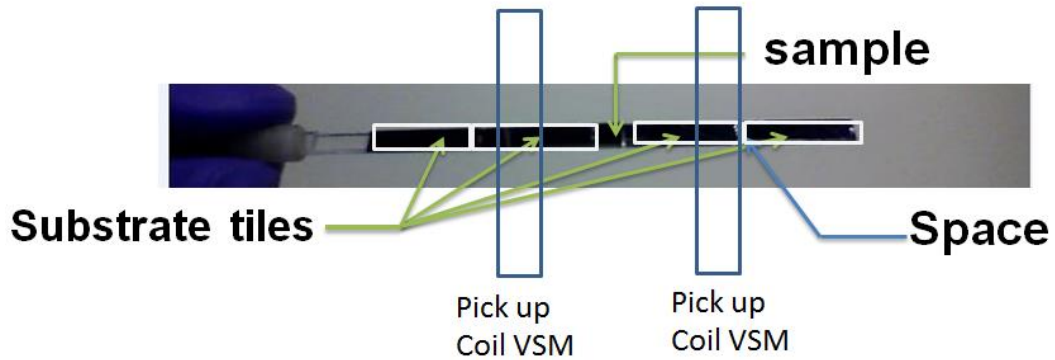


Figure 6.10 The sample holder fully covered by the sample (in the middle) + substrate tiles. The effect if the substrate is suppressed since it is longer than the distance between the pick-up coils.

Each hysteresis curve measurement was done in the sweeping field control mode, and the linear field approach mode with the time constant of 1s. The field speed for $m(H)$ measurements was 11 Oe/s for the 0.3 tesla hysteresis curves and 100 Oe/s for the 9 tesla hysteresis curves. The temperature speed for $m(T)$ measurements was 0.017 to 0.05K/s.

VII. EXPERIMENTAL RESULTS

7.1 Optical Characterization

The thickness and the optical properties of the samples were calculated from the measurement results using a B-Spline model. The model included a 2.21 nm thick native SiO₂ layer. The thickness of this oxide was determined from ellipsometric measurements performed on a Si substrate.

7.1.1 Optical Properties of NiO (Low and High O Sputtering Pressure)

The optical properties of the NiO films were calculated from the measurement results using the following B-Spline models:

(a) NiO (Low O Sputtering Pressure)

Include Surface Roughness = ON Roughness = 30.57 nm (fit)

Layer # 2 = <u>B-Spline</u> Thickness # 2 = <u>436.62 nm</u> (fit)
Layer # 1 = <u>NTVE_JAW</u> Native Oxide = <u>2.21 nm</u>
Substrate = <u>SI_JAW</u>

Angle Offset = 0.270 (fit)

(b) NiO (High O Sputtering Pressure)

Include Surface Roughness = ON Roughness = 17.67 nm (fit)

Layer # 2 = <u>B-Spline</u> Thickness # 2 = <u>316.20 nm</u> (fit)
Layer # 1 = <u>NTVE_JAW</u> Native Oxide = <u>2.21 nm</u>
Substrate = <u>SI_JAW</u>

Angle Offset = 0.00

Figure 7.1 B-Spline Multi-layers Fitting for NiO. (a) NiO (Low O Sputtering Pressure). (b) NiO (High O Sputtering Pressure).

The results shows that for low energies, the optical constants of NiO sputtered at low O pressure are slightly lower than those of NiO sputtered at high O pressure, and the refractive index for NiO is around 2 (see Figure 9.2(a)). NiO sputtered at high O pressure is more absorbing than the one sputtered at low O pressure at higher photon energies.

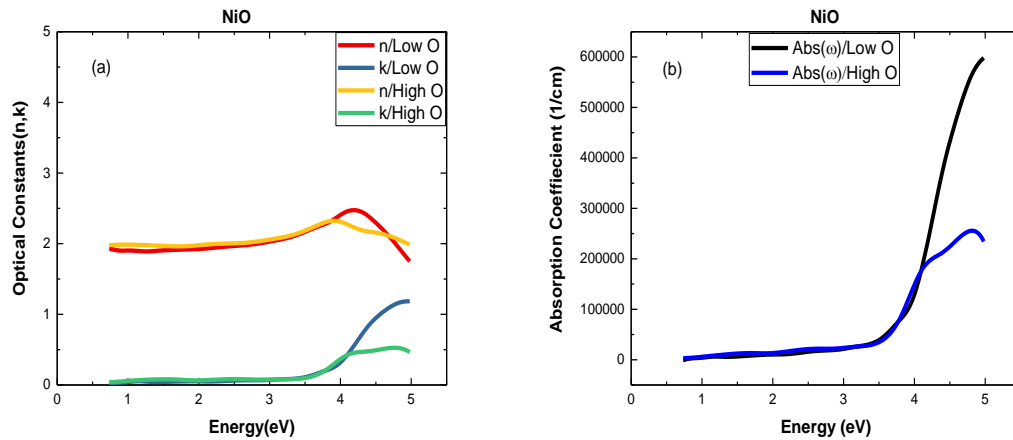


Figure 7.2 Measured optical properties for NiO (Low and high O sputtering pressure). Optical constants ($n(\omega)$, $k(\omega)$) (a), and absorption coefficient $\alpha(\omega)$ (b).

7.1.2 Optical Properties of $Ni_{0.8}Fe_{0.8}O_{1-\delta}$ (Low and High O Sputtering Pressure)

The optical properties of the NiFeO films were calculated from the measurement results using the following B-Spline models:

(a) NiFeO (Low O Sputtering Pressure)

Include Surface Roughness = ON Roughness = 32.05 nm (fit)

Layer # 3 = <u>B-Spline</u> Thickness # 3 = <u>282.84 nm</u> (fit)
--

Layer # 2 = <u>SIO2_JAW</u> Thickness # 2 = <u>1.20 nm</u>
--

Layer # 1 = <u>INTR_JAW</u> Thickness # 1 = <u>1.00 nm</u>
--

Substrate = <u>SI_JAW</u>

Angle Offset = 0.00800

(b) NiFeO (High O Sputtering Pressure)

Include Surface Roughness = ON Roughness = 6.81 nm (fit)

Layer # 3 = <u>B-Spline</u> Thickness # 3 = <u>261.59 nm</u> (fit)
--

Layer # 2 = <u>SIO2_JAW</u> Thickness # 2 = <u>1.20 nm</u>
--

Layer # 1 = <u>INTR_JAW</u> Thickness # 1 = <u>1.00 nm</u>
--

Substrate = <u>SI_JAW</u>

Angle Offset = 0.00800

Figure 7.3 B-Spline Multi-layers Fitting for NiFeO. (a) Ni_{0.8}Fe_{0.2}O (Low O Sputtering Pressure). (b) NiFeO (High O Sputtering Pressure).

For high energies, the optical constants (extinction coefficient) for (NiFe) Oxide sputtered at low O pressure are higher than those of (NiFe) Oxide sputtered at high O pressure, and for low energies, the optical constants are almost identical for both materials, and yet in this energy regime, the absorption is approximately the same, whereas at high energies, (NiFe) Oxide sputtered at low O pressure is more absorbing than the one sputtered at high O pressure. Like for NiO, the refractive index for NiFe Oxide at the lowest energy is approximately equal to 2 (see Figure 7.4(a)).

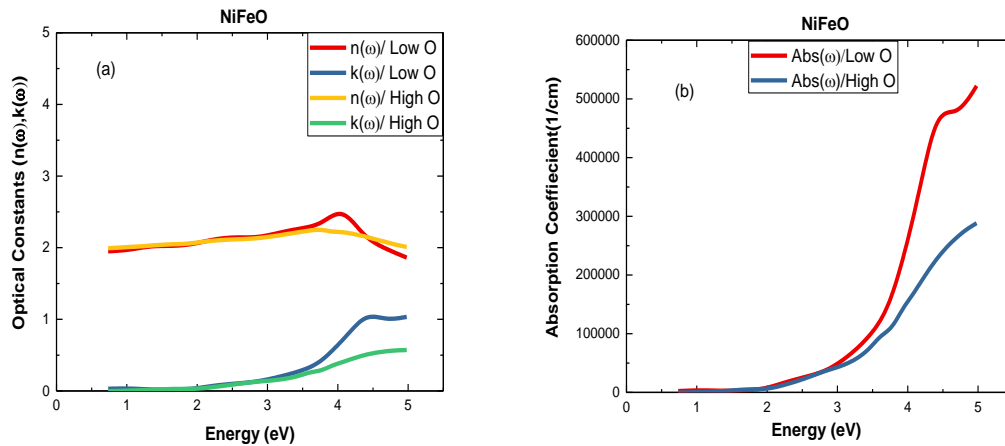


Figure 7.4 Measured optical properties for NiFe Oxide (Low and high O sputtering pressure). Optical constants ($n(\omega)$, $k(\omega)$) (a), absorption coefficient $\alpha(\omega)$ (b).

The Figure 7.5 (a) shows that the optical constant (k) for $\text{Ni}_{0.8}\text{Fe}_{0.2}\text{O}_{1-\delta}$ (Low O) is higher than that for NiO (Low O) for the energy ranging from ~ 1 to ~ 4 eV and the opposite for the energy ranging from ~ 4 to ~ 4.8 eV. The optical constant (n) is the same for both samples for the energy ranging from 1 to 2eV, from 2 to ~ 4.5 eV the optical property (n) for $\text{Ni}_{0.8}\text{Fe}_{0.2}\text{O}_{1-\delta}$ (Low O) is greater than that for NiO (Low O), and from ~ 4.5 to 5 eV the optical property (n) for $\text{Ni}_{0.8}\text{Fe}_{0.2}\text{O}_{1-\delta}$ (Low O) is lower than that for NiO (Low O).

The Figure 7.5 (b) also shows that the optical constant (k) for $\text{Ni}_{0.8}\text{Fe}_{0.2}\text{O}_{1-\delta}$ (Low O) is higher than that for NiO (Low O) for the energy ranging from ~ 1 to ~ 3.8 eV, and from ~ 4.25 to ~ 5 eV both samples seem to have the same (k). The optical constant (n) is the same for both samples for the energy ranging from 1 to 2.25 eV, from 2.25 to ~ 4 eV the optical property (n) for $\text{Ni}_{0.8}\text{Fe}_{0.2}\text{O}_{1-\delta}$ (Low O) is greater than that for

NiO (Low O), and from ~4 to 5 eV both samples have almost the same the optical constant (n).

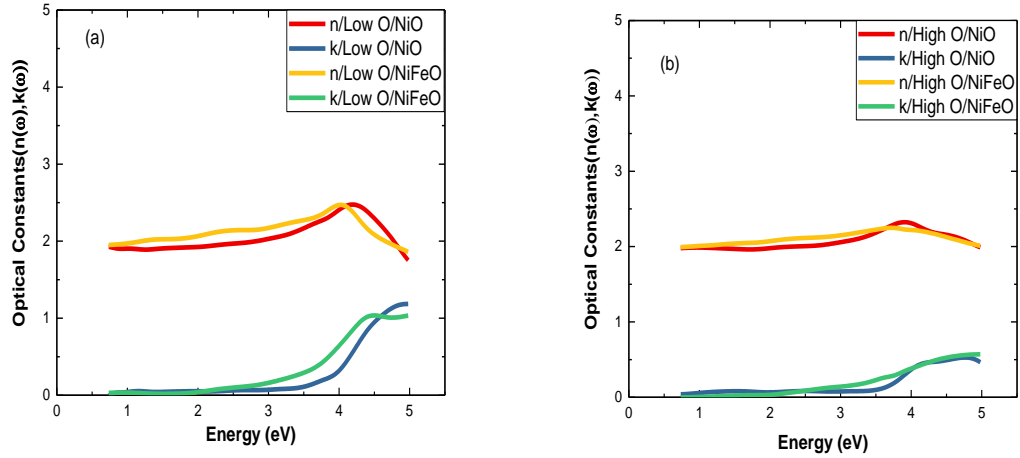


Figure 7.5 Optical properties of NiO (Low O) vs. those of $\text{Ni}_{0.8}\text{Fe}_{0.2}\text{O}_{1-\delta}$ (Low O) (a), optical properties of NiO (High O) vs. those of $\text{Ni}_{0.8}\text{Fe}_{0.2}\text{O}_{1-\delta}$ (High O) (b).

7.2 Magnetic Characterization

7.2.1 Magnetic Properties for NiO (Low and High O Sputtering Pressure)

Figure.7.6 shows the data measured on the NiO sample sputtered at low oxygen (Low O) concentration. Figure.7.6a shows the ZFC and FC magnetic moment for NiO (Low O) sample cooled and measured at 9 Tesla. Figure.7.6b shows the ZFC and FC magnetic moment for NiO (Low O) sample cooled and measured at 0.3 Tesla, and Figure. 7.6c. shows the ZFC and FC for NiO (Low O) sample cooled at 9Tesla and measured at 0.3 Tesla. Figure.7.6d shows the hysteresis curve measured at RT.

For the NiO sample with low O concentration, the magnetic moment $m(T)$ measured at 9 Tesla is higher than the moment $m(T)$ measured at 0.3 Tesla, which indicates that the sample is not diamagnetic. The moment $m(T)$ for the FC curve measured at 0.3 Tesla, after the sample cooling at 0.3 Tesla is almost identical of the one measured 0.3 Tesla, after the sample cooling at 9 Tesla. Both ZFC and FC curves show peaks at the same temperature of 54.75 K. For the measurement at 9 Tesla, the peak for the FC curve is higher than the one for the ZFC curve, whereas, both ZFC and FC have peaks of same magnitude for the measurement at 0.3 Tesla; this shows that the height of the peak at 54.75K is influenced by the intensity of the applied magnetic field.

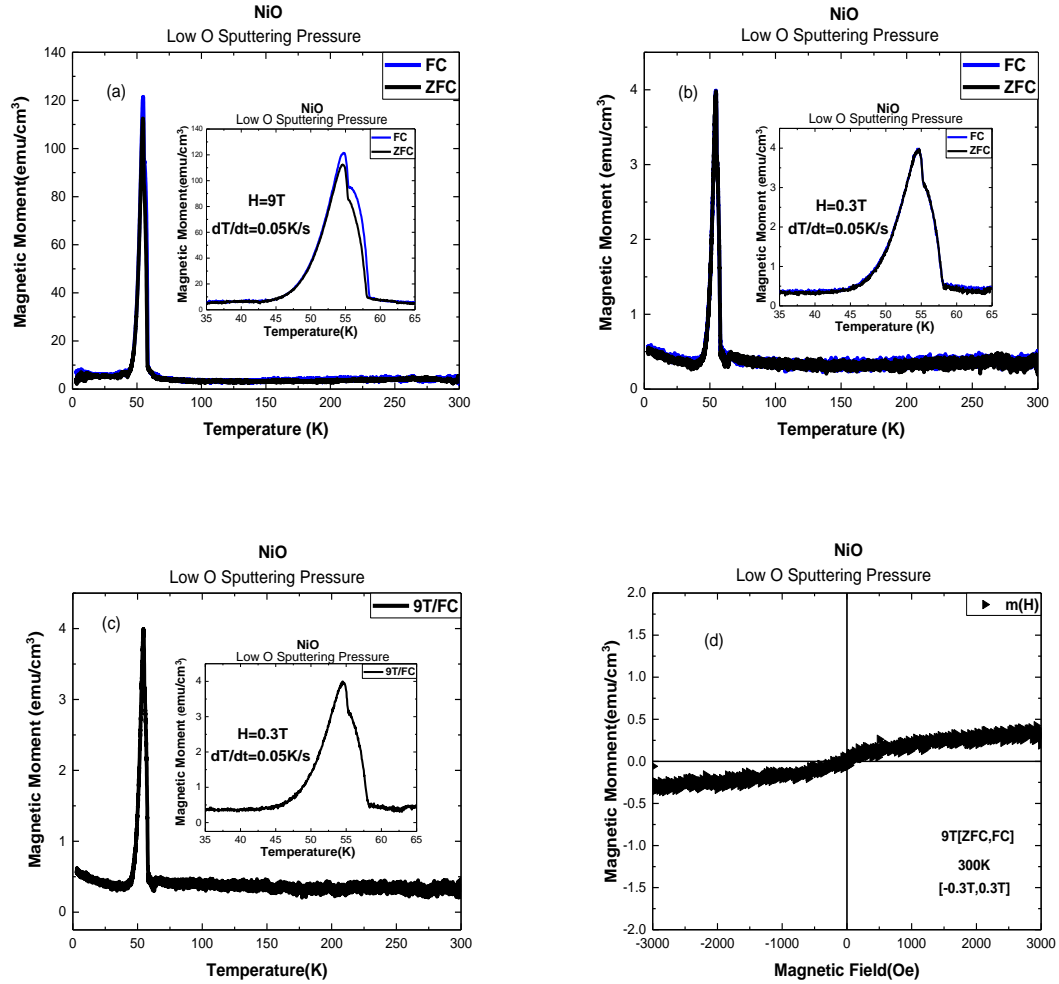


Figure 7.6 Magnetic properties for NiO sputtered at low O pressure. Magnetic moment as function of temperature: (a) ZFC and FC (9 tesla) curves measured at 9 Tesla, (b) ZFC and FC magnetic moment for NiO (Low O) cooled and measured at 0.3 Tesla, (c) ZFC and FC magnetic moment for NiO (Low O) cooled at 9 Tesla and measured at 0.3 Tesla, and magnetic moment as function of the applied magnetic field: (d) from -0.3 to 0.3 Tesla.

The magnetic moment $m(H)$ measured from -9 to +9 Tesla also shows that dependence on the temperature. The magnetic moment $m(H)$ at 300K is greater than those measured at 200K. The moment $m(H)$ also shows a paramagnetic jump around the origin which is more noticeable for $m(H)$ at 200K, and at 300K.

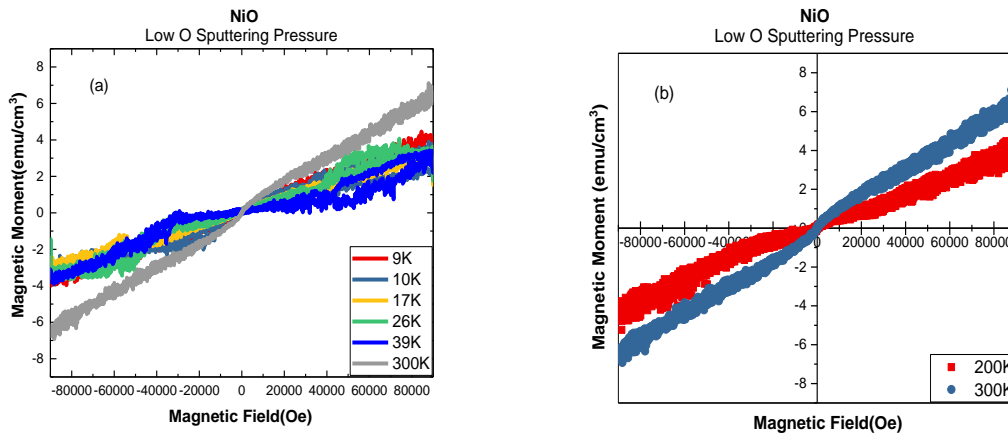


Figure 7.7 Magnetic moment $m(H)$ per unit volume of NiO (Low O) measured from -9 to +9 Tesla at different temperatures. The magnetic moments at temperatures below 54.75 K vs. the magnetic moment at 300K (a), the magnetic moment at temperatures above 54.75K.

Some similarities for NiO sputtered at low O pressure were also observed for the one sputtered at high O pressure. For example, the magnetic moment $m(T)$ measured at 9 Tesla is also higher than the moment $m(T)$ measured at 0.3 Tesla. And FC curves obtained at 0.3 Tesla after sample cooling at 0.3 Tesla and 9 Tesla are also almost identical. Both ZFC and FC curves obtained at 9 Tesla and 0.3 Tesla have peaks at the same temperature of 54.75 K. The peak for the FC curve is higher than the peak for the ZFC curve for 9 Tesla case, and ZFC and FC curves have peaks of same magnitude for measurements at 0.3 Tesla after sample cooling at 0.3 Tesla and at 9 Tesla after sample cooling at 0.3 Tesla respectively.

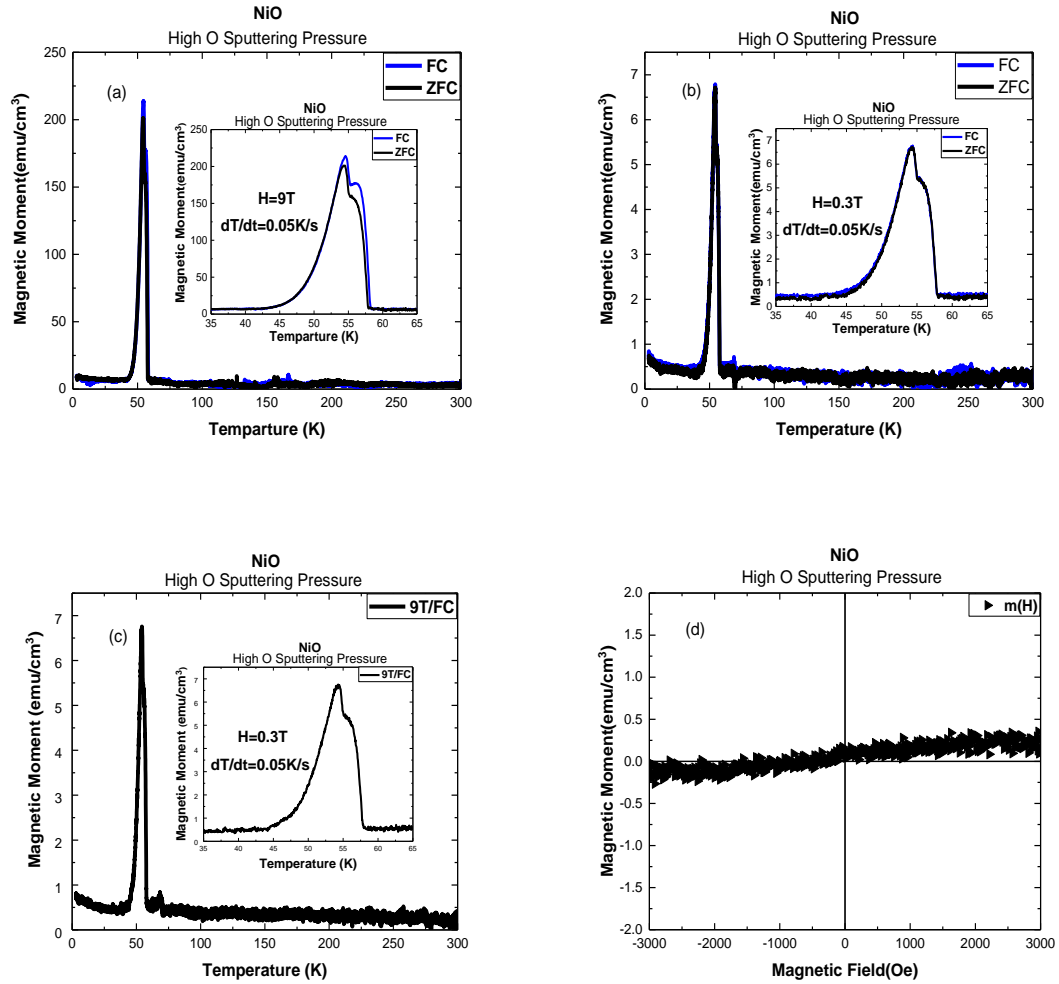


Figure 7.8 Magnetic properties for NiO sputtered at high O pressure. Magnetic moment $m(T)$ as function of temperature: (a) ZFC and FC (9 Tesla) magnetic moments measured at 9 Tesla, (b) ZFC and FC (0.3 Tesla) magnetic moments measured at 0.3 tesla, (c) ZFC and FC (9 Tesla) magnetic moments measured at 0.3 Tesla, and magnetic moment as function of the applied magnetic field: (d) from -0.3 Tesla to 0.3 Tesla measured after ZFC, and FC curves measurement at 9 Tesla.

However, due to the difference in O sputtering pressure, the magnetic moment $m(T)$ for NiO sputtered at low O pressure is higher than the one of NiO sputtered at high O pressure. And yet, the peak for NiO sputtered at high O pressure is higher than the peak for NiO sputtered at low O pressure. Excluding the maximum peak, the magnetic moment $m(T)$ of NiO sputtered at high O pressure decreases as the temperature increases.

The magnetic moment $m(H)$ measured from -9 to 9 Tesla at different temperature shows a decrease in magnetic moment as the temperature increases (see Figure 7.9), this is in agreement with the measurement of $m(T)$ illustrated by Figure 7.8. There is the ferromagnetic phase that decreases as the temperature increases, to leave place to the antiferromagnetic phase.

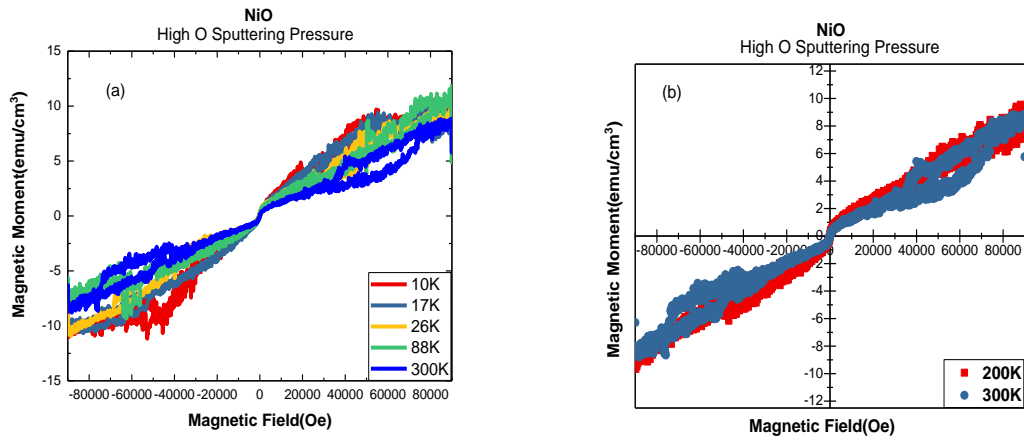


Figure 7.9 Magnetic moment $m(H)$ per unit volume for NiO samples measured from -9 to 9 Tesla at different temperatures.

Also, at 300K the magnetic moment $m(H)$ per unit volume shows that NiO sputtered at low O pressure is greater than the one for NiO sputtered at high O pressure. And NiO sputtered at high O pressure has a very noticeable moment jump at the zero magnetic field (H). The moment $m(H)$ for NiO sputtered at high O pressure shows a vortex structure (see Figure 7.10) at high magnetic field. This could be due to antiferromagnetic domains in the sample. Normally, we may think that NiO sputtered at high O pressure has to be antiferromagnetic as the DFT calculation of bulk NiO shows; however the antiferromagnetic configuration can easily happen in bulk materials whereas

the moments in the boundary layers prevent thin films from being perfectly antiferromagnetic.

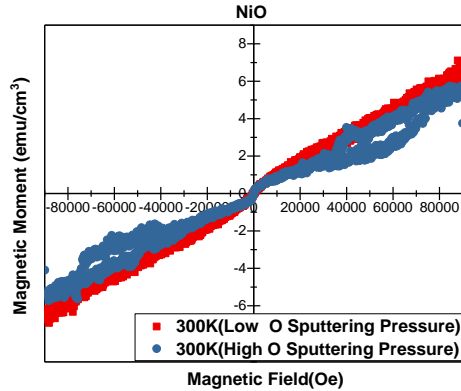


Figure 7.10 Magnetic moment $m(H)$ per unit volume at 300K for NiO samples, one sputtered at low O pressure, and another sputtered at high O pressure. The moment $m(H)$ shows the magnetic vortex at high magnetic fields.

For both low and high O sputtering pressure cases, the magnetic moment $m(T)$ obtained at 9 Tesla is greater than the one measured at 0.3 Tesla, this shows that the samples are not diamagnetic. And both ZFC and FC curves have peaks at the temperature of 55.75K. The magnetic moment $m(T)$ per unit volume for NiO sputtered at low O pressure is greater than the one sputtered at high O pressure.

7.2.2 Magnetic Properties for $Ni_{0.8}Fe_{0.2}O_{1-\delta}$ (Low and High O Sputtering Pressure)

For NiFe Oxide sputtered at low O pressure, the magnetic moment $m(T)$ measured at 9 Tesla is greater than the one measured at 0.3 Tesla. For both cases, the

ZFC and FC curves have peaks at the same temperature of 54.75K, and for the magnetic moment measured at 9 Tesla, the FC curve has a higher peak than the ZFC curve, but both curves have peaks of the same height for the magnetic moment measured at 0.3 Tesla. Excluding the peak, the magnetic moment increases as the temperature increases.

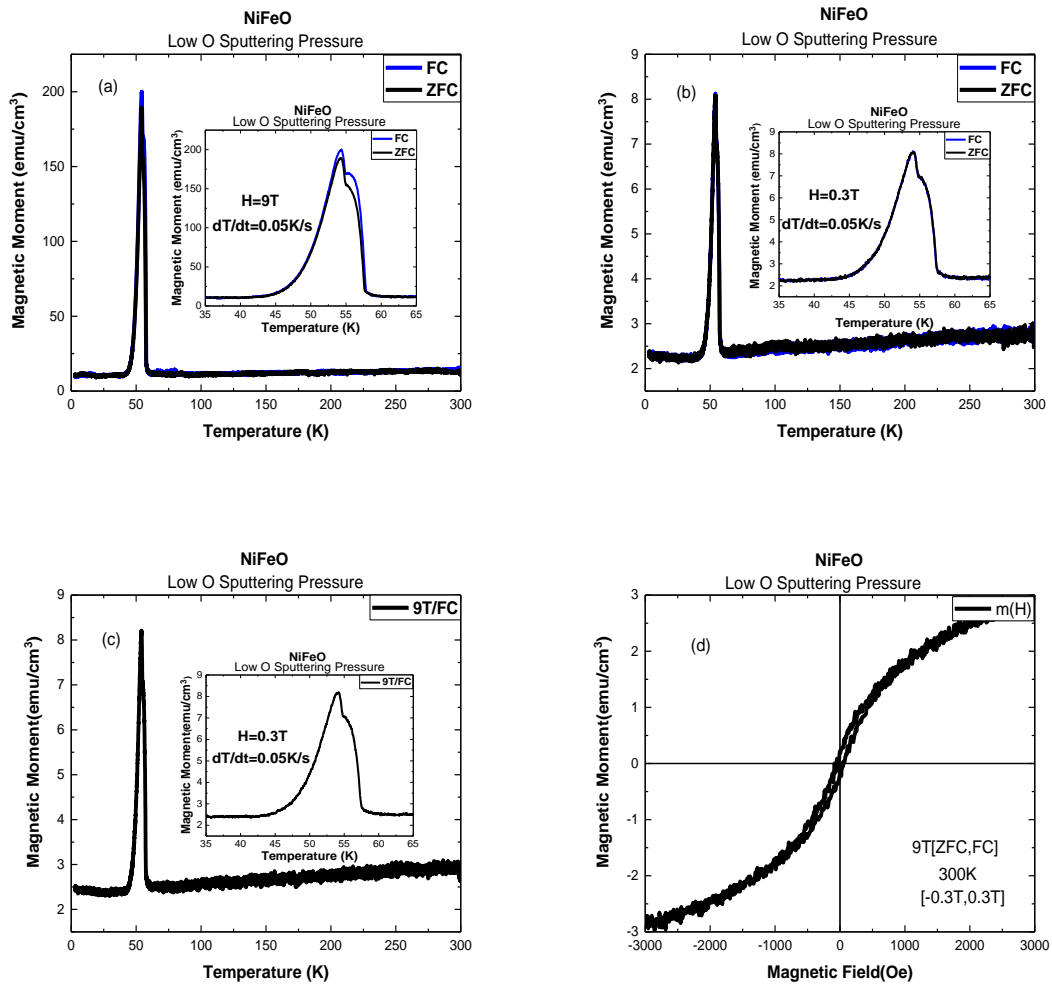


Figure 7.11 Magnetic Properties for $\text{Ni}_{0.8}\text{Fe}_{0.2}\text{O}_{1-\delta}$ sputtered at low O pressure. ZFC and FC curves obtained with the applied magnetic field of 9 Tesla (a), and 0.3 Tesla (b). 9T/FC curve obtained at 0.3 Tesla (c). Magnetic moment as function of the applied magnetic field from -3 Tesla to 3 Tesla measured after ZFC, and FC curves at 9 Tesla (d).

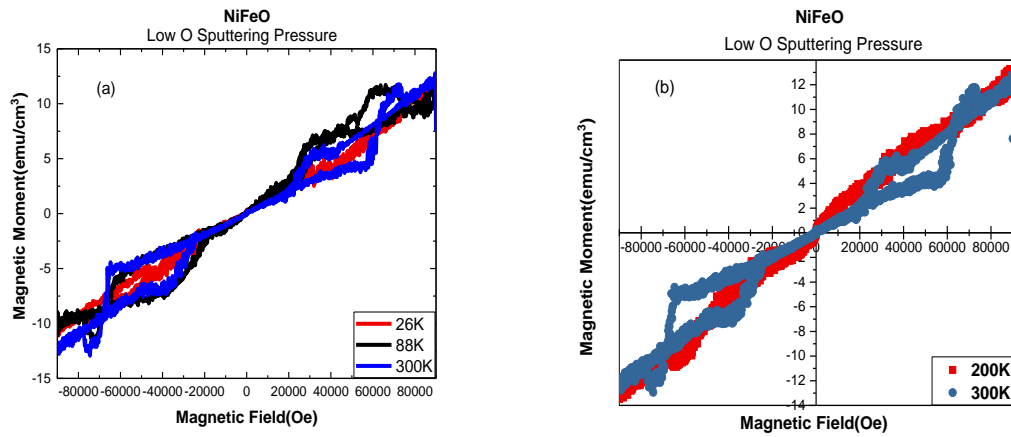


Figure 7.12 Magnetic moment $m(H)$ per unit volume for $\text{Ni}_{0.8}\text{Fe}_{0.2}\text{O}_{1-\delta}$ samples. Magnetic moments $m(H)$ measured at temperatures 26K, 88K, and 300K (a). Magnetic moment $m(H)$ measured at 200K, and 300K (b).

For NiFeO sputtered at high O pressure, the magnetic moment $m(T)$ measured at 9Tesla is greater than the one measured at 0.3Tesla. For both cases, the ZFC and FC curves have peaks at the temperature of 54.75K, and for the magnetic moment measured at 9Tesla, the FC curve has a higher peak than the ZFC curve, but for the magnetic moment $m(T)$ measured at 0.3Tesla, both curves have a peak of the same height. Excluding the peak, the magnetic moment decreases as the temperature increases. At low temperature below 25 K a peak which is not present in any of the other samples is observed in both the FC and ZFC curves. The height of ZFC curve is consistently lower than the height of the FC curve. The height of this low temperature peak increases by a factor of 4 when the applied field is increased by a factor of 30.

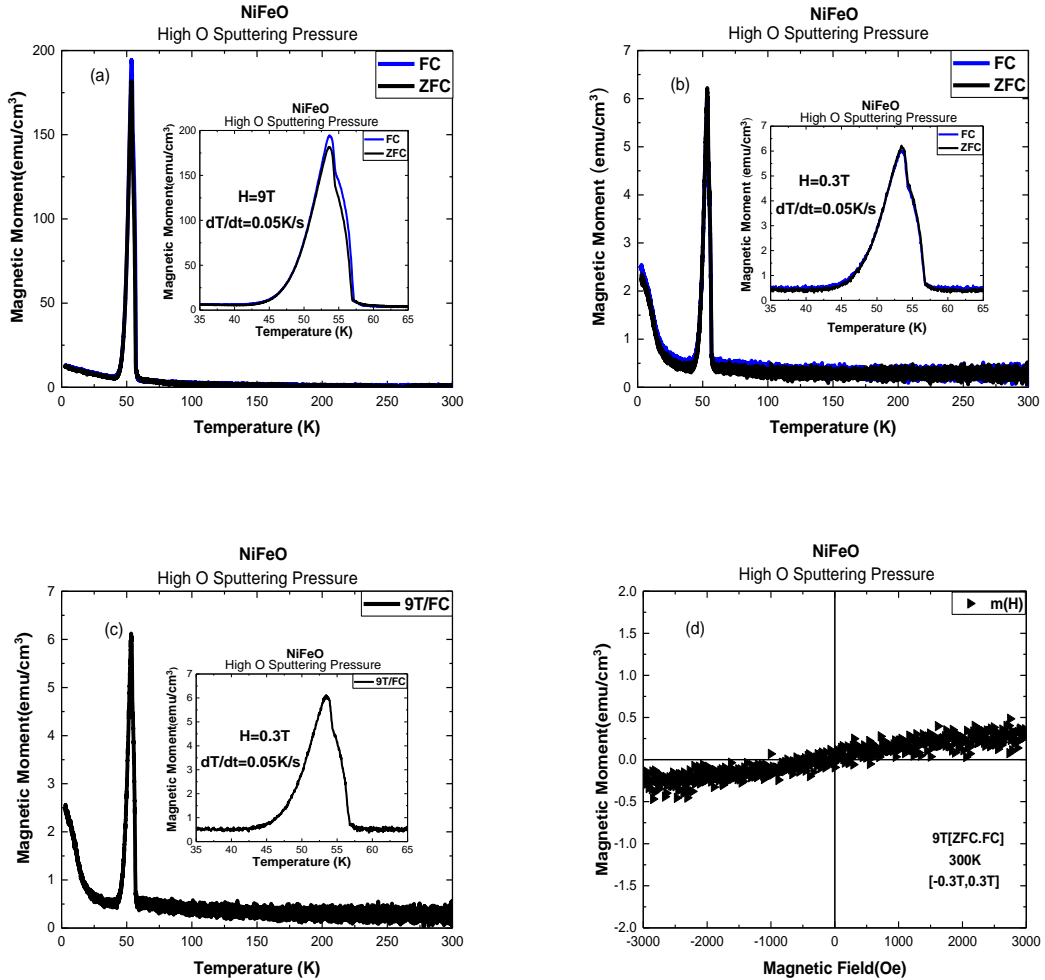


Figure 7.13 Magnetic Properties for $\text{Ni}_{0.8}\text{Fe}_{0.2}\text{O}_{1-\delta}$ sputtered at high O pressure. ZFC and FC curves obtained with the applied magnetic field of 9 Tesla (a), and 0.3 Tesla (b). 9T/FC moment measured at 0.3 Tesla (c). Magnetic moment as function of the applied magnetic field from -9 to 9 Tesla (d).

The $m(H)$ at different temperatures shows the paramagnetic jump around the origin decreases as a function of the temperature. For low temperatures, each $m(H)$ curve has the noticeable magnetic vortex at high applied magnetic field. Also the magnetic

moment $m(H)$ decreases slightly as the temperature increases (see Figure 7.14), this is in agreement with the $m(T)$ measurement (see Figure 7.13).

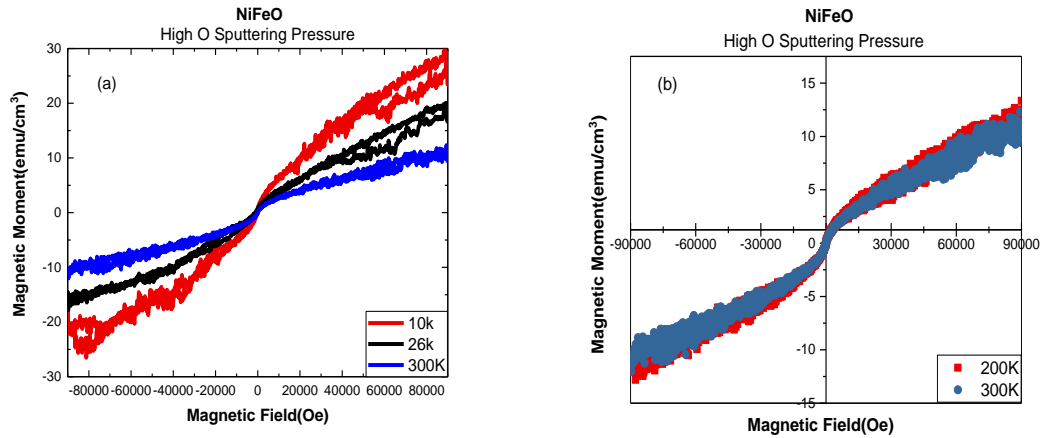


Figure 7.14 Measured magnetic moment $m(H)$ per unit volume at different temperature for $\text{Ni}_{0.8}\text{Fe}_{0.2}\text{O}_{1-\delta}$ sample sputtered at high O pressure. The moment $m(H)$ at 10K, 26K, and 300K (a), the moment $m(H)$ at 200K, and 300K.

At 300K, there is a magnetic moment jump around the zero magnetic field for NiFeO sputtered at high O pressure. For low magnetic field, the magnetic moment for NiFeO sputtered at high O pressure is higher than the one for NiFeO sputtered at low O pressure.

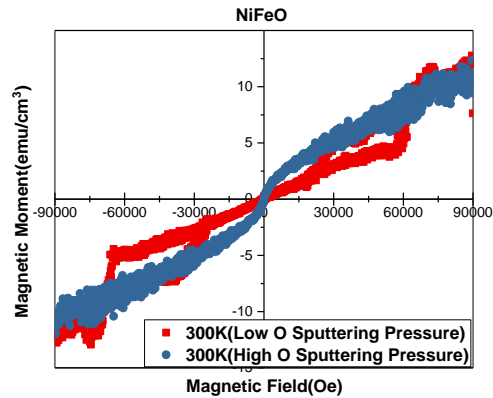


Figure 7.15 Measured magnetic moment $m(H)$ per unit volume at 300K for NiFeO sputtered at low O pressure, and NiFeO sputtered at high O pressure.

The double peak is present in the $m(T)$ for all samples. The position of the peak suggests that it originates from O_2 condensed on the sample. Notice that the peak is exactly situated at the melting temperature of O_2 ; in addition, the PPMS manual [97] says that the O_2 contamination may lead to a peak for a measurement of magnetic moment below 100K. The double peak we observed looks similar to the peak observed by Dubroca et al. (2006) [98] on a single Si wafer.

Two types of measurements were made to exactly learn about its true origin. The first of the measurements consisted of measuring the magnetic moment $m(T)$ of the substrate, to achieve that, the sample holder had to be fully covered by the substrate using the rubber cement (glue) to suppress the effect of the substrate. And the second measurement consisted of measuring the magnetic moment $m(T)$ of the sample holder only. Figure 7.16 shows measurements of $m(T)$ for sample holder+ substrate, and the

sample holder only. Both results also show the same peak at almost the same temperature, thus this indicates that this peak has nothing to do with the sample.

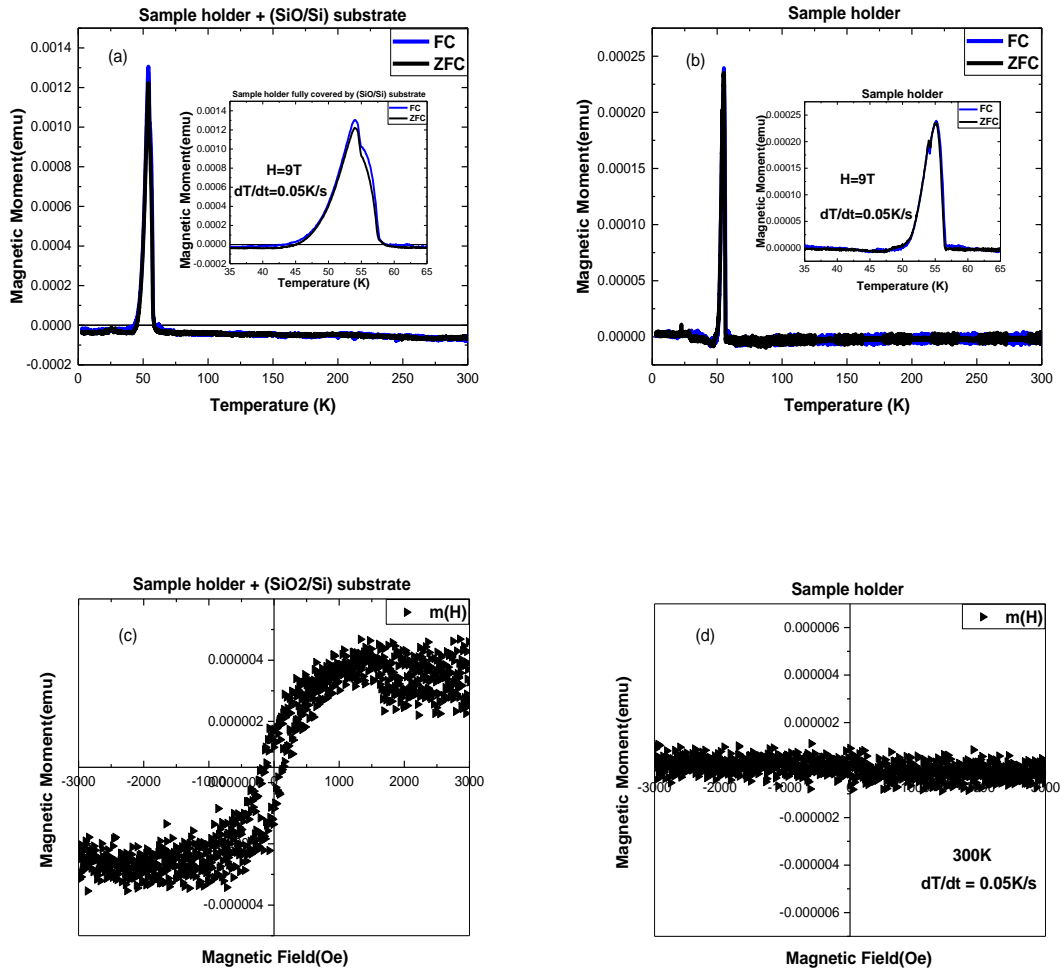


Figure 7.16 Measured magnetic moment $m(T)$ at 9 Tesla of the sample holder+substrate (a), and the sample holder only (b). The moment $m(H)$ for the sample holder+substrate (c). The moment $m(H)$ for the sample holder only (d).

The interpretation of the results shown in Figure 7.16 is not straightforward. The observed moment suggests that if condensed oxygen is causing the peak that the oxygen

film is not homogeneous across the sample holder. Notice also the large difference in moment between the bare sample-holder and the sample-holder covered with substrate tiles. The latter also contains rubber cement with air bubbles, and the surface area is not constant across the length of the quartz sample holder because of the small gaps between the substrate tiles.

7.3 Summary

The magnetic properties of RF sputtered NiO and $\text{Ni}_{0.8}\text{Fe}_{0.2}\text{O}_{1-\delta}$ thin films vary with oxygen and iron concentration. Films sputtered with low oxygen flow rate have a slightly higher magnetization at room temperature than films sputtered at higher O flow rate. Excepting the NiO films, the magnetic moment of films sputtered at low O flow rate seems to increase as a function of temperature; this is due of the presence of the ferromagnetic components in the sample which is characteristic of ferromagnetic phases according to J. Khemprasit et al. [39]. And these films are ferromagnetic at room temperature which is agreement with Yuan-Hua Lin et al. [34], and P. Douvalis et al. [35] since the RXD at room temperature may not detect the impurity phase. Doping with Fe increases the magnetization with a factor 4-6 for low O flow condition. For high O flow conditions, the Fe-doping significantly changes the magnetization below 25 while the magnetization at RT is hardly affected.

The magnetic moment of films sputtered at high O flow decreases as the temperature increases, this may be due to the particle size effect since J. Khemprasit et al. [39] claim that the particle size increases with increasing temperature, and this leads to the decline of the magnetic moment $m(T)$. Also as the temperature increases more

thermal energy is available and this excess energy may lead to the magnetic disorder in the samples causing the decline of the magnetic moment $m(T)$.

The dual higher peaks around 54.75K are caused by the condensed O_2 according to our results which also agree with [97], [98]. Our DFT results show that bulk NiO and 12.5 at. % Fe-doped NiO is antiferromagnetic, and J. Petersen et al. [84] found the same for 25 at. % Fe-doped NiO, however the experiment shows NiO and $Ni_{0.8}Fe_{0.2}O_{1-\delta}$ sputtered at high O flow show weak magnetic moment which is possible due to the presence of a ferromagnetic phase, this phase may be due to the surface to volume effect since our samples are not completely considered as bulk even though they are thick enough. Since there are small gaps between the substrate tiles (see Figure 6.10), a small amount of glue used to stick the substrates on the sample holder may fill them (gaps), according to Quantum Design Inc. [101] this glue can also contribute to the measured magnetic moment. Also note that the magnetic moments in the samples can also originate from impurities as for example discussed by M.A. Garcia [102]. For the AJA system there are two main contamination sources, the sputter gases (Ar is 5N and O_2 is 4N4) and the sputter targets (99.94% for $Ni_{0.8}Fe_{0.2}$ and 99.99% for Ni).

VIII.DISCUSSION

(A) Overall Summary

The theory shows that NiO is an antiferromagnetic semiconductor with a band gap which depends on the Hubbard potential U . Also Fe-doped NiO appears to be a semiconductor. The calculated Ni magnetic moment is less than that of Fe. Calculated Ni and Fe magnetic moments are in good agreement with values found in the literature. Calculations show that for a 32-atom supercell, 6.25 at.% Fe-doped NiO is a p-type semiconductor, but not antiferromagnetic due to non-zero net magnetic moment. According to the above finding that the Ni magnetic moment is different from that of Fe strictly speaking, such supercell is ferri-magnetic. On the contrary 12.5 at.% Fe-doped NiO, i.e two Fe atoms per supercell, is antiferromagnetic; this indicates that the magnetic nature depends on the amount of Fe dopants and the site they reside on. In addition, calculations for optical properties show that the refractive index (n) in the lowest energy regime for both materials is in good agreement with our experiment and [84]; note that the static real dielectric function also depends on the Hubbard energy. However, both materials generally have different optical properties.

The experiment shows that all samples are not diamagnetic since the magnetic moment change is in the same direction as the applied magnetic field. RF sputtered NiO thin films grown on SiO₂/Si have a small magnetic moment. Although the origin of this moment is not clear, it is most probably due to magnetic moments in the grain boundaries, on the surfaces, or in the defects of the thin films. The glue (rubber cement) used to mount the sample [101], or magnetic impurities originating from the sputter gas

or targets can also contribute [102]. As expected, NiFeO thin films grown on SiO₂/Si have a small magnetic moment in the applied magnetic field.

The magnetic moment also depends on the O sputtering pressure, for example, at room temperature the magnetic moment per unit volume of NiO sputtered at low O pressure is higher than that of NiO sputtered at high O pressure. In addition, the magnetic moment per unit volume of NiFeO sputtered at low O pressure is higher than that of NiFeO sputtered at high O pressure. While, in the low energy regime, the experimental optical properties are in better agreement with those obtained theoretically, for high energies, there is a noticeable difference. Our static refractive index (n) is about 2 which is 4% lower than [103], this may be due to the thickness and density of our samples.

Other reasons for the observed differences between the experiment and theory might be due to countless defects present in our polycrystalline samples. In addition, unlike the experiment, DFT calculations were performed at zero Kelvin (K), this suggests that the temperature difference between experiment and calculation might also be responsible for the observed differences.

(B) Future Works

It would be interesting to compare the results of the DFT calculations with the optical properties of epitaxial NiFeO thin films with larger crystallites and less grain boundaries. Permalloy oxide can be grown epitaxially on MgO (100) or Bi-YIG (111) by dual ion beam sputtering [99]. As DIBS allows sputtering at much lower pressure, the density of such films is expected to be much higher than those of RF sputtered films.

Another approach would be to further explore the effect of defects; in particular oxygen vacancies on the optical properties [100]. Such approach could involve the use of effective medium approximations to partly model the polycrystalline nature of the films.

Regarding the observed magnetic properties works needs to be done to further detail their origin. Magnetic measurements as a function of the film thickness could reveal whether the magnetic moment is homogeneously distributed through the film or is maybe concentrated in the seed-layer which has the smallest crystallites. Scanning probe microscopy measurements (including AFM, MFM, and conductive AFM) could reveal a correlation between film structure, magnetic moment, and conductivity useful for systematic switching studies of MRAM devices.

APPENDIX SECTION

APPENDIX A

Units:

emu	electromagnetic units
Oe	Oersted
μ_B	Bohr magneton

APPENDIX B

The variation of the energy functional E:

$$\begin{aligned}
 \delta E[\Psi] &= E[\Psi + \delta\Psi] \\
 &= \frac{\langle \Psi + \delta\Psi | \hat{H} | \Psi + \delta\Psi \rangle}{\langle \Psi + \delta\Psi | \Psi + \delta\Psi \rangle} - \frac{\langle \Psi | \hat{H} | \Psi \rangle}{\langle \Psi | \Psi \rangle} \\
 &= \frac{\langle \delta\Psi | \hat{H} | \Psi \rangle + \langle \Psi | \hat{H} | \delta\Psi \rangle}{\langle \Psi | \Psi \rangle} - \frac{\langle \Psi | \hat{H} | \Psi \rangle}{(\langle \Psi | \Psi \rangle)^2} \left(\langle \delta\Psi | \Psi \rangle + \langle \Psi | \delta\Psi \rangle \right) + O(\delta\Psi^2) \\
 &= \frac{1}{\langle \Psi | \Psi \rangle} \left[\langle \delta\Psi | (\hat{H} | \Psi \rangle - E[\Psi] | \Psi \rangle) + \left\{ \langle \delta\Psi | (\hat{H} | \Psi \rangle - E[\Psi] | \Psi \rangle) \right\}^* \right]
 \end{aligned}$$

The variation of the energy functional for the state $|\Psi\rangle = \left| \Psi_0 + \sum_{n=1}^{\infty} a_n \Psi_n \right\rangle$, with

$\hat{H}|\Psi_n\rangle = E_n|\Psi_n\rangle$, is given by:

$$\begin{aligned}
E[\Psi] &= \frac{\langle \Psi | H | \Psi \rangle}{\langle \Psi | \Psi \rangle} \\
&= \frac{\left\langle \Psi_0 + \sum_{n=1}^{\infty} a_n \Psi_n \left| \hat{H} \right| \Psi_0 + \sum_{n=1}^{\infty} a_n \Psi_n \right\rangle}{\left\langle \Psi_0 + \sum_{n=1}^{\infty} a_n \Psi_n \left| \Psi_0 + \sum_{n=1}^{\infty} a_n \Psi_n \right\rangle} \\
&= \frac{\left\langle \Psi_0 + \sum_{n=1}^{\infty} a_n \Psi_n \left| E_0 \Psi_0 + \sum_{n=1}^{\infty} a_n E_n \Psi_n \right\rangle}{\left\langle \Psi_0 + \sum_{n=1}^{\infty} a_n \Psi_n \left| \Psi_0 + \sum_{n=1}^{\infty} a_n \Psi_n \right\rangle} \\
&= \frac{E_0 + \sum_{n=1}^{\infty} |a_n|^2 E_n}{1 + \sum_{n=1}^{\infty} |a_n|^2} \\
&= E_0 + \sum_{n=1}^{\infty} (|a_n|)^2 (E_n - E_0) + O\{|a_n|^4\}
\end{aligned}$$

REFERENCES

- [1] J.F. Gibbons, and W.E. Beadle, *Solid State Electronics*, Pergamon Press, Vol.7, pp 785-797 (1964).
- [2] D. Ielmini, F. Nardi and C. Cagli, IOP Publishing, *Nanotechnology* 22, 254022 (2011)
- [3] S. H. Chang et al. *Appl. Phys. Lett.* 92, 183507 (2008).
- [4] T. Katase, T. Onozato, M. Hirono, T. Mizuno, and H. Ohta. *Journal of Nature /Scientific Reports* (2016).
- [5] G. Cai, J. Wang, and P. S. Lee, *Acc. Chem. Res.*, 49 (8), pp 1469–1476 (2016).
- [6] X. Xin and Y. L. Xin, *NiO coating for smart window application by reaction flash evaporation of nickel*, Proc. SPIE 2892, Display Devices and Systems, 279 (1996).
- [7] P. Mallick, N. C. Mishra, *American Journal of Materials Science* 2(3): 66-71 (2012).
- [8] N. Mironova-Ulmane, A. Kuzmin, J. Grabis, I. Sildos, V.I. Voronin, I.F. Berger, V.A. Kazantsev. *Solid State Phenomena Vols. 168-169* pp341-344 (2011).
- [9] B. Koillert and L. M. Falicov, *J. Phys. C: Solid State Phys.* 8 695 (1975).
- [10] C. Tzschaschel, K. Otani, R. Iida, T. Shimura, H. Ueda, *Phys. Rev.B.*95, 174407 (2017).
- [11] A. I. Arbab, *Chin. Phys. B* Vol. 22, No. 3, 030301(2013).
- [12] B. Thide, *Electromagnetic Field Theory*, Upsilon Books (Calvin College, Michigan), Ch.1 pp 15-16 (2004).
- [13] J. Peatross, M. Ware, *Physics of Light and Optics*, (Brigham Young University, Utah), ch.2, pp 38-41 (2006).
- [14] M. J. Mageto, C. M. Maghanga, and M. Mwamburi, *The African Review of Physics*, 7:0011 (2012).
- [15] R. G. Brown, *Classical Electrodynamics*, (Duke University Physics Department, North Carolina), Ch.11, pp 122-124 (2007).
- [16] G. Tompkins, A. McGahan, *Spectroscopic Ellipsometry and Reflectometry: A User's Guide*, Wiley, App. C. 2, pp 212-217 (1999).

- [17] J. Pearson, *Lecture Notes on Solid State Physics*, (University of Manchester, UK), Ch. 1, pp 1-19 (2008).
- [18] C. Kittel, *Introduction to Solid State Physics*, 8th Ed., Ch.1 pp 2-5 (2008).
- [19] S. H. Simon, *Lectures for Solid State Physics*, (Oxford University, UK), Ch.13, pp 133-138 (2012).
- [20] M. Suzuki and I. S. Suzuki, *Lectures on Solid State Physics: Bloch theorem and Energy band*, (Department of Physics, State University of New York at Binghamton, New York), pp 11- 20 (2006).
- [21] I.R. Harris and A.J. Williams, *Magnetic Materials*, (School of Metallurgy and Materials, University of Birmingham, Birmingham, UK), Materials Science and Engineering– Vol. II – Magnetic Materials (2009).
- [22] T. DeGrand, *Quantum Physics*, (High Energy Physics, University of Colorado Boulder, Colorado), Ch. 2, pp 23-24 (2017).
- [23] N.-C. Yeh, *Advanced Condensed Matter Field Theory*, (ITAP Summer Lectures), Ch.1 pp 3- 6 (2009).
- [24] P. D. Haynes, *Linear-scaling methods in ab initio quantum-mechanical calculations*, (University of Cambridge, UK), Ch.2 pp 10-11 (1998).
- [25] W. C. CHEW, *Quantum Mechanics Made Simple: Lectures Notes*, (University of Illinois at Urban Champaign) Ch. 6, pp 59-63 (2012).
- [26] A.F.J.Levi. *Applied Quantum Mechanics*.2nd Ed., Ch. 8 pp 353-376 (2006).
- [27] M.Tadic, D. Nikolic, M. Panjan, G. Blake. *Magnetic properties of NiO (nickel oxide) nanoparticles: Blocking temperature and Neel temperature*. Journal of Alloys and Compounds 647 (2015) 1061-1068.
- [28] G. Ma, X. Tang, H. Su, Y. Li, H. Zhang, and Z. Zhong. *Effects of Standard Free Energy on NiO Bipolar Resistive Switching Devices*. IEEE Transactions on Electron Devices, Vol. 61, No. 5 (2014).
- [29] C. Liu, T. Tsao, Y. Tai, T. Leu, C. Ho, W. Tang, D. Miu .*Out-of-Plane Permalloy Magnetic Actuators for Delta-Wing Control*. IEEE (1995).
- [30] G. Zahnd, L. Vila, T. V. Pham, A. Marty, P. Laczkowski, W. S. Torres, C. Beigné, C. Vergnaud, M. Jamet, and J-P. Attané, *Nanotechnology* 27, 035201 (5pp) (2016).
- [31] I. Sugiyama, N. Shibata, Z. Wang, T. Yamamoto, Y. Ikuhara, *Nature Nanotechnology* 8, 266–270 (2013).

- [32] N. Mironova-Ulmane, A. Kuzmin, J. Grabis, I. Sildos, V.I. Voronin, I.F. Berger, V.A. Kazantsev, "Structural and Magnetic Properties of Nickel Oxide Nanopowders", *Solid State Phenomena*, Vols. 168-169, pp. 341-344 (2011).
- [33] Lin Y H, Wang J, Cai J, Ying M, Zhao R, Li M and Nan C W 2006 *Phys. Rev. B* 73 193308.
- [34] Y.-H. Lin, J. Wang, J. Cai, M. Ying, R. Zhao, M. Li, and C.-W. Nan, *Phys. Rev. B* 73, 193308 (2006).
- [35] A .P. Douvalis, L. Jankovic and T. Bakas, *J. Phys.: Condens. Matter* 19, 436203 (2007).
- [36] S. Manna, A. K. Deb, J. Jagannath, and S. K. De, *J. Phys. Chem. C* 2008, 112, 10659–10662.
- [37] S. Philip Raja and C. Venkateswaran, *J. Phys. D: Appl. Phys.* 42, 145001 (2009).
- [38] S. Liu, J. Jia, J. Wang, S. Liu, X. Wang, H. Song, X. Hu, *Journal of Magnetism and Magnetic Materials* 324, 2070–2074 (2012).
- [39] J. Khemprasit, S. Kaen-ngam, B. Khumpaitool, P. Kamkhon, *Journal of Magnetism and Magnetic Materials* 323, 2408–2412 (2011).
- [40] D.Y. Jiang, J.M. Qin, X. Wang, S. Gao, Q.C. Liang, and J.X. Zhao, *Vacuum* 86, 1083-1086 (2012).
- [41] M. Tyag, M. Tomar, V. Gupta, *Advanced Materials Research* Vols. 488-489 pp 103-108 (2012).
- [42] M. Guziewicz et al., *Optica Applicata*, Vol. XLI, No. 2 (2011).
- [43] A. Venter, J. R. Botha, *S Afr J Sci.*; 107(1/2), Art. #268, 6 pages (2011).
- [44] P.M. Ponnusamy, S. Agilan, N. Muthukumarasamy, T.S. Senthil, G. Rajesh, M.R. Venkatraman, D. Velauthapillai, *Materials Characterization* 114, 166–171(2016).
- [45] W. Haipeng, *Tsinghua Science and Technology*, Vol.: 11, Issue: 3 (2006).
- [46] J. S. Nkoma, and G. Ekosse, *J. Phys.: Condens. Matter* 11, 121–128 (1999).
- [47] R. Elliott, F. Rodrigues, C. A. Pickles and J. Peacey, *Canadian Metallurgical Quarterly*, 54:4, 395-405 (2015).
- [48] M. Winter, *Nickel Crystal Structure*, (The University of Sheffield, UK) (2006).

- [49] A. Furlan, J. Lu, L. Hultman, U. Jansson, and M. Magnuson, *Journal of Physics: Condensed Matter* 26, 415501 (2014).
- [50] N. Mironova-Ulmane¹, A. Kuzmin¹, J. Grabis, I. Sildos, V.I. Voronin, I.F. Berger and V.A. Kazantsev, *Solid State Phenomena Vols. 168-169* pp 341-144 (2011).
- [51] Fiebig, *Spin Dynamics of Antiferromagnetic Compounds*, (Universitat Bonn, Germany) (2010).
- [52] J.G. Lee, *Computational Material Science: An Introduction*, CRC Press, Ch.4 pp 99-100 (2011).
- [53] E. Koch, *Mean-Field Theory: Hartree-Fock and BCS*, Forschungszentrum Jülich GmbH, Vol. 6, No. 2 (2016).
- [54] J.C. Slater, *Physical Review*, Volume 81, Number 3 (1951).
- [55] J.C Slater, *The Theory of Complex Spectra*, *Phys. Rev.* 34, 1293 (1929).
- [56] W. M. C. Foulkes, L. Mitas, R. J. Needs and G. Rajagopal, *Rev. Mod. Phys.* 73, 33- 83 (2001).
- [57] P. R. C. Kent, *Techniques and Applications of Quantum Monte Carlo*, (Robinson College, Cambridge), Ch.2 Subsec. 2.3.0.1 (1999).
- [58] T. A. Kaplan, and W. H. Kleiner, *The Physics. Review, Second Series*, Vol. 156, No. 1 (1967).
- [59] R. O. Jones, *Rev. Mod. Phys.*, Vol. 87, No. 3, July–September 2015.
- [60] W. Kohn, A. D. Becke, and R. G. Parr, *J. Phys. Chem.*, 100, 12974-12980 (1996).
- [61] P. Hohenberg, and W-Kohn, *Phys. Rev.* Vol. 136, No. 3B (1964).
- [62] W.M.C. Foulkes, *Tight-Binding Models and Coulomb Interactions for s, p, and d Electrons*, Forschungszentrum Jülich GmbH, Vol. 6, No. 3 (2016).
- [63] L. A. Constantin, E. Fabiano, and F. D. Sala, *J. Chem. Phys.* 145, 084110 (2016).
- [64] W. Kohn and L.J. Sham, *Phys. Rev.* Vol. 140, No. 4A, p. A1133 (1965).
- [65] G. Kresse and J. Furthmüller, *Phys. Rev. B*, vol. 54, no. 16, pp. 11169–11186 (1996).
- [67] D.S. Sholl, and J. A. Steckel, *Density Functional Theory: A Practical Introduction*, John Wiley & Sons, Inc., New Jersey, Ch.1, pp 13-14 (2009).
- [68] A. Cucchieri and T. Mendes, *Phys. Rev. Lett.* PRL 118, 192002 (2017).

- [69] L. A. Constantin, J. P. Perdew, and J. M. Pitarke, *Phys. Rev. B* 79, 075126 (2009).
- [70] M. A. Mosquera, C. H. Borca, M. A. Ratner, and G. C. Schatz, *J. Phys. Chem. A* 2016, 120, 1605–1612.
- [71] John P. Perdew, Kieron Burke, Matthias Ernzerhof, *Phys. Rev. Lett.* Vol.77, No. 18 (1996).
- [72] A. D. Becke, *J. Chem. Phys.* 107 (20), 22 November 1997.
- [73] M. Godfrey, *Solid State Physics*, (University of Manchester, UK), Ch.2, pp 21-22 (2017).
- [74] W. Wessner, *Mesh Refinement Techniques for TCAD Tools*, (Technischen Universität Wien, Austria) Ch. 6, Subsec.6.3 (2006).
- [75] H. Hernández-Cocoletzi, G. H. Cocoletzi, J.F. Rivas-Silva, A. Flores, N. Takeuchi, *Journal of Nano Research*, Vol. 5, pp. 25-30, 2009.
- [76] L.A. Palomino-Rojas, M. Lo´pez-Fuentes, G. H. Cocoletzi, G. Murrieta, R. de Coss, N. Takeuchi, *Solid State Sciences* 10, 1228-1235, p. 1235 (2008).
- [77] J. A. Camargo-Mart´inez and R. Baquero, *Revista Mexicana de F´ısica* 59, 453–459 (2013).
- [78] M. Chan, G. Ceder, *Phys. Rev. Lett.* 105, 196403 (2010).
- [79] K. O. Obodo, and N. Chetty, *J. Phys.: Cond. Matt.*, Vol. 25, No.14 (2013).
- [80] A. Consiglio, and Z. Tian, *Nature: Scientific Reports* 6, Article number: 36875 (2016).
- [81] A. J. Garza, and G. E. Scuseria, *J. Phys. Chem. Lett.*, 7 (20), pp 4165–4170 (2016).
- [82] J. Hafner, G. Kresse, *Properties of Complex Inorganic Systems*, Springer US, pp 69-82, 978-1-4615-5943-6 (1997).
- [83] M. Cococcioni, S. de Gironcoli, *Phys. Rev. B* 71, 035105 (2005).
- [84] J. Petersen, F. Twagirayezu, P. D. Borges, L. Scolfaro, and W. Geerts. *AIP Advances*, vol. 7, 055711 1-5 (2017); doi:<http://dx.doi.org/10.1063/1.4975493>..
- [85] “Privacy Policy”, *ATC Flagship Series Sputtering Systems* .AJA International.inc. <http://www.ajaint.com/atc-series-sputtering-systems.html> (Accessed, March 2, 2017).
- [86] G. H. Xu, M. Zhu, J. Liu, Z. Zhou, H. Liang, *Wear* 255, 246-252 (2003).

- [87] Y. Cui, *Electrical and Optical Properties of RRAM*, (Alkek Library, Texas State University, US), (2016).
- [88] B. L. Dutrow, and C. M. Clark, *Geochemical Instrumentation and Analysis: X-ray Power Diffraction*, (Carleton College, US), (Accessed, March 2, 2017).
- [89] S. Tan, *Bruker D8 Discover XRD User's Guide*, (NanoScale, Fabrication, and Characterization Facility, University of Pittsburgh, US), ch.1, pp 1-2 (2009).
- [90] Jim Connolly, *Rigaku SmartLab Operation Procedures*, (Dept. of Earth & Planetary Sciences, University of New Mexico, US), pp 1-8 (2013).
- [91] J. Humlíček, *Handbook of Ellipsometry*, (Williams Andrew Publishing) Springer, Ch. 1, pp 6-9 (2005).
- [92] C. M. Morris, R. Valdés Aguilar, A. V. Stier, N. P. Armitage, *Opt. Express* 20, 12303-12317 (2012).
- [93] D. Chan, *Optical Investigations of Bioorganic Systems by Spectrally Resolved Ellipsometry*, Cuvillier Verlag Göttingen, 9783736915053, Ch.1 pp 2-21 (2005).
- [94] “Privacy Policy”, *Ellipsometry Tutorial: Optical Constants*. J.A Woollam. Co., Inc. <https://www.jawoollam.com/resources/ellipsometry-tutorial/optical-constants> (Accessed, April 2, 2017).
- [95] “Privacy Policy”, *Physical Property Measurement System (PPMS)*, Quantum Design Inc., <http://www.qdusa.com/products/ppms.html> (Accessed, April 6, 2017)
- [96] M. Klicpera, P. Javorský, M. Diviš, *Journal of Physics: Conference Series* 592 012014 (2015).
- [97] “Privacy Policy” *Oxygen Contamination*, Quantum Design, MPMS Application Note 1014-210B (1997).
- [98] T. Dubroca, J. Hack, and R. Hummel. *Phys. Rev. B* 74, 026403 (2006).
- [99] Steven E. Rios, et al. *J. Magn. Magn. Mat.* 286 (2005), 455-462.
- [100] J. Petersen, F. Twagirayezu, P. D. Borges, L. Scolfaro, and W. Geerts, *Ab initio study of oxygen vacancy effects on electronics and optical properties of NiO*, *MRS Advances* 1, 37, pp. 2617-2622 (2016).
- [101] “Privacy Policy”, *VSM Sample Mounting Techniques*, Quantum Design Inc., Application Note 1096-306, Rev. B1, (2016).
- [102] M. A. Garcia, E. F. Pinel, J. de la Venta, A. Quesada, V. Bouzas, J. F. Fernández, J. J. Romero, M. S. Martín González, and J. L. Costa-Krämer, *J. Appl. Phys.* 105,

013925 (2009).

- [103] A. Ghosh, C. Nelson, L. Abdallah, S. Zollner, *J. Vac. Sci. Tech. A*, 33, 061203 (2015).
- [104] P. Mallick, and R. Biswal, *Nanoscience and Nanotechnology*, 6(4): 59-61(2016).
- [105] Md. Abdul Ahad Talukder, Yubo Cui, Maclyn Compton, Luisa Scolfaro, Stefan Zollner, FTIR Ellipsometry study on RF sputtered Permalloy-oxide Thin Films, *MRS Advances* 1, 49, pp. 3361-3366 (2016).